Elasticity of viral capsids and topological defects

Lucas Menou


Numéro National de Thèse : 2020LYSEN038

THESE de DOCTORAT DE L'UNIVERSITE DE LYON
opérée par
l'Ecole Normale Supérieure de Lyon

Ecole Doctorale N° 52
Physique et Astrophysique de Lyon (PHAST)

Spécialité de doctorat : Biophysique
Discipline : Physique

Soutenue publiquement le 30/09/2020, par :
Lucas MENOU

Élasticité de capsides virales et défauts topologiques

Elasticity of viral capsids and topological defects

Devant le jury composé de :

QUILLIET, Catherine - Maitre de conférences - Université Grenoble Alpes - Rapporteure

TRESSET, Guillaume - Directeur de recherche CNRS - Université Paris-Saclay - Rapporteur

BOUDAOUD, Arezki - Professeur des Universités - ENS de Lyon - Examinateur

REGUERA, David - Full Professor - Universitat de Barcelona - Examinateur

CASTELNOVO, Martin - Chargé de recherche CNRS - ENS de Lyon - Directeur de thèse

ELASTICITY OF VIRAL CAPSIDS AND TOPOLOGICAL DEFECTS

LUCAS MENOU
Under the supervision of M. MARTIN CASTELNOVO

REMERCIEMENTS

Exprimer sa reconnaissance est, je trouve, l'un des actes des plus difficiles qui soit. Je ne suis jamais satisfait des mots que je trouve ni des formulations que j'emploie quand bien même je prétends savoir ce que je dois. Une fois encore, je n'ai qu'un seul mot, trop usé, tellement élimé (c'est de Pablo Neruda) : merci. Alors, je bute, pour qui ? Non pas, qu'il n'y ait personne, certainement pas, trop de noms résonnent et la concision impose un choix. Donc, en fataliste, une liste, elle préservera l'anonymat et le (pas si)net Internet sera mis au pas : merci au laboratoire de physique de l'ENS de Lyon, c'est long, plus long que la personnification métonymique utilisée mais(, mes ?) trois exquises années passées en ton sein m'ont nourri de discussions administratipoliticocoscienthéoriques enluminées, cloisonné que j'étais dans l'enfeu de mon esprit plus bas situé ; merci aux professeur·e·s, votre inspiration souvent doublée de recommandations m'ont permis de voler (vers) et de ravir (mes proches en obtenant) ce titre de docteur (bo-hé-mien) ; merci aux membres du jury ayant jugé ces travaux, j'espère avoir pris en compte l'entièreté de vos leçons ; merci aux ami·e·s, co-bureaux espions ayant supporté les insultes stoïquement encaissés par un CANYON entêté, aux grimpeurs et aux grimpeuses motivé·e·s aux remarques subtilement acérées, aux bouffeurs et aux bouffeuses *déficié* à l'apport energétique défiant la thermodynamique, aux gamers et aux gameuses programmé·e·s pour gagner, aux buveurs et aux buveuses de bière et de café, aux pauseurs et aux pauseuses aux règles déposées, aux magistériens et aux magistériennes encliqué·e·s, bref, aux étoiles dont je suis le féal (c'est de Rimbaud), et pour lesquels, par cette bohème non-abstème, il fallait que je fasse le beau ; merci à la famille de soutenir le lunatique lumen, si les précédent·e·s ont un poème (?), je suis, je serai toujours en dette pour celles et ceux que j'aime ; enfin, surtout, merci au directeur de thèse à l'ipad surchauffant, sous les coups de stylet virevoltant, calculant un tenseur de stress toujours plus rapidement (ce qui fut étonnamment relaxant). Je vous souhaite à vous, oui vous, qui m'avez lu jusqu'au bout, (merci à vous) la chance - non même la moitié de la chance, chanceux·euses, cela est suffisant - que j'ai eu de l'avoir eu pour diriger mes simus.

ABSTRACT

Viruses are in many ways fascinating biological systems. They vary in their structure, their replication methods, and in their target hosts. They are the smallest self-replicating and self-assembling entities on Earth. Viruses are partly made of a protein shell called the capsid, the most important and interesting component as it encloses their genetic material. The main role of the capsid is to protect the viral genome. As a result and despite their smallness, they have evolved to sustain high external or internal constraints. However, the mechanisms underlying the appearance of viruses (through the capsids shape) and those that bring their high resistances are still poorly understood. Such problematics are of great interest as they could lead to the development of artificial nanocages. Viral derived nanocages are promising for various bioappplications, such as gene therapies or nanoapplications, such as drug delivery. The work I propose in my Ph.D. aims to contribute modestly to the understanding of viral assembly and stability using both analytical and numerical investigations.

Viruses are biological structures produced thanks to molecular self-assembly. Because the final crystal is too be curved, the induced elastic stress is relaxed thanks to the introduction of topological defects in the protein lattice. We propose in the Ph.D. thesis a quantitative mechanism for this phenomenon by using standard thin shell elasticity. In particular, we show that the type and the angular location of a defect is determined by the value of the azimuthal stress that characterizes compressive or tensile regions. The elastic model proposed permits us to compare quantitatively the relaxation of mechanical stress induced by various defect distributions.

Testing the mechanical stability of viral particles is possible thanks to nanoindentation experiments by atomic force microscopy. Using a coarse-grained molecular simulation of a viral structure, we build in the Ph.D. thesis a framework to help interpret mechanical information obtained by such nanoexperiments. More specifically, non-vanishing Gaussian curvature of viruses and the geometry of the tip have an influence on the viral quantitative stiffnesses that can be extracted. The coalescence of analytical and numerical results enables us to capture and rationalize the latter influence. We hope the latter work to be of

interest for following investigations regarding mechanical aspects of viruses.

RÉSUMÉ

Les différentes propriétés des virus en font des objets intéressants et fascinants. On peut en trouver de différentes structures, avec des méthodes de réplication différentes et ils sont spécifiques à leurs cibles. Ils constituent la plus petite entité auto-assemblée, elle-même encodée par un matériel génétique. Ce génome est protégé par une capside à l'intérieur virus lui-même. La capside est le constituant le plus important d'un virus. Son rôle est de protéger le génome viral des agressions extérieures. De fait, elle peut supporter de hautes contraintes mécaniques ou chimiques externes et/ou internes. Cependant, les mécanismes conduisant à leur construction, influençant leurs formes et leur conférant cette résistance sont toujours assez peu compris. Ces problématiques présentent un intérêt majeur car elles ouvrent la porte au développement de nanocages. Ces nanocages inspirées des virus pourraient être particulièrement utiles pour des applications biologiques, en thérapie génique par exemple, ou des applications technologiques, comme la délivrance de médicaments à des cibles spécifiques. Le travail présenté dans cette thèse se propose modestement de contribuer à la compréhension de l'auto-assemblage et de la stabilité virale en utilisant des modèles numériques et analytiques.

Les virus sont des échafaudages biologiques auto-assemblés. La structure finale étant nécessairement courbée, la contrainte élastique au cours de l'auto-assemblage due à la courbure est relachée par l'inclusion de défauts topologiques dans le réseau protéique. Dans cette thèse, par l'utilisation de la physique de l'élasticité en milieu continu, on propose une modélisation pour ce phénomène. En particulier, on montre que le type et la localisation angulaire du défaut à la frontière de l'assemblage sont deux paramètres fixés par la contrainte azimuthale, celle-ci pouvant être compressive ou extensive. Le modèle élastique proposé permet de comparer et d'évaluer l'effet relaxant de différentes distributions de défauts topologiques dans la structure.

Par ailleurs, l'évaluation et les tests de stabilité mécaniques des structures virales ont été rendus possible par les expériences de nanoindentation par microscopie à force atomique. En utilisant une simulation numérique de dynamique moléculaire d'une structure virale

gros-grains, on construit dans cette thèse un cadre de travail permettant d'aider à l'interprétation des informations mécaniques tirées de ces expériences. Plus spécifiquement, la courbure Gaussienne non-nulle du virus indenté et la géométrie de la pointe utilisée pour l'indentation ont des influences sur la rigidité mécanique effective pouvant être extraite expérimentalement. La coalescence de résultats numériques et théoriques nous permet de capturer et de rationaliser cette influence. On espère que ce travail pourra être d'intérêt pour des recherches futures portant sur les propriétés mécaniques des virus.

CONTENTS

ABSTRACT vii

RÉSUMÉ viii

I STATE OF THE ART

1 BIOLOGICAL PRELIMINARIES 3
- 1.1 Résumé . . . 3
- 1.2 History of viruses and their morphology . . . 3
- 1.3 Structure and symmetry of capsids . . . 6

2 ELASTICITY AND DEFECTS 9
- 2.1 Résumé . . . 9
- 2.2 Elasticity on curved membranes . . . 9
  - 2.2.1 Euler theorem and Euler characteristic . . . 9
  - 2.2.2 Crystalline order and defects . . . 11
  - 2.2.3 Mathematical formalism . . . 14
- 2.3 Numerical simulations of deflected membranes . . . 20
  - 2.3.1 In-plane energy . . . 20
  - 2.3.2 Out-of-plane energy . . . 21
- 2.4 Cautions . . . 21

3 SELF-ASSEMBLY PATHWAY 23
- 3.1 Résumé . . . 23
- 3.2 Disclinations and curvature . . . 23
- 3.3 Dislocations and relaxation . . . 28
- 3.4 Motivation . . . 32

4 AFM, VIRUS AND DEFECTS 35
- 4.1 Résumé . . . 35
- 4.2 Introduction . . . 35
- 4.3 Atomic Force Microscopy . . . 35
- 4.4 Experiments . . . 36
- 4.5 Continuum model, scaling . . . 43
  - 4.5.1 Scaling . . . 43
  - 4.5.2 Deviation from Föppl–Von-Karman equations . . . 44
  - 4.5.3 Solutions . . . 45
  - 4.5.4 Cautions . . . 46
- 4.6 Numerical view point . . . 47
- 4.7 Motivations . . . 51

II MECHANICAL STRESS RELAXATION IN SELF-ASSEMBLY

5 GROWTH ON A CURVED SUBSTRATE 55
5.1 Résumé . . . 55
5.2 Introduction . . . 55
5.3 Equations in a polar frame . . . 55
5.3.1 Back to basics . . . 55
5.3.2 Creased membranes and crushed caps . . . 57
5.4 Growth on a spherical substrate . . . 60
5.4.1 Introduction of disclinations . . . 60
5.4.2 Introduction of dislocations . . . 67
5.5 Various distributions . . . 70
5.5.1 Defects along one direction VS multiple directions 70
5.5.2 Effect of scar lengths . . . 73
6 NUMERICAL TEST 75
6.1 Résumé . . . 75
6.2 introduction . . . 75
6.3 Numerical proceedings and test . . . 75
6.4 Switching from disclinations to dislocations . . . 78
6.5 Conclusion . . . 79

III STIFFNESS HETEROGENEITY IN VIRUSES

7 (VIRTUAL) NANOINDENTATION 85
7.1 Résumé . . . 85
7.2 Introduction . . . 85
7.3 Virtual Atomic Force Microscopy . . . 86
7.3.1 Parametrization of the empty capsid . . . 86
7.3.2 Interactions with the substrate and with the tip . 87
7.3.3 Simulation and relaxation . . . 87
7.3.4 Data extraction . . . 88
7.4 Results . . . 89
7.4.1 Spherical tip VS Conical tip . . . 89
7.4.2 Geometrical dependance . . . 89
7.4.3 5-fold, 3-fold symmetries . . . 92
8 GEOMETRICAL MODEL 95
8.1 Résumé . . . 95
8.2 Introduction . . . 95
8.3 Spherical nanoindentation . . . 95
8.4 Conical indentation . . . 97
8.5 Discussion . . . 98
8.6 Conclusion . . . 104

CONCLUSION 107

BIBLIOGRAPHY 113
Books 113
Articles 113
Collections 122
Technical report 123
Online 123

Figure 1.1 Schematic diagram of Zika Virus cycle, virus is recognized by the Fcγ receptors. This enables the virus to fuse with the ensosome and initiate virus production using the replication apparatus of the host cell. The release of copies kills the host cell. (Diagram taken from Ref. [43]) 5

Figure 1.2 The hidden geometry of the omegavirus. To highlight what has been said in the main text, an artistic coarse-graining is made [40]. This is an artistic coarse-graining It enables us to extract the magic number $T = 4$, where $h = 2, k = 0$. Omegavirus exhibits a *skew* capsid. 7

Figure 1.3 The three virus spherical classes. All canonical capsids may be built from a single type of pentamer and of distinct hexameral shapes, leading to *skew* (or *non-skew*) and *chiral* (or *non-chiral*) capsids. The path to get from one pentamer to its nearest neighboring one is highlighted in red. Proteins constituting viruses are coarse-grained into triangles for sake of clarity. The previous coarse-graining is explained hereafter (See Ch. 2). 8

Figure 2.1 Most viruses present an hexagonal packing. That is why we introduce previously the *triangulation number* T. A viral capsid can be coarse-grained as a shell exhibiting a triangular lattice. Each protein is represented as a triangle. Thus, T becomes a quantitative metric for capsid size. A) Structure of $P74-26$ major capsid protein (a typical monomer constituting the spherical $P74-26$ viral capsid) colored by domain with corresponding labeled schematic in Subfig. B. B) Domains of $P74-26$ major capsid protein. C) The hexagonal packing leading to a "triangulated" protein shell which presents then elastic properties. Figures are adapted from Ref. [97]. . 10

Figure 2.2 A typical coarse-grained icosahedral viral capsid, which can be seen as a curved elastic crystal, $T = 9$, $\{h, k\} = \{3, 0\}$. Each triangle represents a protein. This coarse-graining enables us to capture the in-plane and out-of-plane behavior of the elastic shell. Disclinations are highlighted with red dots. 12

Figure 2.3 A) An example of a flat disclination (5-fold coordinated) in a coarse-grained monolayer. In blue is highlighted the angle to add to recover an hexagonal lattice. B) An example of a flat dislocation in a coarse-grained monolayer, in red and black are highlighted two unclosed loops to show the Burgers vector highlighted in blue. Figures are adapted from Ref. [94]. Their definitions remain unchanged in curved membranes. 16

Figure 3.1 A) The unit cell in the form of a triangular prism. Each line represents a spring, the equilibrium lengths of springs, of constant stiffness k, constituting triangles are set from top to bottom $a_0 + 2\Delta$, a_0 and $a_0 - 2\Delta$, so that the radius of curvature of the outer shell is set $R = a_0(1 + a_0/2\Delta)$. Dashed and dotted lines represent springs connecting the three layers of triangles which stiffnesses are respectively $k/2$ and $k/3$ to make the sheet elastically isotropic. B) The closure algorithm. Because of the presence of spontaneous curvature, the opening angle α is always less than 60° contrary to a perfect hexagon. Thus, below a critical angle α_c, the five existing subunits are to be stretched to form a "pentagon", i. e. a disclination. Figures and details are taken from Ref. [62]. 24

Figure 3.2 Shapes and relative sizes of viral structures against the spontaneous radius of curvature, R, which is determined by the quantity Δ. Those structures were built using an algorithm described in the main text and in Fig. 3.1. Here a_0 is set to 1 and Δ is i) 0.2, ii) 0.15, iii) 0.1, iv) 0.08, v) 0.076, vi) 0.075, and vii) 0.072. A conical closed structure is obtained for $\Delta = 0.076$ that is $R_e \sim 7.5$. Figures and details are adapted from Ref. [62]. . 25

Figure 3.3 Elastic energy for a spherical membrane as function of the intermediate size during viral self-assembly. Elastic cost of disclinations is taken into account after their inclusion in the membrane. A) Energetic cascade for disclination inclusion. Elastic energy for 12 disclinations with icosahedral symmetry (thick red line), compared to the energy of $n = 1$ to $n = 12$ disclinations (thin black lines). Dashed vertical lines indicate the radial positions of disclinations. The elastic energy without disclinations is shown by the blue line. B) Elastic energy for 12 disclinations with icosahedral symmetry (thick red line), compared to 10 realizations of random locations for 12 disclinations (thin dashed colored lines). Inset: Example of locations of six disclinations regularly localized on the shell growing at a constant curvature. Figures and details are taken from Ref. [30] 26

Figure 3.4 The snapshots of a T = 13 growth in discrete simulation A) and continuum theory B). For the discrete part, the yellow vertices belong to pentamers, blue ones to hexamers, and red ones to the cap edge. The gold core mimics the preformed scaffolding layer or inner core. The caps for the continuum part denote the energy contour plots for the newest disclinations that appear in the purple energy well. The red region has the highest energy and the purple region the lowest one. There is a yellow ball in the position of each disclination. The largest ball corresponds to a newly formed disclination. Each valley corresponds to the position of a future disclination. Figures and details are adapted from Ref. [64]. 28

Figure 3.5 A disclination surrounded by a cloud of aligned dislocations (scars). The central disclination is highlighted in purple and dislocations in red and green. To distinguish them, $+1/6$ and $-1/6$ charges are in red and green respectively. The resulting configuration, particularly lengths L_1 and L_2 or intermediate spacings between dislocations constituting scars depend on details encrypted in elastic constants, imposed curvature and size of the crystal. The gold inner core mimics the imposed curvature. Figure is taken from Ref. [6]. 30

Figure 3.6 A) The schematics of six possible states (defect morphologies I–VI) described in the text. B) The phase space spanned by surface coverage, Φ, and boundary stresses, σ_b, that delineate the regions of mechanical stability (existence) for the competing radial scar morphologies described in the core text. Figures and details are taken from Ref. [6]. 31

Figure 3.7 A) Curved colloidal crystal under isotropic expansion, fracture appears along defects. The initial shell configuration (obtained by relaxing a random configuration of particles) shows topological defects already arranged in scars. R_0 represents the initial radius of the spherical crystal, ΔR its relative increase. B) Squeezing a colloidal crystalline sphere leads to plastic deformation mediated by grain boundary scars reorientation. The ellipsoid is deformed under the constant surface-area constraint. c represents the length of the semi-axis. 7-fold defects are represented in red on the snapshots, 5-fold in blue, 6-fold in grey. Figures and details are adapted from Ref. [72]. 33

Figure 4.1 A) Sketch of an Atomic Force Microscope (AFM). B) Sketch of the experimental approach for investigating the mechanical properties of capsids by means of nanoindentation. A sharp tip approaches the sample to be tested. The tip is attached to a cantilever. Deflections of the cantilever due to tip-sample interactions are measured thanks to the reflection of the laser onto a photodetector illuminating the back of the former. C)-D)-E) Typical experimental force-distance curves acquired on capsids. C)-D) Responses are linear. $F = k_{eff} z$, hence, it is possible to measure an effective spring stiffness k_{eff}. The linear response of the surface is due to the deflection of the cantilever. Hence, one shall take into account the stiffness of the cantilever to measure the stiffness of the sample itself. E) The drop in the force-distance curve is the physical signature of a sample mechanical failure. The sample is broken. Sketches and curves were kindly given by Mme Carrasco-Salas. 37

Figure 4.2 MVM particles as viewed along fivefold A), threefold B), and twofold C) symmetry axes. Left side corresponds to simplified cartoons. Center images represent molecular surfaces derived from cristallographic data taken from The Protein Data Bank (PDB ID code 1MVM; Ref. [1]). Right side: $60\,nm \times 60\,nm$ AFM images of MVM particles. Figures and details are taken from Ref. [24]. 38

Figure 4.3 Comparison of the mechanical properties of A) MVM empty capsids and B) virions. Left side gives the crystallographic structures of both particles using the program RasMol [92]. On the right side, the histograms are shown. The distributions of effective stiffness (spring constant, k) values is depicted for individual particles subjected to nano-indentation along fivefold (red), threefold (green), and twofold (blue) axes. Figures and details are taken from Ref. [24]. 40

Figure 4.4 A) Measured heights H_m of norovirus like particles as a function of pH. The dashed line shows the linear regression of H_c against the pH. B) Spring constant K as a function of pH, the error bars corresponds to the width of the median absolute deviation. The latter statistic was calculated from the slope in the linear region of the force-separation curve for at least 50 particles. Fig. adapted from Ref. [33]. 41

Figure 4.5 Nanoindentation experiments of Φ29. A) Typical forward indentations curves on different locations, i. e. on glass substrate (dotted), on the up right configuration (grey), on the laid down configuration (black). B) Classification of the indentation curve slopes, as previsouly, up right configuration is in grey and laid down one in black. Note the decrease of the spring stiffness in the second configuration. 56 indentations were carried out on 5 uprigth capsids and 6 laid down ones. We shall report that in the upright dataset, two proheads were adsorbed through the connector, two through the capped-end and one remains unidentified. Figures taken from Ref. [26]. 42

Figure 4.6 Contact force curves for the native numerical Cowpea Chlorotic Mottle Virus (CCMV) indented on each of the rotational symmetric orientations, as a function of the total displacement, which includes also AFM tip displacement. The stiffness of the cantilever of the AFM is set to $k \sim 0.05\,N\,nm^{-1}$. Figure is taken from Ref. [39] . 49

Figure 4.7 Force-distance relationships of locally deformed viral shells. ξ is the normalized indentation depth with the radius of the numerical shell R, F is scaled by κ_b/R where κ_b is the flexural rigidity here. A) For small γ, regimes are linear with an effective stiffness proportional to $\sqrt{\gamma}$. B)-C) Above the critical threshold γ_c, stiffness heterogeneity appears with the faceted shape. For $\gamma \sim 1000$, pentamers are stiffer than hexamers and for a strong indentation, pentamers buckle in the viral shell, causing softening. For $\gamma > 2000$, pentamers may even snap into a new stable inverted configuration, which creates discontinuities in the force-distance function. Figures and details are adapted from Ref. [20]. . . . 50

Figure 5.1 A) Plot of radial and azimuthal stresses (respectively σ_{rr} and $\sigma_{\theta\theta}$) against normalized radial position r/R, where r is the radial position in polar coordinates, R the radius of the cap. For this particular plot, $R/R_0 = 1/2$. R_0 denotes the radius of curvature. Note that above a critical radius $r^* = R/\sqrt{3}$, $\sigma_{\theta\theta}$ becomes negative. B) Sketch of the hoop stress profile where r^* is highlighted in blue. 59

Figure 5.2 Proposed mechanism for nucleations of defects illustrated on triangulated surfaces, based on values of hoop stress. Threshold values for hoop stress are labeled as σ_{5c} and σ_{7c}. Arrows represent the elastic stress that makes possible the nucleation of the respective (negative or positive) disclination in the azimuthal direction. If hoop stress is compressive enough, a positive disclination is nucleated. On the other hand, if hoop stress is tensile enough, a negative disclination is added. Last mechanism makes possible the introduction of dislocations in the crystalline structure, a supplementing positive 5-fold defect is to be attached to the 7-fold negative one. . . . 61

Figure 5.3 Relaxation of hoop stress by defect nucleation. The hoop stress at the rim of the assembly is computed with and without defects (highlighted in red on the sketched structure, we specify their angular positions on graphs). The size R of the structure is shown at the top of each graph in function of imposed Gaussian curvature radius R_0. The radial position of the first defect $\rho_1 = 0.95R_a$, the second defect $\rho_2 = 0.8R_b$, the third one $\rho_3 = 0.85R_c$. We chose radial positions in order to highlight relaxation of hoop stress described in the main text. At each step, a disclination is added at the most compressive region. 66

Figure 5.4 Hoop stress $\sigma_{\theta\theta}$ in function of the adimensionalized radial position r/R, R represents the size of the cap specified at the top of each graph in function of the imposed radius of curvature R_0. A) Only one positive disclination is included in the structure (a 5-fold defect). In the configuration specified in Fig. 5.3. We plot hoop stress for $\theta = 0$ i.e. the angular position of the first defect. Note the tensile burst near the border of the cap, this should favor the inclusion of a negative 7-fold defect. B) On the contrary, the negative disclination case is considered, though with same configuration. Now, a compressive burst near the border of the cap favors the nucleation of a 5-fold defect. Note the subsequent relief of hoop stress each time a disclination is added. 67

Figure 5.5 Hoop stress with respect to polar angle for various defect distributions. Those configurations are used to relax locally the mechanical stress due to the geometric curvature, we set Gaussian curvature to $1/R_0^2$. The size of the cap is shown at the top for each graph. A) All defects are arranged along the single angular position $\theta = 0$. Their radial positions are as follows, $\rho_5 = \rho_{57} = .95R_a$, for the charged dislocation $\rho_{57} = .95R_a$; $\rho_5 = .97R_a$. For the scar, $\rho_{57}^{(1)} = .95R_a$, $\rho_{57}^{(2)} = .97R_a$, $\rho_{57}^{(3)} = .99R_a$. For the charged scar, we chose a similar arrangement, and we set $\rho_5 = .996R_a$. For distributions close to the border, no particular effect is observed on stress relaxation patterns at long distance. B) However, for the very same arrangement, and if the size of the cap is increased, a strong modulation of the relaxing effect is possible, where the charged scar appears to be more efficient. C) We sketch here typical configurations at the rim of triangulated surfaces: a single dislocation and a scar made of two dislocations, hoop stress patterns are highlighted with red and blue arrows (respectively red for a compressive stress and blue for a tensile one). 71

Figure 5.6 Hoop stress relaxation against the angular position at the rim of the cap for several defect distributions. We highlight here that for similar defect arrangements, the "relaxation order" is conserved, i. e. no change in relaxation efficiency can be observed comparing respectively disclinations, dislocations, charged dislocations, etc., if same types of defect(s) are added at other angles. For instance, on graph A) defects are placed at $\theta = 0$, and then B) disposed at respectively $\theta_i = \{0, 2\pi/3, 4\pi/3\}$. Locations of defects are sketched by green stars on respective spherical caps below each graph. In fact, each defect nearly touches the boundary. The order remains unchanged. Nevertheless, a better mechanical relaxation can be noted due to the higher number of defects in the second case. 72

Figure 5.7 Hoop stress relaxation against the angular position at the rim of the cap for various length of scars. Defects are radially aligned along a single direction. We set $\rho_1 = .758R$, for the single disclination and single dislocation. Then, between each defect, we let a space of .008. Note that the best relaxation is obviously obtained for the longest scar. Hoop stress relaxation pattern remains unchanged though. 73

Figure 6.1 Comparison of analytical (lines) and numerical (points) energy densities at the rim of the coarse-grained crystalline cap for several defect distributions. Numerical structures were built accordingly. We present here the single disclination case and the single dislocation one A) at the rim and B) far from the border. C) The multidisclination case is shown below. The size of the spherical cap for each plot is shown above in function of the radius of curvature R_0. Other parameters, $\rho_5 = \rho_{57} = .88R_a$, and $\rho_5^{(3)} = .88R_c$. $\theta = 0$ for two first cases, $\theta_i = \{0, \pi/2, \pi\}$ for the last one. Locations of defects are sketched with green stars on respective spherical caps at top right corners. Satisfactory agreements are obtained for all cases without any adjustment. . 77

Figure 6.2 Snapshots of self-assembly simulations showing nucleation of defects depending on hoop stress thresholds. l_0 is the equilibrium length of edges.The first closing threshold is associated to the length $l_{5c} = 0.7l_0$. Then we increase the closing threshold l_{7c}. If $l_{7c} = 1.5l_0$ no dislocation appears in the simulation, only disclinations. We precise that the radius of curvature $R_0 = 12l_0$ and we set the ratio of moduli $k_e/k_b = 100$. Red dots highlights pentamers, blue dots, heptamers and green dots, tetramers. Tetramers are considered as defects on the boundary, we expect trimers instead. Each arrow indicates that 180 triangles (coarse-grained proteins) are added under the specified conditions above and below. 80

Figure 7.1 Comparison of virtual nanoindentation experiments using a spherical or a conical tip. A) Snapshot of a virtual nanoindentation using a spherical tip. B) Snapshot of a virtual nanoindentation using a conical tip. Note that the conical part is indenting the numerical capsid. This is highlighted by the blue dotted ellipse. C) Quadratic fits of the discrete elastic energy against the indentation depth. Note the decrease of the effective stiffness when the spherical tip is off-centered. D) Extracted numerical stiffness against the position of the tip for the spherical tip (red circles) and the conical tip (blue diamonds). Each point of the curve is the average of 4 virtual indentations. The error bars are the corresponding root mean-square deviations. The stiffness does not vanish for $r > R_0 + R_t$ with the conical tip. Parameters of simulations: $R_t/R_0 = 1/5$, Semi-aperture of the cone $\alpha = \pi/4$, $\gamma = 57.6533$. Other parameters unchanged. 90

Figure 7.2 Comparison of virtual nanoindentation experiments using various conical tips. A) Effective stiffness against the tip position, the aperture angle $\alpha = \pi/4$ is the same for both tips. Only the bottom radius was changed, for the blue diamond curve $R_t/R_0 = 1/5$, for the square green curve $R_t/R_0 = 3/4$. Note the shift to the right of the plateau for the bigger radius compared to the initial situation as function of the position of the tip. B) Here, both radii of conical tips are equal, only the aperture angle was changed, $\alpha = \pi/4$ for the blue diamond curve, and $\alpha = \pi/6$ for the magenta down triangle curve. Note the decrease of the heigth of the plateau with aperture angle of the cone. $\gamma \simeq 57.6533$. The experiment for each position was repeated 2 times, error bars correspond to square root type deviations. Other parameters unchanged. 91

Figure 7.3 Comparison of virtual nanoindentation experiments for various orientations and two different Föppl–Von-Karman numbers γ. A) Numerical effective stiffness against the position of the tip for various orientations of the numerical capsid, $\gamma = 57.6533$. Inset represents the structure of the capsid for such a γ. The orientations are taken in order to indent either on a disclination at the top or off-centered. Trajectories of the tip on the capsid are represented with the respective colors on sketches at the right. No significant differences can be noticed for this case. B) Numerical effective stiffness against the position of the tip for various orientations of the numerical capsid, $\gamma = 576.533$. Trajectories are represented with the same colors on the numerical capsid which structure is computed for latter γ. Strong discrepancies can be noticed. Parameters of the indentation and of the tip : $R_t/R_0 = 1/5, \alpha = \pi/4$. The experiment for each position was repeated 2 times, error bars correspond to square root type deviations. Other parameters unchanged. 94

Figure 8.1 Sketches of indentations. A) Indentation with a sphere, we highlight the fact that when the tip is off-centered, $X_{tip} = r$, the real indentation δ_r is less than the vertical descent or indentation δ. B) Indentation with a cone, the real indentation δ_r is constant after a given radial position of the tip $r = (R_0 + R_t)\cos\alpha$. Idealized deformed regions are highlighted in orange. 96

Figure 8.2 Effective stiffness against the position of the tip. The red curve represents the numerical stiffness obtained by indentation with a spherical tip, the blue curve represents the numerical stiffness obtained by indentation with a conical tip. Plain and dotted lines correspond to the respective analytical model. The trends appear to be correct for both cases but no quantitative agreement is observed. This can be due to the strong "no lateral movement" assumption. Parameters of the simulations: $\gamma = 57.6533, R_t/R_0 = 1/5, \alpha = \pi/4$ (for the cone). Each dot is the mean of 4 numerical experiments, error bars correspond to square root type deviations. Other parameters unchanged. 99

Figure 8.3 The need to take into account the horizontal response of the capsid. When the tip is off-centered, the capsid response possesses an horizontal component F_h. The latter component is highlighted for both spherical A) and conical B) cases. C) The quantitative disagreement between the geometrical model and the numerical results for quantitative stiffness as function of the lateral position of the tip may be due to this horizontal response. Parameters of the simulations: $\gamma = 57.6533, R_t/R_0 = 1/5, \alpha = \pi/4$ (for the cone). Each dot is the mean of 4 numerical experiments, error bars correspond to square root type deviations. Other parameters unchanged. 101

Figure 8.4 Horizontal displacement of the barycenter of all vertices against lateral position of the tip. A linear trend appears for both shapes of tip (spherical or conical) in agreement with Eq. (8.9) presented in main text. Parameters of the simulations: $\gamma = 57.6533, R_t/R_0 = 1/5, \alpha = \pi/4$ (for the cone). Dots represents the mean of 4 simulations and error bars correspond to respective square root deviations. 102

Figure 8.5 Effective stiffness against lateral position of the tip for various conical shapes. Colored curves represent numerical results. Plain and dotted lines correspond to respective corrected analytical models. Trends appear to be correct and a quantitative agreement is reached for all cases. The lateral movement is included in the model. Parameters of the simulations: $\gamma = 57.6533$. Respective parameters are specified above each figure. Other parameters unchanged. 103

ACRONYMS

HIV Human Immunodeficiency Virus
AAV Adeno-Associated Virus
HBV Hepatitis B Virus
MVM Minute Virus of Mice
AFM Atomic Force Microscope
CCMV Cowpea Chlorotic Mottle Virus
IBDV Infectious Bursal Disease Virus
BMV Brome Mosaic Virus
HOPG Highly Oriented Pyrolytic Graphite
TBSV Tomato Bushy Stunt Virus
VAFM Virtual Atomic Force Microscope

Part I

STATE OF THE ART

Gare à ceux qui prétendraient créer de toutes pièces un art nouveau sans aucun lien avec les formes de l'art historique. Car le passé est la base sur laquelle il faut fonder tout progrès, car ce passé, c'est l'expérience humaine tout entière, c'est l'enseignement des siècles.
– *César Daly*

1 BIOLOGICAL PRELIMINARIES

1.1 RÉSUMÉ

Dans ce chapitre, on se propose d'établir un bref état de l'art sur la morphologie et la structure biologique des virus. Un modèle d'infection viral général est rappelé, ainsi que la théorie de Caspar-Klug relative à la structure des virus sphériques.

1.2 HISTORY OF VIRUSES AND THEIR MORPHOLOGY

It is impossible to know with certainty how and when viruses emerged as they do not leave historical footprints such as fossils. Though, they must be prior to multicellular organisms, hence they should exist since the mesoproterozoic era [22]. They were discovered thanks to a porcelain filter, called the Chamberland-Pasteur filter, which could purify a liquid sample from its bacteria population. In 1892, Dmitri Ivanovsky showed that a disease of tobacco plant could be transmitted via liquid plant extracts even after their purification by Chamberland-Pasteur filtration. However, many years passed before a link was established between those filterable agents (seen previously as very small bacteria) and a new type of disease causing particle : Viruses. They are in many ways fascinating biological systems. They are the smallest self-replicating entities which use nucleic acids [1] to store their biological information or genome. They are able to self-assemble, thereby reducing significantly their free energy. Their genome is stored and protected by an outer shell called the "capsid" made of proteins [2] sometimes inside a second envelope made of proteins and phospholipids. These capsids are remarkably stable from the biochemical view point but they exhibit also remarkable mechanical properties (some

1. Nucleic acids are biopolymers, or small biomolecules, essential to all known forms of life, they encode and then store information of every life-form organism and viruses on Earth.

2. Proteins are large biomolecules, or macromolecules, consisting of one or more long chains of amino acid residues, i. e.organic compounds containing amine (-NH2) and carboxyl (-COOH) functional groups. Proteins are required for the structure, function, and regulation of the body's cells, tissues, and organs.

capsids can have a young modulus above 140 MPa) [70]. Viruses have additionnaly a very complex life cycle. Though their genomes encode all proteins needed to assemble new capsids, viruses lack any metabolic components or ribosomes possessed by cells. Consequently, they can only replicate within a host cell. At the surface of most virions [3], one finds glycoproteins [4] that enable viruses to bind to targeted cells via viral receptors. It is admitted that viruses have simply evolved to make use of those molecules, which have their own physiological functions in the cell, for their own replication. Usually, a virus attaches to the specific receptor site on the host cell membrane. Then, we can distinguish bacteriophages from plant and animal viruses. The nucleic acid of bacteriophages is injected in the host cell naked, leaving the capsid outside the cell. Plant and animal viruses can enter through endocytosis, in which the cell membrane surrounds the entire virus before its entire disassembly. Once the genome released in the cell, the replication mechanism strongly depends on the viral genome. Nevertheless, all viruses reroute host cell's replication process for proteins to synthesize viral enzymes and assemble new virions. After the assembly of many (typically hundreds of) copies, the new viral particles are released, often resulting in cell death. Outside their host cells the infectious particles remain passive until a new host is encountered, starting the replication process again (See Fig. 1.1). Because they are to interfere with very specific metabolisms, they are highly specific to their hosts. Consequently, as said earlier, they can be classified with the type of hosts they infect. They can be divided into bacteriophages, animal viruses, plant viruses and finally archaea viruses. Archaea viruses and bacteriophages, or shortly phages, infect prokaryotic (without a nucleus) host organisms (i. e. more generally bacteries). On the contrary, the host cells of animal and plant viruses are eukaryotic (with a nucleus).

A viral capsid is a shell made of proteins protecting the viral genome.

The detailed knowledge of the mechanism of viral assembly is of significant interest for bionano-application [95]: Their self-assembly offers the possibility to enclose tailored cargo, which could not enter the host cell otherwise, for gene therapies. It is now possible to load viruses experimentally with drugs, markers, and even nano-particles like quantum dots or magnetic beads [35, 48].

3. A virion is a complete virus consisting of a genome surrounded by a protein shell, it is the infective form of a virus.

4. Proteins which contain chains of monosaccharides (i. e. simple sugars).

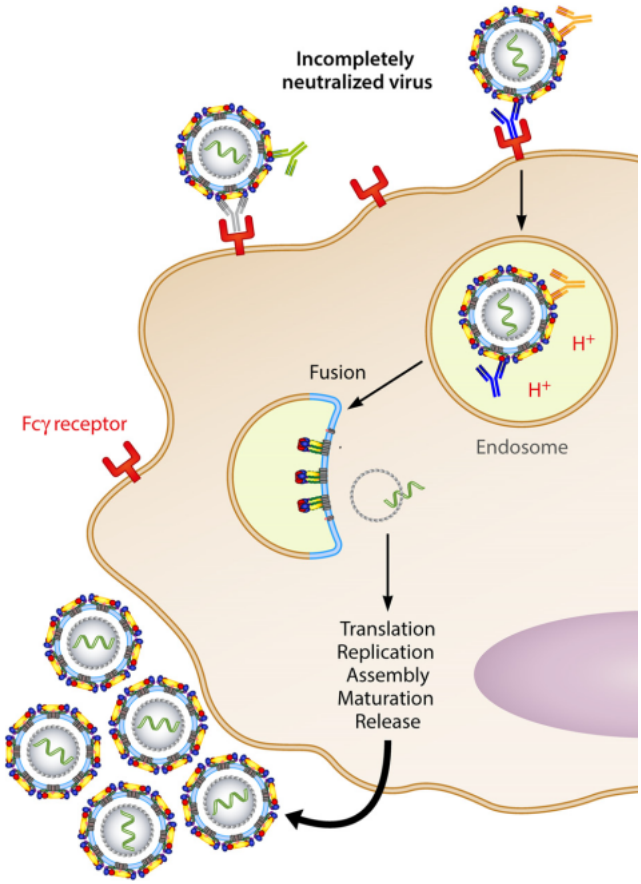

Figure 1.1 – Schematic diagram of Zika Virus cycle, virus is recognized by the Fcγ receptors. This enables the virus to fuse with the ensosome and initiate virus production using the replication apparatus of the host cell. The release of copies kills the host cell. (Diagram taken from Ref. [43])

This widespread use of the self-assembly paradigm is associated with its versatility and efficiency. It has motivated a recent series of experiments and the building of models exploring both the mechanical limits of viral capsids and the global self-assembly pathway. These studies revealed an astonishing robustness of viral shells against large internal pressure and externally applied forces underlining the progressive arising of their symmetry. This work aims to contribute modestly to the understanding of viral assembly and stability using both analytical and numerical investigations. In the following sections we present earlier theoretical results, that are important to know and to understand for studying capsid mechanic.

1.3 STRUCTURE AND SYMMETRY OF CAPSIDS

Capsid proteins are expressed from the RNA or DNA contained by the virus itself. As mentioned previously, once in the host cell, they self-assemble in a very efficient way that can withstand high internal or external pressure. Most of them are spherical but it is also possible to find more original structures in Nature, such as conical, e. g. the Human Immunodeficiency Virus (HIV) capsid, or toroidal one, e. g. the intracisternal toroidal type "A" virus of murine leukemia [13, 79]. Thanks to the modern techniques of X-ray spectroscopy and cryotransmission electron microscopy, the crystallographic structure of viruses is now part of the core knowledge of modern virology [96]. For most of them, the capsid proteins are grouped in subunits called *capsomers* i. e. oligomers made of either five (pentamer) or six (hexamer) proteins . Surprisingly but very interestingly spherical viruses possess an icosahedral symmetry (their shape is similar to a dice with 20 faces). As most viruses are spherical hollow containers, the simplest and smallest capsid one can imagine is a perfect icosahedron made of exactly 60 proteins assembled into pentamers. In that case, all proteins are similar and surrounded by a similar environment, leading to a very robust biological shell: The Adeno-Associated Virus (AAV) capsid. However, a capsomer has a limited size ($\sim 5\,\mathrm{nm}$), and 12 of them gives a very small virus which diameter $d \sim 25\,\mathrm{nm}$ [17, 47]. All viral genomes cannot be contained in such a small volume. Hence, Caspar and Klug proposed a brilliant model in which in larger shells, proteins shall arrange in such a way that the protein-protein interactions are *quasi-equivalent* to the ones found in the perfect icosahedral shell [28]. They proposed that for a given viral spherical shell, each triangular facet of the match-

A virus can be seen as a curved crystal.

ing icosahedron can be divided into three symmetrically equivalent parts. Those parts are called icosahedral asymmetric units (IAU), to construct the hexagonal lattice. Then, the Caspar-Klug Theory (CK Theory) is built upon 60 identical subunits organized on the 20 triangles creating the faces of the icosahedron. Consequently, the icosahedral symmetry of capsids is generalized to an *icosadeltahedral* one, where the number of hexamers is unlimited but exactly 12 pentamers lie on the vertex positions of a perfect icosahedron [5]. The number of hexamers required for the tessellation of a capsid with a given protein lattice structure is linked to the so-called *triangulation number* T [6] introduced with the *quasi-equivalence principle*. T follows a sequence of *magic numbers* ($T = 1, 2, 3, 4, 7, 9, \cdots$) characterized by two integers h, k which describe the number of hexamers one would have to "walk over" to get from one pentamer to an adjacent pentamer within a completed capsid $T = h^2 + hk + k^2$. In order to get from one pentamer to its nearest neighboring pentamer, one must follow a straight chain of h hexamers, then make a 60 degrees turn and proceed another straight chain of k hexamers (See Fig. 1.2).

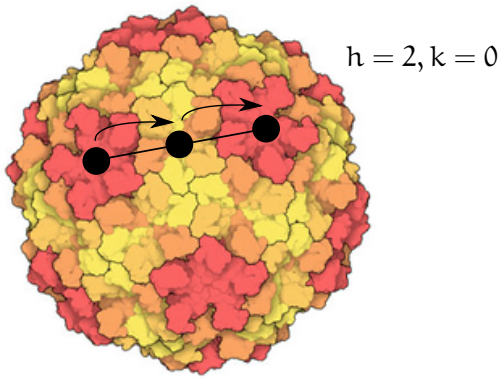

Figure 1.2 – The hidden geometry of the omegavirus. To highlight what has been said in the main text, an artistic coarse-graining is made [40]. This is an artistic coarse-graining It enables us to extract the magic number $T = 4$, where $h = 2, k = 0$. Omegavirus exhibits a *skew* capsid.

This number comes handy as, in most cases, a capsid with a triangulation number T is comprised of $60T$ capsid proteins, or 12 pentamers

5. The number of pentamers is topologically constrained to close a capsid whatever its shape as we will see in further details later.

6. The adjective "triangulation" is explained herefater in Ch. 2.

and $10(T-1)$ hexamers [28, 68]. When $h \geqslant k > 0$, we use the term *skew* capsid. Skew capsids with $h \neq k$ are chiral (See Fig. 1.3).

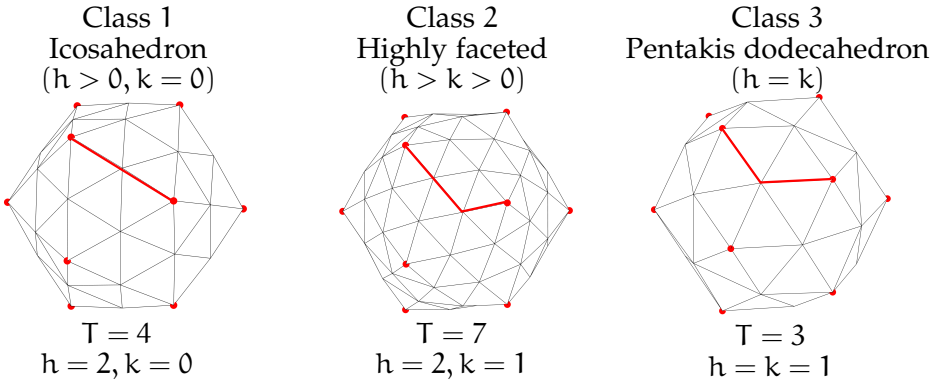

Figure 1.3 – The three virus spherical classes. All canonical capsids may be built from a single type of pentamer and of distinct hexameral shapes, leading to *skew* (or *non-skew*) and *chiral* (or *non-chiral*) capsids. The path to get from one pentamer to its nearest neighboring one is highlighted in red. Proteins constituting viruses are coarse-grained into triangles for sake of clarity. The previous coarse-graining is explained hereafter (See Ch. 2).

Small capsids are generally spherical, but large viruses (e. g. phage HK97 or the phycodnavirus with a diameter approaching 100 nm) exhibit a faceted geometry with nearly flat portions between the twelve pentamers pointing outward. This *buckling transition* results from the competition between the stretching energy associated with the pentamers (*in plane* energy) in the lattice of capsomers and the bending elasticity of the viral capsid (*out of plane* energy) [66]. All what has been said previously is valid for viruses exhibiting a spherical aspect, non-icosahedral capsids with spherocylindrical shapes are common among bacteriophages. Even more complex, polymorphism can be observed for several capsids. This polymorphism depends on the physiological environment itself. Exceptions to the quasi-equivalence principle suggest that shapes of capsids depend strongly on capsomer-capsomer interactions which themselves depend on spatial environment. It reflects an influence of the covalent bindings but also of the conformational changes in the protein structures. The exact shape of these of course differs from a protein type to another.

Hence, rationalizing the morphological aspect of viral capsids appears to be a great challenge from the chemical, physical, biological and mathematical view point [9, 91].

2 ELASTICITY AND DEFECTS

2.1 RÉSUMÉ

On se propose de détailler ici les modèles mathématiques et numériques nous permettant de rationaliser les comportements élastiques des virus ainsi que leur structures. Une emphase est mise sur la description mathématique des pentamères et des heptamères considérés comme des défauts topologiques dans la structure protéique biologique des virus.

2.2 ELASTICITY ON CURVED MEMBRANES

2.2.1 *Euler theorem and Euler characteristic*

Proteins constituting viral capsids can be seen as triangles and are packed hexagonally, the most condensed state in the curved biological shell.

Proteins possess somehow the ability to deform reversibly. Hence, a shell made of proteins shall present elastic properties and shall be deformable. Then, a virus can be seen as a crystal but more importantly as *a curved elastic crystal*. Provided reasonable hypotheses, it shall be possible to use physics of elasticity to describe the elastic behavior of viruses. One can look first at the local protein packing to make viral capsids, as we only describe the global symmetry of spherical capsids in Ch. 1. It appears that, in most viruses, proteins are packed hexagonally (as described previously), because it is the most condensed state reachable for them (See Fig. 2.1).

There exists a geometrical frustration in the hexagonal protein lattice due to the curvature required for the closure of the viral shell itself...

However, the latter hexagonal packing is in conflict with the geometrical curvature required to close the shell. An hexagonal protein lattice shall lead to a planar membrane. From now on, one can introduce the notion of *geometrical frustration* to describe situations where certain types of local order (here the hexagonal packing), favoured by physical interactions, cannot propagate throughout a system [90]. The geometrical frustration in our case is revealed by the Euler theorem. This elegant theorem relates the number of vertices (written V), the

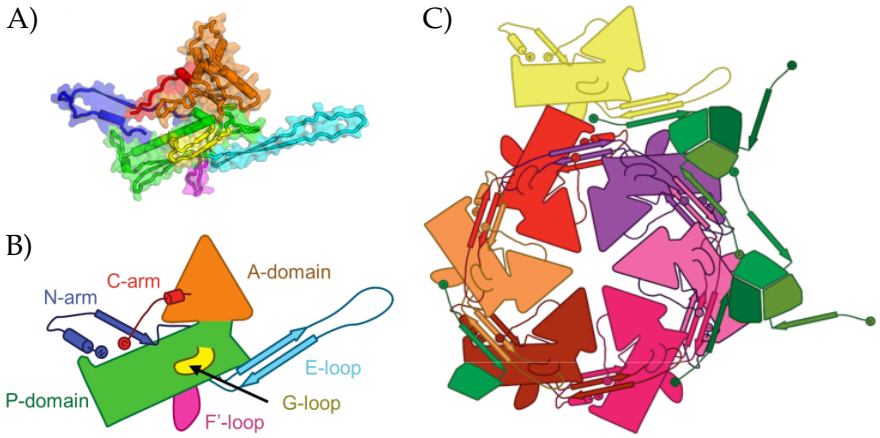

Figure 2.1 – Most viruses present an hexagonal packing. That is why we introduce previously the *triangulation number* T. A viral capsid can be coarse-grained as a shell exhibiting a triangular lattice. Each protein is represented as a triangle. Thus, T becomes a quantitative metric for capsid size. A) Structure of P74 – 26 major capsid protein (a typical monomer constituting the spherical P74 – 26 viral capsid) colored by domain with corresponding labeled schematic in Subfig. B. B) Domains of P74 – 26 major capsid protein. C) The hexagonal packing leading to a "triangulated" protein shell which presents then elastic properties. Figures are adapted from Ref. [97].

number of edges (written E) and the number of faces (written F) for any convex polyhedron (such as our coarse-grained capsid) [1]:

$$V - E + F = \chi_E. \tag{2.1}$$

In Eq. (2.1), χ_E is the *topological charge*. There exists an easy path to compute the previous number. χ_E is related to the *genus* g of the tessellated closed surface. Indeed, g represents, in simple words, the number of "handles" of it and one can write $\chi_E = 2(1-g)$. For surfaces with boundaries, the Euler number is given by $\chi_E = 2(1-g) - h$, where h is the number of boundaries or "holes". Consequently, a sphere without holes nor handles ($g = 0, h = 0$) has its Euler characteristic equal to 2, a torus with 1 handle and no boundaries ($g = 1, h = 0$) has its Euler characteristic equal to 0. Two orientable closed surfaces with the same genus (thus the same Euler characteristic) are homeomorphic. They can be mapped into one another without changing their topological properties. One kind of mapping includes any transformation of a surface in space that can be achieved by bending, stretching, squeezing or shrinking the surface. So, essentially, we can achieve a homeomorphism by treating a surface in space as if it were made from a sheet of rubber and then bending, stretching, squeezing or shrinking it. If one can continuously deform a surface into another without drilling or tearing it, former and latter surfaces are homeomorphic and topologically equivalent.

Then, if one wants to tesselate a sphere using an hexagonal lattice (or to build a viral shell), one shall make sure that the equation $V - E + F = 2$ is satisfied by the tessellation. This mandatory directive is possible to follow by the introduction of topological defects in the crystalline order of the membrane.

2.2.2 *Crystalline order and defects*

As we are to study crystals with 6-fold local order (See Subsec. 2.2.1), it should be useful to introduce a minimal model. Instead of studying the elasticity of an all-atom system, we shall represent a single protein as a triangle. Then, to mimic the previous presented tessellation, we create a bond between each pair of adjacent proteins. Consequently, within this discrete model, building blocks are triangles.

1. In our coarse-grained model, F represents the number of proteins, V the number of summits of proteins, E the number of edges between adjacent proteins.

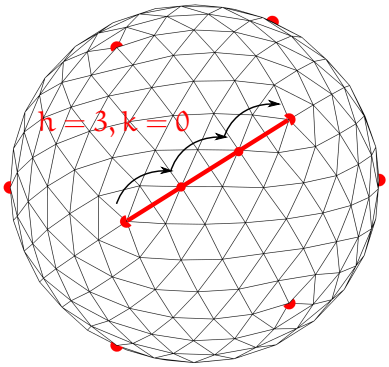

Figure 2.2 – A typical coarse-grained icosahedral viral capsid, which can be seen as a curved elastic crystal, $T = 9$, $\{h, k\} = \{3, 0\}$. Each triangle represents a protein. This coarse-graining enables us to capture the in-plane and out-of-plane behavior of the elastic shell. Disclinations are highlighted with red dots.

The previous coarse-graining has been extensively used to explore capsid growth [46, 62, 74]. Here, we shall discuss about a technical detail. Indeed, a shortcut was taken. It is not correct to say that a protein is exactly coarse-grained by a triangle. The latter sentence is valid only if the capsid one wishes to represent is sufficiently big (with a triangulation number $T \geqslant 7$). For smaller capsid ($T = 1, 3, 4$), the latter coarse-graining possess a loop effect, and a triangle represents in fact 3 packed proteins [2] [103].

Coming back to our model, It shall be necessary to name a topological defect as also a *topological charge*, where the so-called charge is the deviation from the ideal coordination number of the planar triangular lattice. If one writes q_i and c_i the charge and the coordination number of the i^{th} vertex respectively, one has $q_i = 6 - c_i$. This notion of charge comes handy by use of the famous Gauss-Bonnet theorem, which relates the Euler characteristic introduced earlier and the total charge of the crystal Q:

$$Q = \sum_{i=1}^{V} q_i = 6\chi_E. \tag{2.2}$$

For the case of viral capsids, or simply, spheres, the total charge must be equal to 12, using Eq. (2.2). Hence, if one wishes to tessellate a sphere using a triangular lattice, one shall introduce twelve pentagones, i. e.

2. Those 3 proteins, once packed, exhibit indeed a triangular shape.

twelve vertex coordinated five times [3]. Let us explain why. It is possible to relate the coordination number c_i of a vertex to its contribution to the Euler sum written e_i. Let us consider consider a tessellation in which each face is a triangle : each edge then belongs for one-half to the vertex and each face for $1/3$. Thus, the contribution of the i^{th} vertex to the euler sum is given by:

$$e_i = 1 - \frac{c_i}{2} + \frac{c_i}{3} = 1 - \frac{c_i}{6}. \tag{2.3}$$

Hence, a vertex coordinated five times has a $+1/6$ contribution, a vertex coordinated seven times has a $-1/6$ contribution and a vertex coordinated six times (the ideal coordination number of a planar triangular lattice) has zero contribution. In other words, a vertex ideally coordinated is shared among 6 faces, other coordination numbers lead to the introduction of a defect in the lattice. Immediately, it is easy to realize that the contribution of twelve pentagons to the Euler sum is exactly 2. Referring to Ch. 1, we now know why capsids present hexamers (6 hexagonally packed proteins) with exactly 12 pentamers (5 pentagonally packed proteins). Their protein lattice is in fact geometrically frustrated by their own curvature required for their closure.

... and building the latter frustrated protein lattice is made possible by the introduction of exactly 12 pentamers called positive disclinations and possibly pentamer-heptamer pairs called dislocations. On the contrary, isolated heptamers, physically and mathematically forbidden in the lattice are called negative disclinations.

Note that, in crystalline shell exhibiting a triangular lattice, dipoles of topological defects can exist. Indeed, following our previous reasoning, a dipole constituted of a pentamer-heptamer pair presents a zero charge (and consequently a zero contribution to the euler sum) in the soft network. Nonetheless, the elastic stress shall be non-negligible close to the introduced topological dipole. Those two types of defects are the main ones we will focus on in this study. Hereafter, isolated pentagons and isolated heptagons in the triangulation are called *disclinations*. Due to their charges, they are respectively called *positive* and *negative* disclinations. They represent pentamers (respectively heptamers) for viral capsids, and they are the consequence of the geometrical frustration associated to the topology of the biological membrane. Pentagon-heptagon pairs exhibiting a zero contribution to the Euler sum and that are not topologically forbidden are called *dislocations*.

Consequently, we know now that a virus can be viewed as an elastic curved shell. The latter possesses a thickness and its geometry can be defined by specifying the form of its middle surface (the middle curved plane of the shell) and of its thickness at each point. To study the mechanic of viruses during self-assembly, we now make two hypotheses.

3. Note that fullfilling Eq. (2.2) enables at the same time to fullfill Eq. (2.1).

Firstly, we assume that the straight lines, initially normal to the middle plane of the membrane *before* the deformation, remain straight and normal to the middle surface *during* the deformation, and the length of such elements is not altered. Secondly, we assume the absence of reciprocal pressure of horizontal layers. In other words, for a given layer, no pressure is exerted from the layer above or below. Hence, and from now on, we will assume that viruses behave as shells of constant thicknesses. Hence, we see (possibly unclosed) viruses as *2D elastic crystals*. We will briefly describe in next subsection the mathematical formalism used to describe such shells.

2.2.3 *Mathematical formalism*

In this subsection, we introduce briefly the mathematical formalism of 2D continuum elasticity used in this work. Obviously, this summary is not exhaustive and we just describe the minimalist toolkit used to study elastic crystal assumed to describe correctly viral elastic behavior. This brief reminder is separated in two subsubsections, in-plane elasticity and out-of-plane elasticity considered with the Monge gauge explained hereafter. For sake of simplicity, this introduction will have two conventions, we use implicit Einstein summation (components with repeated index are summed up), and displacements/components are embeded in a 3D euclidean space described by cartesian coordinates. In order to use other arbitrary coordinates, one can use nothing but the chain rule to reparametrize as one wishes.

2.2.3.1 *In-plane formalism*

There exists a mathematical formulation to describe disclinations and dislocations within the crystalline order of the viral shell.

Let us suppose an initial flat elastic crystal. The analysis of the flat membrane begins with the elastic free energy taken to be quadratic in strain (using tensor notation):

$$E = \frac{1}{2}\int_S ds\,(2\mu u_{ij}u_{ij} + \lambda u_{ii}^2), \tag{2.4}$$

where λ and μ are the 2D Lamé coefficients characterizing the elastic properties of the membrane, S its total surface, u_{ij} the 2D strain. In elasticity, a deformation is represented by a vector field $\mathbf{u}(\mathbf{r}) = (u_1, u_2)$ which maps the point $\mathbf{r}(x_1, x_2)$ to $\mathbf{r}(x_1, x_2) + \mathbf{u}(x_1, x_2)$. Hence, the in-plane deformation is encoded in the in-plane vector field $\mathbf{u}$. The strain is defined as the change in separation between points in the reference

state, dl^2, and deformed state dl'^2, $dl'^2 - dl^2 = 2u_{ij}\,dx_i\,dx_j$. This gives:

$$u_{ij} = \frac{1}{2}\left(\frac{\partial u_i}{\partial x_j} + \frac{\partial u_j}{\partial x_i} + \frac{\partial u_k}{\partial x_i}\frac{\partial u_k}{\partial x_j}\right) \simeq \frac{1}{2}\left(\frac{\partial u_i}{\partial x_j} + \frac{\partial u_j}{\partial x_i}\right). \tag{2.5}$$

The last equality of Eq. (2.5) holds for small deformations [61]. Note that u_{ij} is symmetric (no change appears if i, j indexes are inverted in the latter equation). We note $\partial/\partial x_i = \partial_i$ the covariant derivative against the i^{th} component. In the absence of topological defects, the displacement is a single valued mapping. In their presence, the mapping is disrupted and $\mathbf{u}$ becomes a multi-valued function. Following the model built by Seung and Nelson [94], disclinations can be defined in terms of a bond angle field on the crystal. It measures the orientation of edges around each vertice. Hence, crossing any closed loop L containing a disclination increases the scalar θ of an increment called *disclinicity* s.

$$\oint_L d\theta = \oint_L \frac{\partial \theta}{\partial x_i}\,dx_i = s \tag{2.6}$$

In our coarse-grained lattices with a 6-fold rotationnal symmetry, s is a multiple of $2\pi/6$. The values $\pm 2\pi/6$ are the most important for our case because they represent respectively the ± 1 topological charges (i. e. pentagons and heptagons mathematically). The disclinicity is the angle (to withdraw or to add) by which it is possible to recover the original lattice (See Fig. 5.5). Using the Stokes theorem, it is possible to rewrite Eq. (2.6) on partial derivatives to get the mathematical formulation of a disclination located at $\mathbf{r}_0$ on the plane:

$$\epsilon_{ij}\frac{\partial}{\partial x_i}\frac{\partial}{\partial x_j}\theta = s\delta(\mathbf{r} - \mathbf{r}_0). \tag{2.7}$$

ϵ_{ij} is the Levi-Civita tensor and δ is the classic Dirac delta distribution. We give its definition:

$$\epsilon_{i,j} = \begin{pmatrix} 0 & \epsilon_{12} = 1 \\ \epsilon_{21} = -1 & 0 \end{pmatrix} \tag{2.8}$$

One can relate the bond-angle field and the displacement with the relation $\theta = 1/2\epsilon_{ij}\partial_i u_j$ [73]. Hence, it follows that:

$$\epsilon_{ik}\epsilon_{jl}\partial_k\partial_l\frac{1}{2}(\partial_i u_j - \partial_j u_i) = s\delta(\mathbf{r} - \mathbf{r}_0). \tag{2.9}$$

Regarding dislocations, they can be defined directly from the displacement vector. Indeed, crossing a counterclockwise loop L containing the dislocation core increments $\mathbf{u}$ by a vector $\mathbf{b}$ called the *Burgers vector*. Mathematically, this gives:

$$\oint_L du_k = \oint_L \frac{\partial u_k}{\partial x_i} dx_i = b_k. \tag{2.10}$$

The Burgers vector is the amount by which the path around the singularity fails to close (See Fig. 5.5). Following the same method used previously, it is possible to write ($\mathbf{r}_0$ being the location of the dislocation):

$$\epsilon_{li} \frac{\partial}{\partial x_l} \frac{\partial}{\partial x_i} u_k = b_k \delta(\mathbf{r} - \mathbf{r}_0). \tag{2.11}$$

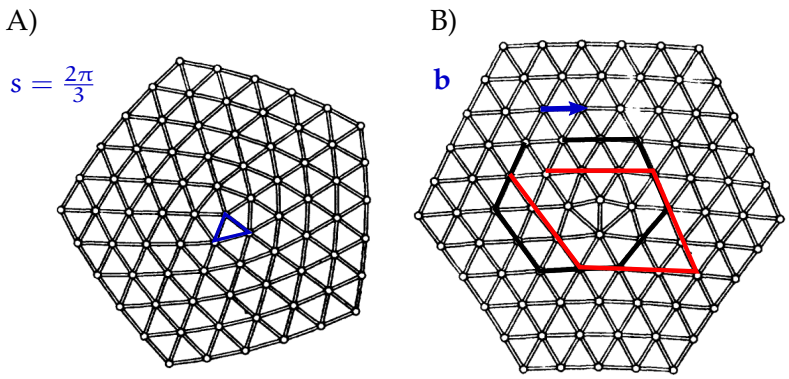

Figure 2.3 – A) An example of a flat disclination (5-fold coordinated) in a coarse-grained monolayer. In blue is highlighted the angle to add to recover an hexagonal lattice. B) An example of a flat dislocation in a coarse-grained monolayer, in red and black are highlighted two unclosed loops to show the Burgers vector highlighted in blue. Figures are adapted from Ref. [94]. Their definitions remain unchanged in curved membranes.

Minimizing the previous free energy E against variations of $\mathbf{u}$ enables us to get the equilibrium equation:

$$\frac{\partial \sigma_{ij}}{\partial x_i} = 0, \tag{2.12}$$

where σ_{ij} is defined as the stress tensor (with δ_{ij} the Kronecker symbol):

$$\sigma_{ij} = 2\mu u_{ij} + \lambda u_{kk} \delta_{ij}. \tag{2.13}$$

Eq. (2.13) and Eq. (2.12) permit us to say that the stress tensor is also symmetric and has zero divergence. Thus, it can be derived from a scalar function χ and defined as the *Airy stress function* [61]:

$$\sigma_{ij} = \epsilon_{ik}\epsilon_{jl}\frac{\partial}{\partial x_k}\frac{\partial \chi}{\partial x_l}. \tag{2.14}$$

Although, various χ functions can satisfy Eq. (2.12). We shall give a *compatibility equation* so that χ provides the way to derive a physically realizable stress distribution *given* a displacement $\mathbf{u}$. Inverting Eq. (2.13) yields:

$$u_{ij} = \frac{1+\sigma}{Y}\sigma_{ij} - \frac{\sigma}{Y}\sigma_{ll}\delta_{ij}, \tag{2.15}$$

where we define:

$$\begin{aligned} Y &= \frac{4\mu(\mu+\lambda)}{2\mu+\lambda}, \\ \sigma &= \frac{\lambda}{2\mu+\lambda}, \end{aligned} \tag{2.16}$$

as respectively the 2D *Young modulus* and the *Poisson ratio*. Combining Eq. (2.14) and Eq. (2.15) leads to an equation on the Airy stress function and the 2D strain:

$$\begin{aligned} \frac{1}{Y}\nabla^4\chi &= \epsilon_{ik}\epsilon_{jl}\partial_k\partial_l u_{ij} \\ &= \epsilon_{ik}\epsilon_{jl}\partial_k\partial_l\frac{1}{2}(\partial_i u_j - \partial_j u_i) + \epsilon_{ik}\epsilon_{jl}\partial_k\partial_l\partial_j u_i \\ &= \epsilon_{kl}\partial_k\partial_l\theta + \epsilon_{ik}\partial_k\epsilon_{jl}\partial_j\partial_l u_i, \end{aligned} \tag{2.17}$$

where $\nabla^4 = \nabla^2\nabla^2$ is the bilaplacian, the laplacian ∇^2 being equal to $\partial_i\partial_i$ on the plane. With the use of Eq. (2.6) and Eq. (2.7), we finally write the final *in-plane stress compatible equation*:

$$\frac{1}{Y}\nabla^4\chi = \sum_\alpha s_\alpha\delta(\mathbf{r}-\mathbf{r}_\alpha) + \sum_\beta b_i^\beta\epsilon_{ik}\partial_k\delta(\mathbf{r}-\mathbf{r}_\beta). \tag{2.18}$$

In Eq. (2.18), we summed over all topological defects that can be present in the surface. The α^{th} disclination is located at $\mathbf{r}_\alpha$ on the plane, and the β^{th} dislocation possessing a Burger vector $\mathbf{b}_\beta$ is located at $\mathbf{r}_\beta$. In the latter equation, the dipolar nature of dislocations can be clearly seen with the derivative. Disclinations can be seen as the fundamental defect, and one can build dislocations out of very close opposite pairs

of disclinations (pentagons with a $+1$ charge and heptagons with a -1 charge) with their mathematical expression taken at first order [89]. We note $s(\mathbf{r})$ the right term of Eq. (2.18), and we call it classically the *topological defect density*. It is the source of elastic stress in the planar membrane by analogy with the famous Poisson equation.

$$\frac{1}{Y}\nabla^4\chi = s(\mathbf{r}). \tag{2.19}$$

Nonetheless, Eq. (2.19) is incomplete, because it is restricted to *planar membranes*. But our aim is also to describe elastic behaviors of shells that buckle out of the plane to give incomplete or complete viral capsids.

2.2.3.2 *Out-of-plane formalism*

If one is to study elasticity of non-planar shell, a description of the deflection is required. Consequently, the in-plane displacement is described by previous application $\mathbf{u}(\mathbf{r}) = (u_1, u_2)$ but the out-of-plane one is described with the new-vector field $\mathbf{w}(\mathbf{r})$. In other words, a point in the reference state which was at the position $\mathbf{r}(x_1, x_2)$ is to move to its new position $\mathbf{r}(x_1, x_2) + \mathbf{u}(x_1, x_2) + \mathbf{w}(x_1, x_2)$ in the deformed state. Here, the in-plane deformation is encoded in the vector field $\mathbf{u}$ and the out-of-plane deformation is encoded in the vector field $\mathbf{w}$. In this precise case, $\mathbf{w}$ is in fact a vector field containing a single non-zero component w along the *vertical direction*. This is by far the most popular parametrization for deflected crystals. Called the Monge parametrization, it describes them with a single height function above or below a flat reference plane [34].

Then, the exact form of the strain tensor becomes:

$$\begin{aligned} 2u_{ij} &= \partial_i u_j + \partial_j u_i + \partial_i u_k \partial_j u_k + \partial_i w \partial_j w \\ &\simeq \partial_i u_j + \partial_j u_i + \partial_i w \partial_j w. \end{aligned} \tag{2.20}$$

We define the elastic free bending energy, also called the Helfrich energy H as:

$$H = \int_S ds \left(\frac{1}{2} D \mathscr{H}^2 + \kappa \mathscr{K} \right), \tag{2.21}$$

where $\mathscr{H}$ and $\mathscr{K}$ are respectively the mean curvature and the Gaussian curvature. D, κ, are respectively the flexural rigidity and the Gaus-

sian rigidity [44]. We compute $\mathscr{H}$ and $\mathscr{K}$ (within the Monge gauge formalism for deflections):

$$\mathscr{H} = \nabla \cdot \left(\frac{\nabla w}{\sqrt{1+|\nabla w|^2}} \right) \simeq \nabla^2 w\,; \tag{2.22}$$

$$\begin{aligned} \mathscr{K} &= \frac{\det \partial_i \partial_j w}{(1+|\nabla w|^2)^2} \simeq \det(\partial_i \partial_j w) \\ &= -\frac{1}{2} \epsilon_{ik} \epsilon_{jl} \partial_k \partial_l (\partial_i w \partial_j w). \end{aligned} \tag{2.23}$$

Last equalities hold if $|\nabla w|$ is small. Then, to derive the analog of Eq. (2.19), in the deflected case, we shall minimize the sum $H + E$ against $\mathbf{u}$ and $\mathbf{w}$. This gives:

$$\begin{aligned} D\nabla^4 w &= \nabla_i \sigma_{ij} \partial_j w, \\ \partial_i \sigma_{ij} &= 0. \end{aligned} \tag{2.24}$$

Again, with the very same definition and methodology used previously, cf. Eq. (2.14) and Eq. (2.18), we write:

$$\begin{aligned} D\nabla^4 w + \epsilon_{ik} \epsilon_{jl} \partial_k \partial_l (\partial_i \chi \partial_j w) &= 0, \\ \frac{1}{Y} \nabla^4 \chi = s(\mathbf{r}) + \frac{1}{2} \epsilon_{ik} \epsilon_{jl} \partial_k \partial_l (\partial_i w \partial_j w). \end{aligned} \tag{2.25}$$

Let L be the non-linear scalar operator:

$$L(h, f) = -\epsilon_{ik} \epsilon_{jl} \partial_k \partial_l (\partial_i h \partial_j f). \tag{2.26}$$

We get at equilibrium (no external vertical constraints is applied) a system of equations on the vertical deflection and the Airy stress function:

$$\begin{aligned} D\nabla^4 w - L(\chi, w) &= 0, \\ \frac{1}{Y} \nabla^4 \chi = s(\mathbf{r}) - \frac{1}{2} L(w, w). \end{aligned} \tag{2.27}$$

With a defect free shell, it is possible to let the defect density vanish, and we recover the famous Föppl–Von-Karman equations for large deflections of thin plates [99]. Naturally, if we are to add an external constraint written p, Eq. (2.27) becomes:

$$\begin{aligned} D\nabla^4 w - L(\chi, w) &= p, \\ \frac{1}{Y} \nabla^4 \chi = s(\mathbf{r}) - \frac{1}{2} L(w, w). \end{aligned} \tag{2.28}$$

An analytical description of the internal stress and of deflections capsids is possible using the Föppl–Von-Karman equations within the context of deflections of thin plates. An additionnal term is added to take into account the presence of topological defects in the compatibility equation.

The Föppl–Von-Karman ratio γ is an important adimensionalized parameter that balances the in-plane deformation cost of a viral membrane and the out-of-plane one.

A very important dimensionless parameter arises in discussing spherical crystals with Eq. (2.28), the Föppl–Von-Karman number:

$$\gamma = \frac{YR^2}{D}. \tag{2.29}$$

It measures the ratio of stretching to bending moduli. When the Föppl–Von-Karman number is large, the protein subunits optimize stretching and bend away from their preferred radius of curvature, showing some degree of faceting.This is the case for some viruses such as the Hepatitis B Virus (HBV). Hence, the competition between in-plane energy and out-of-plane energy is evidenced very easily by the previous parameter. Faceted viruses shall exhibit a large γ contrary to non-faceted viruses.

2.3 NUMERICAL SIMULATIONS OF DEFLECTED MEMBRANES

The presented elastic model for shell membranes exhibiting defects is, apart from being very elegant, compatible with a numerical study. Previous equations have been widely used in the literature to address various problems of thin plate elasticity.

2.3.1 *In-plane energy*

From the latter continuous model, it is possible to derive a dicrete version of in-plane stretching energy and of out-of-plane bending energy to be minimized if we are to study numerically deflections of coarse-grained membranes and shells.

We define a stretching energy S on each bond in our 2D triangular lattice:

$$S = \frac{1}{2} k_e \sum_{\{a,b\}} (d_{a,b} - d_0)^2, \tag{2.30}$$

where $d_{a,b}$ is the length of the bond relating vertex a and b and k_e its rigidity (assumed uniform on all bonds). The sum is running through all bonds. Using this discrete in-plane energy enables us to test the predictions of the elastic analytical model regarding a membrane which Lamé coefficients are equal. They are evaluated as $\lambda = \mu = \sqrt{3}/4 \cdot k_e$. Referring to Eq. (2.16), it follows two very useful equalities on the Young modulus and on the Poisson ratio:

$$k_e = \frac{\sqrt{3}}{2} Y, \ \sigma = \frac{1}{3}. \tag{2.31}$$

2.3.2 *Out-of-plane energy*

Additionally, to simulate the deflection of our tessellated membrane, let us introduce the numerical bending energy:

$$B = k_b \sum_{\langle \alpha, \beta \rangle} [1 - \cos(\theta_{\alpha,\beta} - \theta_0)], \tag{2.32}$$

where k_b is the bending stiffness (also assumed uniform on all pairs of adjacent faces). $\theta_{\alpha,\beta}$ is the angle between the normal vectors of faces α and β respectively. θ_0 is a parameter reflecting a preferred curvature for the membrane. Numerically, this is equivalent to simulate a membrane which flexural rigidity D is opposite to its Gaussian rigidity, $D = -\kappa$. Finally, we get the relation [37, 94]:

$$k_b = \frac{2}{\sqrt{3}} D. \tag{2.33}$$

Taking the vertex mass $m = 1$, it yields the membrane mass density [108]:

$$\rho = \frac{2}{\sqrt{3}}. \tag{2.34}$$

2.4 CAUTIONS

We recalled briefly the main equations of elasticity on deflected membranes. When constructing the latter theory, we use two assumptions: the hypothesis of the straight normals and the hypothesis of an absence of reciprocal pressure of horizontal layers (See the end of Subsec. 2.2.2). The theory assumes that the deflections w are sufficiently large (they can be comparable with the shell thickness or larger), but they should remain small relative to other dimensions (for instance its arc length) and then finite. Due to previous assumptions, in-plane deformations and their respective derivatives $u_1, u_2, \partial_i u_j$ are also considered small compared to deflections w and the values $\partial_i w$. Those are quite reasonable for our studies: the deflection w occurs in the direction of the least rigidity, while the displacements u_1 and u_2 occur in the direction of the largest rigidity of the membrane. It is easier to bend adjacent proteins one in front of another rather than to separate them. Generally speaking, for proteins constituting viral capsids, we estimate $D \sim 20 k_B T$, while $Y \sim 200 k_B T / \pi m^2$ [8, 38, 87]. In other words, results that can be

derived using previous equations on curved topographies are obtained within a small curvature expansion deviated from a flat reference state. Therefore, previous equations *must not* be used to study closed elastic crystals but only unclosed ones (i. e. unclosed curved self-assemblies). Indeed, in closed curved shells, there is geometric frustration, implying that stress and strain are necessarily present and cannot vanish, they *do not* obey previous equations. To solve such problems, one should look for a perfect screening solution where the defect density is not zero and exactly equal to the curvature of the system. This can be done using a recent formulation of elasticity theory in curved geometries. It unifies its geometric and topological contents with the theory of defects [65, 111]. Nevertheless, within reasonable assumptions, it is possible to describe deflections compared to a spherical reference. Equations will be presented in Ch. 4.

3 SELF-ASSEMBLY PATHWAY

3.1 RÉSUMÉ

Dans ce chapitre, un bref état de l'art est proposé concernant l'auto-assemblage des structures virales. Encore une fois, une emphase est mise sur l'inclusion des précédents défauts topologiques (*i.e* les pentamères et les heptamères).

3.2 DISCLINATIONS AND CURVATURE

Recent simulations of viral self-assembly have shown that a wide range of capsids shape can be obtained by tuning essentially the spontaneous curvature of the surface [46, 62, 112]. In a very interesting letter published in 2009, Levandosky and Zandi showed that the specific form of conical HIV shells is not induced by a complex biological mechanism (such as the presence of a template or the influence of a surrounding membrane) but rather it is the natural response of an elastic sheet growing under simple rules of nonequilibrium assembly [62]. They used a two-step model: each time a subunit is added into the growing shell, an elastic relaxation of the partially formed structure occurs. The unit cell has the form of a triangular prism constituted of three triangles made smaller and smaller from top to bottom (See Fig. 3.1). This gives a spontaneous curvature to the built numerical sheet. Because of this curvature, it is possible to form disclinations. Indeed, in case of a flat sheet made of perfect hexagons, triangles possess a spontaneous angle α equal to exactly $60°$. Each time five triangles are assembled, it is possible to add a sixth one to realize another perfect hexagon. But the previously described cell creates in fact an opening angle slightly less than $60°$, hence, below a critical angle α_c, one can choose to stretch previous unit made of three layers containing five trangles each to create a "disclination". The system of springs is relaxed using the energy defined in Eq. (2.30), except that stiffnesses are non-uniform in the unit cell (See Fig. 3.1). Finally, they considered a deterministic growth: they assumed the attachment of each new unit cell at the place where the subunit maximizes the

number of intermolecular bonds, corresponding to a minimum of the energy landscape. That corresponds to a location at the growing edge with a minimum opening angle. Hence most probable places are determined by the values of the opening angle (if there are equivalent positions at the edge, then one of them is randomly chosen).

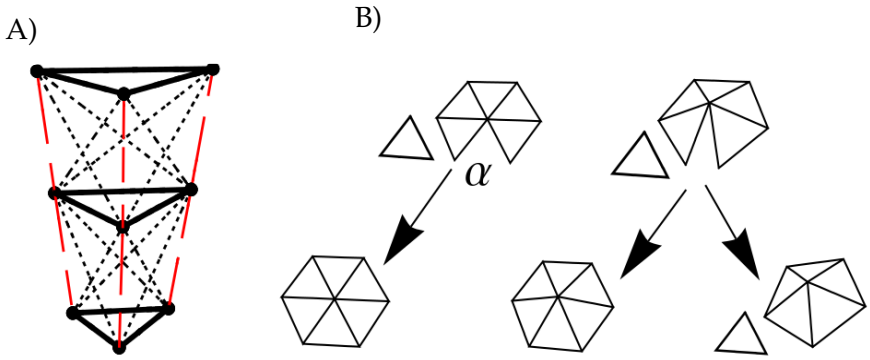

Figure 3.1 – A) The unit cell in the form of a triangular prism. Each line represents a spring, the equilibrium lengths of springs, of constant stiffness k, constituting triangles are set from top to bottom $a_0 + 2\Delta$, a_0 and $a_0 - 2\Delta$, so that the radius of curvature of the outer shell is set $R = a_0(1 + a_0/2\Delta)$. Dashed and dotted lines represent springs connecting the three layers of triangles which stiffnesses are respectively $k/2$ and $k/3$ to make the sheet elastically isotropic. B) The closure algorithm. Because of the presence of spontaneous curvature, the opening angle α is always less than 60° contrary to a perfect hexagon. Thus, below a critical angle α_c, the five existing subunits are to be stretched to form a "pentagon", i. e. a disclination. Figures and details are taken from Ref. [62].

Obviously, with increasing radius of curvature the shell size also increases. The interesting trend regards the shape of the resulting capsids that depends on the spontaneous curvature between triangular prisms. The previous trend is modulated by a deviation from spherical shape as one proceeds from the smaller radii of curvature to the larger ones (See Fig. 3.2). Generally, large spontaneous curvatures promote smaller opening angles and consequently facilitate the creation of pentagons, resulting into a structure very similar to an icosahedron (but not a perfect one). On the contrary, small spontaneous curvatures between subunits make the formation of pentagons energetically costly, keeping opening angles at values just slightly below 60°. In the end,

no pentagon is observed, resulting into very well defined cylindrical shapes (See Fig. 3.2).

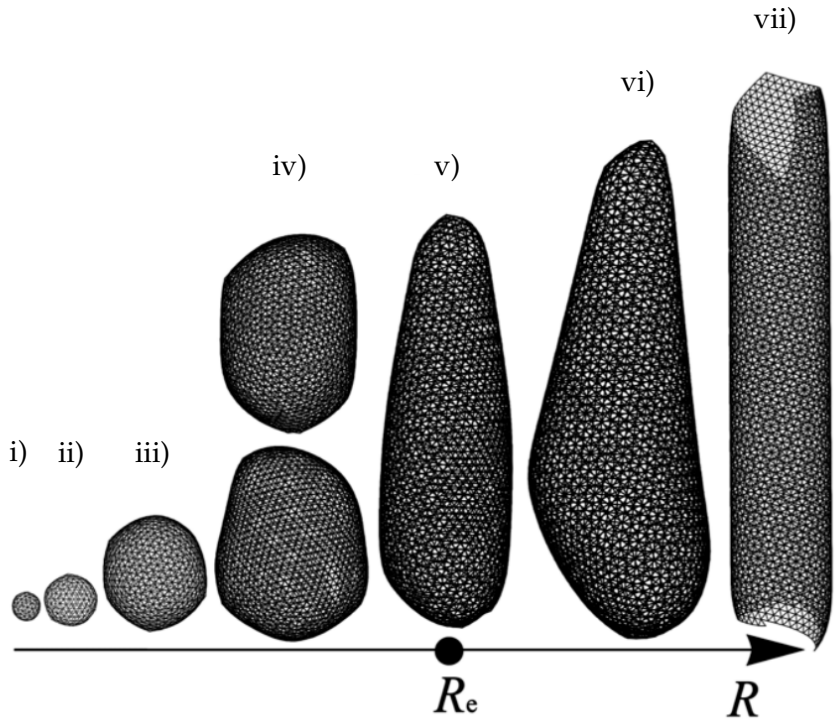

Figure 3.2 – Shapes and relative sizes of viral structures against the spontaneous radius of curvature, R, which is determined by the quantity Δ. Those structures were built using an algorithm described in the main text and in Fig. 3.1. Here a_0 is set to 1 and Δ is i) 0.2, ii) 0.15, iii) 0.1, iv) 0.08, v) 0.076, vi) 0.075, and vii) 0.072. A conical closed structure is obtained for $\Delta = 0.076$ that is $R_e \sim 7.5$. Figures and details are adapted from Ref. [62].

However, as it has been shown in Ch. 2, all viruses exhibit exactly 12 disclinations, required topologically. Notably, these pentamers are irregularly localized in elongated capsids, while they are equidistant in icosahedral capsids. The mechanisms underlying both the appearance and the localization of pentamers are poorly understood. Regarding spherical capsids, Castelnovo clearly highlighted the resulting benefit from the specific icosahedral symmetry in 2017 [30]. At each step of the self-assembly, by solving Eq. (2.27), it is possible to derive an energy composed of three terms, i) the intrinsic elastic cost to map the membrane onto a spherical substrate, ii) the self-energy of disclinations, iii) the pairwise interaction of disclinations. Each disclination helps

to screen out the geometric frustration due to the Gaussian curvature of the sphere. In the meantime, it appears that repulsive interaction among disclinations, as well as their repulsion with the free boundary, will contribute to distribute them regularly. As evidenced in Fig. 3.3, each disclination inclusion enables to delay the strong increase of the elastic energy. We recall here that the maximal net number of disclinations within the structure of a closed capsid is twelve. This net number is fixed topologically (See Ch. 2). It is shown in Fig. 3.3 that the regular distribution of these disclinations along the vertices of an icosahedron gives the lowest energy, compared to a random location for these disclinations. Even more interesting, we observe that icosahedral symmetry appears progressively, as a result of energy minimization upon regular inclusion of disclinations [64, 106, 112].

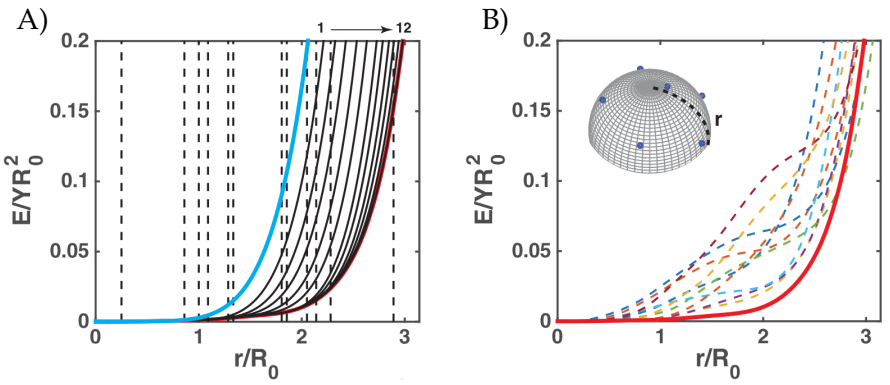

Figure 3.3 – Elastic energy for a spherical membrane as function of the intermediate size during viral self-assembly. Elastic cost of disclinations is taken into account after their inclusion in the membrane. A) Energetic cascade for disclination inclusion. Elastic energy for 12 disclinations with icosahedral symmetry (thick red line), compared to the energy of $n = 1$ to $n = 12$ disclinations (thin black lines). Dashed vertical lines indicate the radial positions of disclinations. The elastic energy without disclinations is shown by the blue line. B) Elastic energy for 12 disclinations with icosahedral symmetry (thick red line), compared to 10 realizations of random locations for 12 disclinations (thin dashed colored lines). Inset: Example of locations of six disclinations regularly localized on the shell growing at a constant curvature. Figures and details are taken from Ref. [30]

Disclinations help to screen intrinsic curvatures of shells. To close a capsid, it is energetically favorable to introduce a pentamer within the biological scaffold.

Regarding large viruses though, large icosahedral symmetries require scaffolding proteins. By studying the growth of large viral shells (capsids), Li and Zandi showed that a nonspecific template not only selects the radius of the capsid, but also leads to the error-free assembly of protein subunits into capsids with universal icosahedral order [64]. Using the continuum and discrete minimal model presented earlier (See Ch. 2), the growth of spherical large shells was investigated with a major supplementary ingredient: a Lennard-Jones potential enables to create an attractive force between triangular subunits and the preformed scaffolding layer. Again, at each step of growth, a new triangle is added to the location in the boundary which makes the maximum number of bonds with the neighboring subunits (this is justified with the same reasons given previously). For the case of the described template driven assembly, and additionnaly to the Föppl–Von-Karman number, one shall introduce a new adimensionalized parameter $\eta = D/\epsilon$. D is the previously defined flexural rigidity and ϵ quantifies the depth of the Lennard-Jones potential. For small η, multimers follow the inner core curvature during the self-assembly, whereas for large η, the spherical shell detaches from the core and follows its spontaneous curvature. The presented study is restricted to regimes where $\eta \simeq O(1)$ and $\gamma \gg 1$, thus the template rules the final size of the capsid. For viruses with $T \leqslant 4$, the inner core appears useless. However, as soon as T becomes greater than 4, the substrate is required. Consistently with previous assumptions, the growth of a large spherical cap ($T = 13$) is considered with an aperture angle θ that varies monotonically from 0 to π. For each value of θ the free energy is evaluated and the inclusion of a new disclination is considered. Once the latter is favorable, the defect is added. Two results deserve to be underlined, the first disclination is not centered, i. e. the cap grows initially defect-free. This is the result of the competition between the disclination self-energy whose minimum is at the boundary and Gaussian curvature–disclination interaction. Additionally, as the shell grows, the addition of disclinations becomes more and more favorable and each time a new energy valley for the formation of a new disclination emerges. On Fig. 3.4, the contour plots of total elastic energies are showed for spherical caps with $\theta = 0.8$ through $\theta = \pi$. The bigger ball in each plot indicates the position of the latest energy well, which is where the addition of the next disclination will take place. The agreement between the continuum model and the simulations is to be enlighted. During the growth process, disclinations always appear in

positions that eventually become the vertices of an icosahedron. To conclude, the final structure depends on the value of γ and of the size of the spherical crystal. Small spherical crystals, with $T < 4$ assemble spontaneously for any Föppl–Von-Karman number, whereas larger ones without a template, with $\gamma \simeq O(1)$ adopt configurations without specific symmetry. A template and a stretching dominant regime can have a significant impact on the structure and the symmetry of the shell.

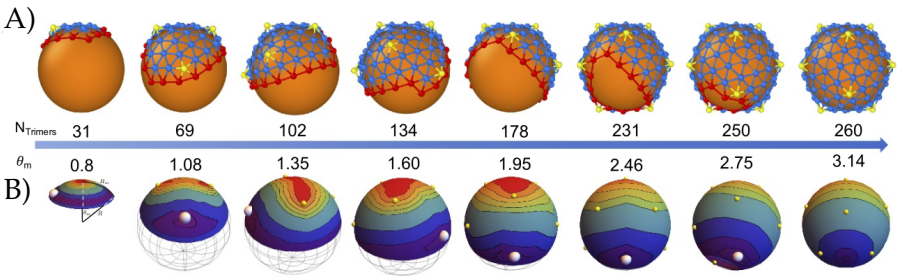

Figure 3.4 – The snapshots of a $T = 13$ growth in discrete simulation A) and continuum theory B). For the discrete part, the yellow vertices belong to pentamers, blue ones to hexamers, and red ones to the cap edge. The gold core mimics the preformed scaffolding layer or inner core. The caps for the continuum part denote the energy contour plots for the newest disclinations that appear in the purple energy well. The red region has the highest energy and the purple region the lowest one. There is a yellow ball in the position of each disclination. The largest ball corresponds to a newly formed disclination. Each valley corresponds to the position of a future disclination. Figures and details are adapted from Ref. [64].

However, in this section, we only discussed energetical consequences of disclinations but no mention was made about dislocations. We must take into account the other ubiquitous point defect and its fundamental role at play if we are to investigate two-dimensional crystals such as viral capsids.

3.3 DISLOCATIONS AND RELAXATION

In literature, a substantial amount of studies exist regarding dislocations. More particularly, for the simplest case of crystalline order on the sphere, the key feature is the appearance of scars, i. e. linear chains of dislocations around a central disclination that freely terminate

inside the crystal or at the boundary of it. They appear for crystals sufficiently large. Crystalline spherical caps are dislocation-free when its width R is comparable to its lattice spacing a, $R \gtrapprox a$ [6, 12, 14, 16, 77, 102]. In a very elegant experiment, the so-called scars even have been observed in systems of colloidal beads self-adsorbed on spherical water droplets in an oil emulsion [12]. The observation was done along with an associated triangulation to enlighten topological defects. As dislocations appear to be very common defects within condensed matter field, a wide range of analytic studies were done, and crystals with scars can be treated analytically and efficiently. In a seminal paper, Bowick *et al.*, using the Green function of the Bilaplace-Beltrami operator on a sphere, provided a way to evaluate the elastic energy of an icosahedral lattice. The latter evaluation takes into account i) disclination-disclination interactions, ii) disclination-dislocation interactions and iii) dislocation-dislocation interactions. More precisely, particular favored tesselations can vary from system to system with fixed "particle" number, depending, e. g., on details such as the defect core energies encrypted via the elastic constants [14, 15]. Interestingly, they showed that if a disclination is placed on the top of a cone and if the resulting crystal is forced into a spherical monolayer, scars radiate out of the disclination all the way to the boundary. We must add that the dislocation core energy within the lattice is small compared to the external stress introduced by the constant curvature. In simple words, m grain boundaries of finite length and variable spacings between dislocations form to reduce external stress in the resulting curved crystal (See Fig. 3.5). But, once again, since the resulting final configuration depends on nonuniversal features, such as dislocation and disclination core energies, curvature, and variate commensurability properties, only a general trend is presented here and all configurations should realize it in an approximate way. However, based on the asymptotic theory of caps within continuum limit of vanishing lattice spacing, Azadi *et al.* derived the morphological phase diagram of ground-state defect patterns for crystals on spherical substrates [6].

For large crystals, dislocations play a key role to relax internal elastic stress under various conditions. Additionnaly, fractures in colloidal crystals are more to nucleate near or on dislocations. However, their existence in viral shells is not certified, but they can be of significant interest in our work.

They studied the transition between neutral state and charged ground states of a crystalline cap subject to external boundary forces σ_b. The latter is added using a constant boundary condition (either tensile or compressive) on the radial stress. The phase portrait was also derived in function of the surface covered by the latter cap $\Phi = W^2/2R^2$, where $1/R^2$ was its gaussian curvature and W its circular radius. Before showing the latter phase portrait, one must outline the mathematical

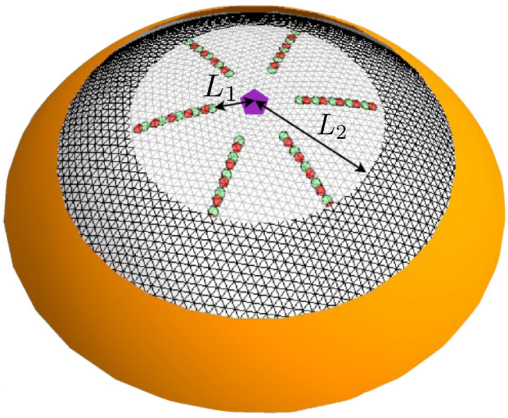

Figure 3.5 – A disclination surrounded by a cloud of aligned dislocations (scars). The central disclination is highlighted in purple and dislocations in red and green. To distinguish them, $+1/6$ and $-1/6$ charges are in red and green respectively. The resulting configuration, particularly lengths L_1 and L_2 or intermediate spacings between dislocations constituting scars depend on details encrypted in elastic constants, imposed curvature and size of the crystal. The gold inner core mimics the imposed curvature. Figure is taken from Ref. [6].

method and physical principles underlying it within the limit $b \to 0$, where b represents the norm of the Burgers vector. To construct such a stable pattern, one should note that a dislocation $\mathbf{b}$ in a stress field experiments the so-called Peach-Koehler force. The force acting on the dislocation is not a physical force (like mechanical force of springs or electrostatic force on a charged particle), but rather a way to describe the tendancy of the dislocation to move through the crystal when stresses are present. We write it as:

$$F_i = \epsilon_{ij}\sigma_{jk}b_k, \tag{3.1}$$

taking into account that the latter force is proportional to the elastic stress. Hence, two interacting dislocations experiment a stabilizing pull towards the boundary proportional to b^2. Then, a distribution of dislocations satisfying mechanical equilibrium in axisymmetric caps and polarized along the hoop direction is under zero force (like aligned magnetic dipoles) [2]. This defect polarization is consistent with scars added or removed along the radial direction to ease the collapse of compressive or tensile hoop stresses depending on the sign. Therefore, Azadi *et al.* sought perfect stress-collapses along the hoop direction.

This is formally equivalent to the notion of perfect screening of Gaussian curvature [52]. It results six distinct competing defect morphologies at low surface coverage in the (Φ, σ_b) plane. These are shown schematically in Fig. 3.6: Dislocation free states exist for all boundary forces and curvatures. There is a region where neutral scars exist (i. e. without a disclination), bounded by two critical tensions that depend on the surface coverage $\sigma_b < T_n^* = Y\Phi/2$ and $\sigma_b > -P_n^* = -Y\Phi/4$. The region of stable charged caps (scars and disclination) is bounded from below by a critical curve $\sigma_b = -P_*^c = -Y(1/12 - \Phi/2)$. One shall note that the charged center-bound scars state lies above the curve $\sigma_b = -P_{**}^c$, where P_{**}^c a tension such that, $P_{**}^c = 0$ if $\Phi < 1/12$ and $P_{**}^c = Y\Phi/4(1 - 1/144\Phi^2) + 1/24 \log 1/12\Phi$ otherwise (See Fig. 3.6).

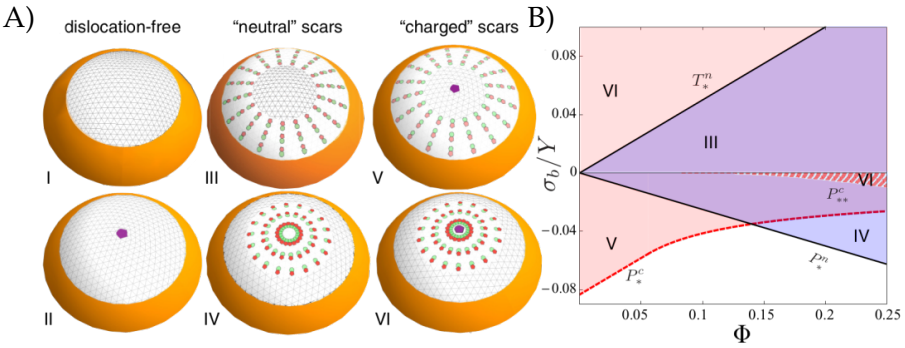

Figure 3.6 – A) The schematics of six possible states (defect morphologies I–VI) described in the text. B) The phase space spanned by surface coverage, Φ, and boundary stresses, σ_b, that delineate the regions of mechanical stability (existence) for the competing radial scar morphologies described in the core text. Figures and details are taken from Ref. [6].

Despite the precise study of this phase portrait, the latter is of great interest to show that positions of dislocations (low-energy defects relatively mobile compared to high-energy ones: disclinations) have an influence on the elastic resulting stress. Their configurations can help to screen a constant Gaussian curvature.

In a substantial numerical work Negri *et al.* showed that scars have a strong influence on crystalline stability if they are submitted to mechanical forces [72]. They considered a set of N colloidal particles confined onto a spherical substrate and interacting through a Lennard-Jones potential. As it has been said previously, the beads tend to group either into packs of 5 (disclinations) or into pairs of 5-7 packs (dislocations). Naturally, because of the spherical constraint, dislocations tend to align

themselves into scars. They submitted the resulting crystal to two main deformations, volumetric and deviatoric. In other words, on one hand to create a volumetric strain, they inflated the final shell, preserving uniform Gaussian curvature (change of volume). On the other hand, to create a deviatoric strain, they changed the shape of the shell preserving its surface constant, starting from a sphere to give an ellipsoid.

Under volumetric strain, as one could have expected, the shell cracks. The fact is that precise initial failures appear to be in scarified regions. Under deviatoric deformation, squeezing the spherical shell into an ellipsoid, one can observe the alignement of scars with the greater axis of the ellipsoid. The first behavior is attributable to the fact that grain boundary scars induce weak spots in the crystal, where cracks are easily nucleated. Dislocations introduce naturally non-null stress and strain fields. Regarding the second behavior, the Peach-Koehler force previously described shall arrange scars parallel to the longer axis following the tensile/compressive stress to reach the final ellipsoidal shape (See Fig. 3.7).

An important note is to be shared with the reader here. We have to specify that dislocations were not observed up to now in viral capsids. Nonetheless, many examples of thin biological structures exhibit them such as bacterial cell wall, bacterial flagella and cell membranes [18, 107, 110]. They are mathematically characterized in slightly different ways. Dislocations in viral capsids may be rare or non-existent due to their capacity to re-assemble while self-assembling. The self-assembly process may not be perfectly irreversible, in order to limit the number of "mistakes" and increases in energy, one can assume that proteins may detach and re-attach somewhere else to avoid the creation of an heptamer. The addition of an heptamer in the structure may be biologically and chemically inconvenient, thus a re-arrangement can probably occur. However, to our knowledge, no findings exist in literature that attest inexistence (or their incompatibility for the case of large capsids) of dislocations in viruses. Then, despite their still non-proven existence in our material of predilection, it can be of significant interest to include such defects in our work.

3.4 MOTIVATION

The brief state of the art proposed hereinbefore provides significant insights in disclination and dislocation inclusion mechanisms. Their

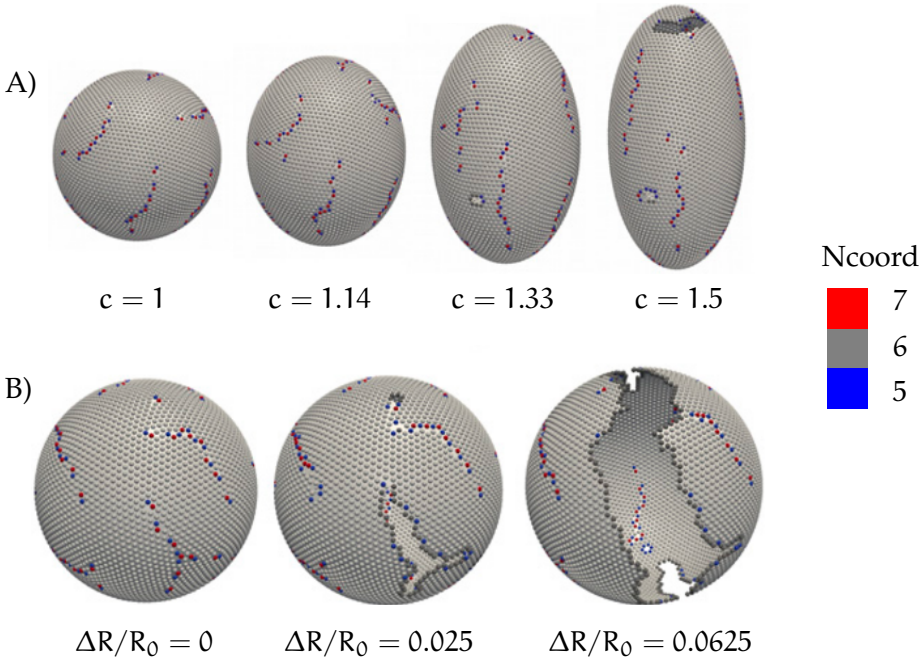

Figure 3.7 – A) Curved colloidal crystal under isotropic expansion, fracture appears along defects. The initial shell configuration (obtained by relaxing a random configuration of particles) shows topological defects already arranged in scars. R_0 represents the initial radius of the spherical crystal, ΔR its relative increase. B) Squeezing a colloidal crystalline sphere leads to plastic deformation mediated by grain boundary scars reorientation. The ellipsoid is deformed under the constant surface-area constraint. c represents the length of the semi-axis. 7-fold defects are represented in red on the snapshots, 5-fold in blue, 6-fold in grey. Figures and details are adapted from Ref. [72].

use to relax stress due to curvature during self-assembly of elastic crystals is not to be proven anymore. Disclinations help to relieve elastic stress by introducing a spontaneous local curvature. Specific patterns of dislocations arise to screen the latter itself, possibly created by an inner core. Those patterns depend also on external parameters (surface coverage and external boundary forces for instance). However, previous results were mostly obtained by minimizing the global energy of the surface as the surface is assembled. A description of defect nucleation mechanisms at the scale of a local subunit is still lacking in literature. We aim at curing this deficiency in the present work.

4 AFM, VIRUS AND DEFECTS

4.1 RÉSUMÉ

Au cours de ce chapitre, un second état de l'art est réalisé, concernant la nanoindentation de capsides virales. La nanoindentation à l'aide de microscope à force atomique est particulièrement utile pour "sonder" les propriétés élastiques de ces mêmes capsides.

4.2 INTRODUCTION

Nanoindentation experiments on the protein shells of viruses has established atomic force microscopy as a useful framework for probing the mechanics of large protein assemblies. Indeed, the stability and strength of capsids are crucial for viruses to infect their respective hosts through the cycle presented on Ch. 1. Moreover, an extensive study is required if capsids are to be used for biomedical and nanotechnological applications. Recently, a wide range of studies regarding indentation have been proposed. They investigate the latter phenomenon, on shells or specific viruses analytically, experimentally or numerically. We propose in this chapter a non-extensive and modest state-of-the-art to supplement previous chapters and conclude this part.

4.3 ATOMIC FORCE MICROSCOPY

Atomic Force Microscopy is a useful tool to probe the mechanical properties of viruses even at the nanoscale and to realize nanoindentation experiments. Viruses respond like springs for small indentation depths. It is thus possible to extract an effective stiffness.

To test mechanical properties of viruses, the most important and popular tool is the AFM. Nevertheless, due to the smallness of viruses, it is often very hard to get a good interpretation of the results and to relate the information to their biological characteristics. The use of this method reveals that viruses can be remarkably resistant to external (chemical or physical) sollicitations. In this section, we will summarize briefly main features of Atomic Force Microscopy. The AFM permits to acquire nanometric-resolution images and to extract the physical rigidity of the tested sample (a macromolecule, a virus, a cell, or even non-livig objects such as nano-antennas) [23, 32, 36, 63, 81, 93]. We will see further that it is also possible to test and compare resistances of

filled and empty capsids, to infer the influence of a mutation in the protein structure or even to detect the influence of maturation process on the effective stiffness. In a typical nanoindentation experiment, the tested sample is chemically attached to the substrate. A sharp tip is attached to a cantilever which back is illuminated by a laser diode. The reflection of the latter pulse to a four-segmented position sensor enabling to record the vertical movements exerted by the cantilever. The distance between the tip and the sample to be probed or imaged is controlled by application of a voltage to a piezo-electric crystal ("piezo"), which expands or contracts in a defined way. Imposing a piezo-extension while measuring the deflections of the cantilever enables to test the mechanical resistance of capsids under external applied loads. Usually, for small indentation, response is linear i. e. proportional to the deflection. The factor is called *effective spring stiffness* as the latter regime corresponds to a spring response. On the contrary for large indentation, non-linear behaviors appear. It is even possible to see discontinuities in experimental, force-distance curves. Those discontinuities are often interpreted as sample mechanical failures or micro-cracks. We call *maximal indentation* the value of the displacement at which a sudden drop appears on the curve. At this point, the sample is destroyed and the *breaking force* can be evaluated. Some mechanical observations done with an AFM can be interpreted using the continuum model of elasticity theory presented in Sec. 4.5. On Fig. 4.1 it is possible to see a sketch of an indentation experiment and typical force-distance curves.

4.4 EXPERIMENTS

Experimentally, for most viruses pentamers are softer than hexamers. The effective stiffness of viruses is in fact anisotropic and depend on their geometries, their shapes and their intrinsic structures.

A wide variety of studies exists in literature focusing on the mechanical properties of viral particles, and several articles adopt the perspective of structural and molecular virology to review the results obtained to date [69, 85]. Carrasco *et al.* showed a stiffness anisotropy of both virions (capsids containing DNA, i. e. active viruses) and capsids of the Minute Virus of Mice (MVM) [24]. After having evidenced relevant conformational rearrangements of the capsid on selected substrates, they measured effective stiffnesses using an AFM to indent the latter biological particles. These measures were taken along various symmetry axes (5-fold, 2-fold, 3-fold axes) shown on Fig. 4.2.

As said earlier, most spherical viruses possess an icosahedral symmetry. 5-fold symmetry axes pass through the vertices of the *matching*

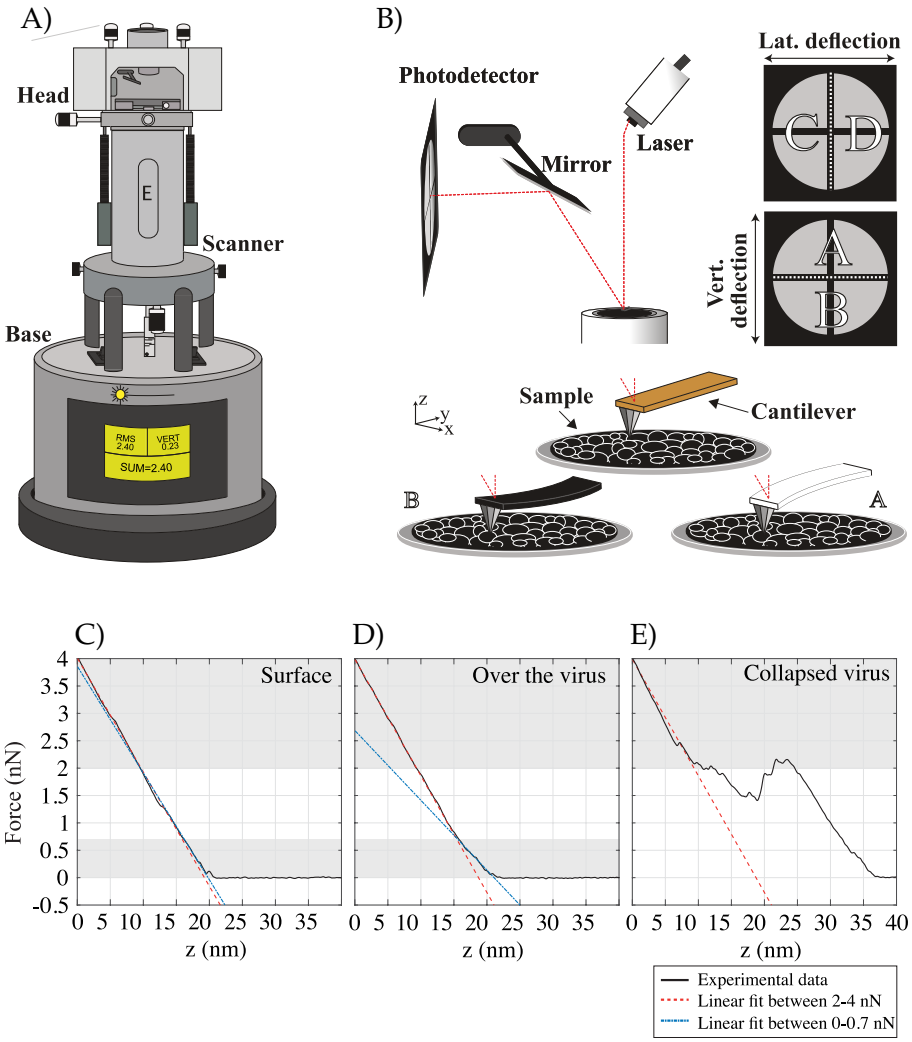

Figure 4.1 – A) Sketch of an AFM. B) Sketch of the experimental approach for investigating the mechanical properties of capsids by means of nanoindentation. A sharp tip approaches the sample to be tested. The tip is attached to a cantilever. Deflections of the cantilever due to tip-sample interactions are measured thanks to the reflection of the laser onto a photodetector illuminating the back of the former. C)-D)-E) Typical experimental force-distance curves acquired on capsids. C)-D) Responses are linear. $F = k_{eff} z$, hence, it is possible to measure an effective spring stiffness k_{eff}. The linear response of the surface is due to the deflection of the cantilever. Hence, one shall take into account the stiffness of the cantilever to measure the stiffness of the sample itself. E) The drop in the force-distance curve is the physical signature of a sample mechanical failure. The sample is broken. Sketches and curves were kindly given by Mme Carrasco-Salas.

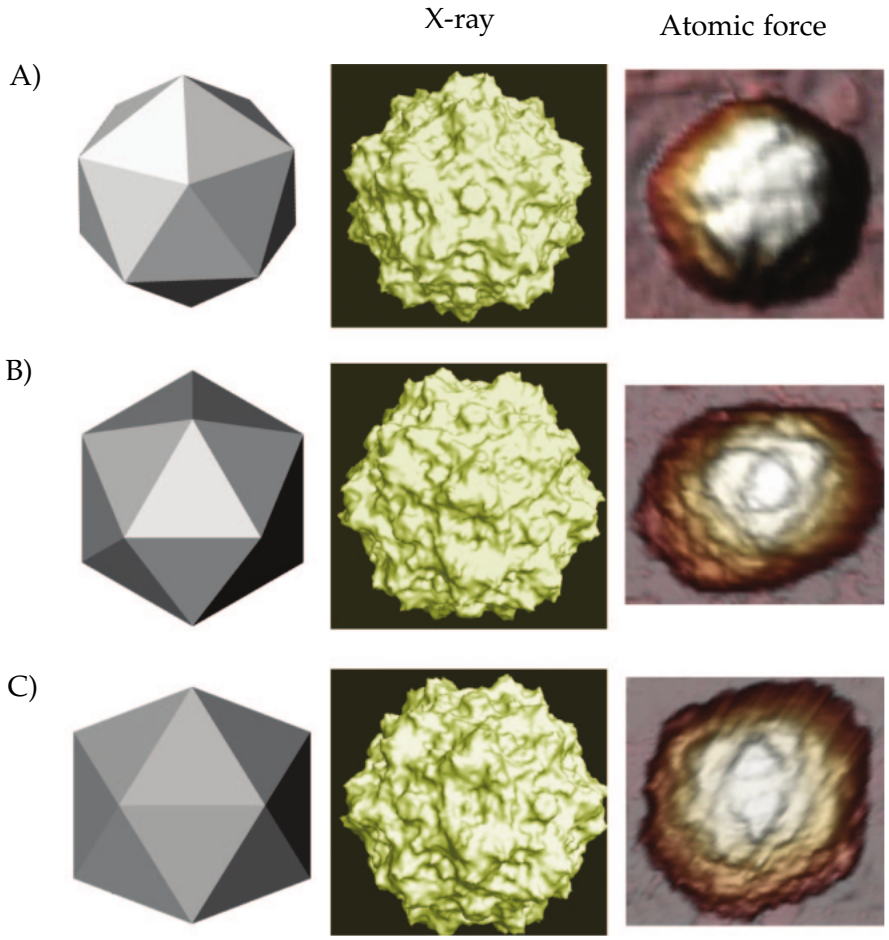

Figure 4.2 – MVM particles as viewed along fivefold A), threefold B), and twofold C) symmetry axes. Left side corresponds to simplified cartoons. Center images represent molecular surfaces derived from cristallographic data taken from The Protein Data Bank (PDB ID code 1MVM; Ref. [1]). Right side: $60\,\mathrm{nm} \times 60\,\mathrm{nm}$ AFM images of MVM particles. Figures and details are taken from Ref. [24].

icosahedral structure, 3-fold ones pass through centers of faces. Indentation along a 2-fold axis of symmetry corresponds to an indentation on one of the edges of the corresponding icosahedron. Due to the optimal distribution of disclinations highlighted by Castelnovo [30], disclinations are in fact located on 5-fold axes. Whatever the particles studied (virions or empty capsids of MVM), the effective stiffness of 5-fold axes is less than the two other symmetries. Results are shown in Fig. 4.3. For both cases, $k_{5-\text{fold}} < k_{3-\text{fold}} < k_{2-\text{fold}}$. This suggests that pentamers or disclinations are weaker, in terms of mechanical resistance, than the rest of the biological structure. Hence, experimental AFM results reveal an anisotropic mechanical stiffness of the MVM particle. Moreover, comparing DNA-filled capsids and empty ones, it is possible to assert statistically a mechanical reinforcement by external DNA. Using finite-element method simulations they showed DNA patches bound to the internal face of the MVM capsid can explain the observed reinforcement. The latter result is in agreement with Ref. [54] regarding WT phage.

In the same laboratory, the mechanical properties were interestingly manipulated by protein engineering. By mutating specific position of MVM virions and capsids, they showed a small dependence of the corresponding stiffness. Note that this dependence was also tested against the last three symmetry axes. The trend presented earlier remains interestingly unchanged [25]. The latter trend against protein mutations was also independently shown by Miguel *et al.* [70].

The effective stiffness that can be extracted from AFM experiments also depends on external parameters such as pH or the underlying substate-virus interaction.

Additionally, we wish to specify that viral stiffnesses can be strongly dependent on the environment, and on the global shapes of viral capsids. For instance, the size and the mechanical stability of norovirus can depend on pH according to Cuellar *et al.* [33] (See Fig. 4.4). The size of the particles tends to increase isotropicallly and linearly with the pH. This increase could be, according to the authors, due to conformationnal changes of the capsomers. The spring stiffness is nearly constant for $\text{pH} < 7$ with the error bars but drops for $\text{pH} > 7$, indicating a weakening of the stability.

Experiments presented in Klug *et al.* [60] also highlighted a stiffness reduction by a factor of three between the native pH 5 and intermediate pH 6 CCMV capsid. The softening from pH 5 to pH 6 can be due to local changes in the bonding environment (changes or interruptions in the protein-protein interactions) that act to weaken the capsid.

However Cuellar *et al.* appropriately highlighted that interaction with the mica support can induce spreading and thus reduce observed

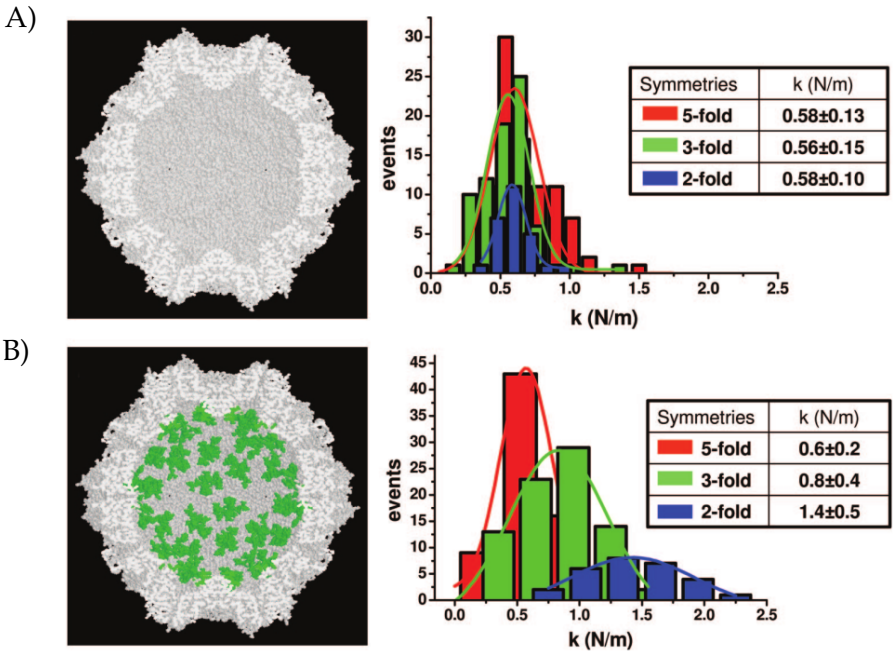

Figure 4.3 – Comparison of the mechanical properties of A) MVM empty capsids and B) virions. Left side gives the crystallographic structures of both particles using the program RasMol [92]. On the right side, the histograms are shown. The distributions of effective stiffness (spring constant, k) values is depicted for individual particles subjected to nano-indentation along fivefold (red), threefold (green), and twofold (blue) axes. Figures and details are taken from Ref. [24].

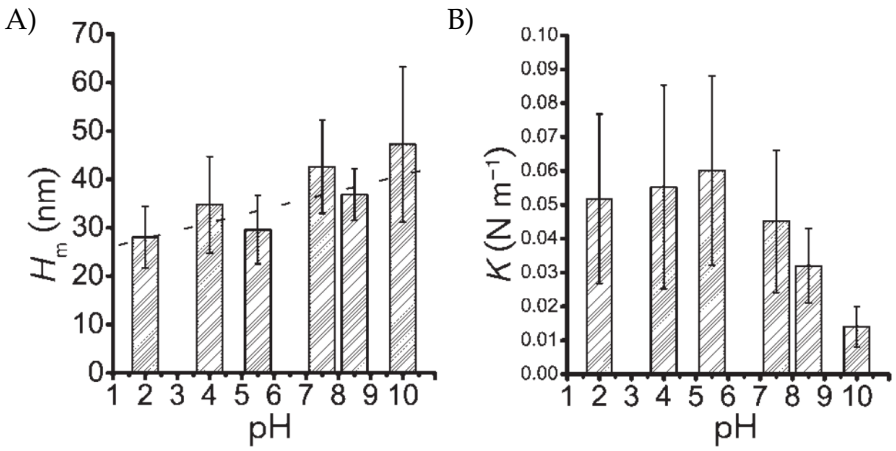

Figure 4.4 – A) Measured heights H_m of norovirus like particles as a function of pH. The dashed line shows the linear regression of H_c against the pH. B) Spring constant K as a function of pH, the error bars corresponds to the width of the median absolute deviation. The latter statistic was calculated from the slope in the linear region of the force-separation curve for at least 50 particles. Fig. adapted from Ref. [33].

heights as this interaction may also be pH dependent. Indeed, contact mechanics for small icosahedral viruses shall not be negligible according to studies realized by Zeng *et al*. They showed significant changes in height distribution of the Brome Mosaic Virus (BMV) if the virions were attached to mica substrate or Highly Oriented Pyrolytic Graphite (HOPG) one [113]. Similarly, Llauró *et al.* reported experimental evidence of the modulation of mechanical properties of the Tomato Bushy Stunt Virus (TBSV) by calcium ions [67].

As said earlier, for viruses with exotic shape such as bacteriophages, non gaussian distributions of stiffnesses can be extracted from nanoindentation experiments. Two complementary studies were led by Carrasco and Ivanovska *et al.* on bacteriophage Φ29 [26, 53]. The virus possess an ovoid shape, the shell of the Φ29 prohead is constructed from 235 capsomers arranged with 11 pentameric plus 20 hexameric units forming icosahedral end caps. 10 hexameric units form the cylindrical equatorial region. At one of the end caps, the connector complex replaces the last pentamer [26, 51, 109]. Because of this exotic appearance, Φ29 reveals complex elastic properties. Focusing on Carrasco's result, the experimental spring stiffness depends obviously on the selected prohead adsorption geometry (that is, up right or laid down, See

Fig. 4.5). Upright proheads exhibit a stiffness of $(0.075 \pm 0.020)\,\mathrm{N\,m^{-1}}$ whereas laid down ones exhibit $(0.192 \pm 0.034)\,\mathrm{N\,m^{-1}}$. Consequently, laid-down proheads are approximately three times stiffer than upright ones. The authors checked that the spring constant of the upright proheads does not depend on the particle geometry adsorption (the position of the connector, top or below is irrelevant). One can interpret this by advancing that the connector must be more compliant and more deformable (because of its hydrophobicity) than the shell. Proheads that are attached through a nondeformed connector would be perhaps too unstable for infectious processes.

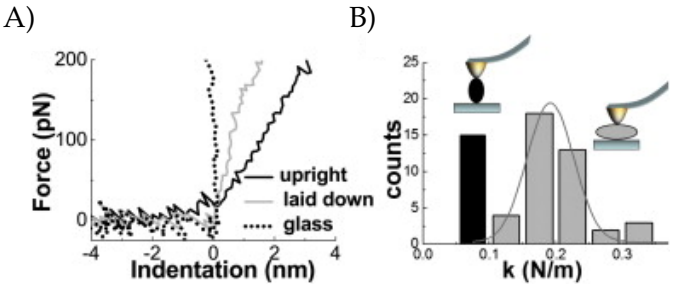

Figure 4.5 – Nanoindentation experiments of Φ29. A) Typical forward indentations curves on different locations, i. e. on glass substrate (dotted), on the up right configuration (grey), on the laid down configuration (black). B) Classification of the indentation curve slopes, as previsouly, up right configuration is in grey and laid down one in black. Note the decrease of the spring stiffness in the second configuration. 56 indentations were carried out on 5 uprigth capsids and 6 laid down ones. We shall report that in the upright dataset, two proheads were adsorbed through the connector, two through the capped-end and one remains unidentified. Figures taken from Ref. [26].

From those studies, one can conclude that variations of the elastic response can arise either from inhomogeneity of the material (e. g. its thickness, its topological distribution) or from variations in local curvature. Indeed it should be harder, for instance, to indent a convex area than a flat one. The biochemical environment also influences greatly the mechanical properties of capsids. In the following section, we present several numerical and analytical attempts to elucidate those variations.

4.5 CONTINUUM MODEL, SCALING

4.5.1 *Scaling*

Several attempts exist to derive the effective spring stiffnesses of capsids in function of their characteristics or the mechanical properties of their materials (i. e. the Young modulus, the bending rigidity, the radius, etc). Within thin shell approximation, it is assumed that the elastic response is obtained by balancing the bending energy and the stretching energy. For small deformations i. e. in linear regime, the scaling is made on a bounded region d. The inverse or mirror buckling is not considered in this case. Thus, evaluating the difference in energy between the newly deformed regime and the former one is possible. Indeed, the deformed regime possess on the bounded region a bigger radius of curvature compared to the initial one, the bounded region is flattened. Assuming the equilibrium, the force-distance law reads [21, 61]:

Scaling relations enable to extract approximate analytical values for effective stiffnesses of viruses that depend on their Föppl-Von-Karman ratio γ.

$$F \sim \frac{D}{R^2}\sqrt{\gamma}\Delta, \tag{4.1}$$

where Δ is the indentation depth, F the deforming force, D the previously defined bending rigidity, R the initial radius of the capsid and γ the Föppl–Von-Karman ratio. For small deformation at least, the effective spring-stiffness scales as $\gamma^{1/2}$. The latter result has been widely tested in the literature (See Ref. [8, 33, 53, 114, 117] for a review).

When the axial load exceeds a critical value, the curvature of the shell is spontaneously inverted, the shell snaps. The bending energy comes primarily from the small strip connecting the inverted part with the non-inverted one. The stretching energy is dominated by the deformation along the circles of constant latitude in the inverted part. Again, balancing those two contributions at equilibrium enables to get a non-linear force-distance relation [21]:

$$F \sim \frac{D}{R^{3/2}}\gamma^{1/4}\sqrt{\Delta}. \tag{4.2}$$

In the non-linear regime, the force-distance law is no longer that of a spring but rather has square root dependence on Δ. Note that the latter relation is valid only if indentation depth does not exceed the initial radius of the cap. Moreover, it is restricted to spherical viruses where the response is invariant under rotation of the shell.

4.5.2 *Deviation from Föppl–Von-Karman equations*

Analytically, it is possible to use Föppl–Von-Karman equations to describe deformation from a spherical substrate (See Eq. 2.28 in Ch. 2). However, they cannot be used to study deflection of spherical elastic shell and more particularly indentation of viruses. The curvature is in this case non-negligible compared to the size of the shell, and the hypotheses to use them are not valid anymore. In this case, the equations used are known as the Donnan-Mushtari-Vlasov equations (DMV). We provide hereafter an easy (but highly non-rigorous) route to derive DMV equations. This proof enables to find most of the terms of the equations. They are obtained by assuming a two-step deformation. A first one passing from a flat state to a spherical one with solutions (in polar coordinates $\mathbf{r} = \{r, \theta\}$ using the Monge gauge parametrization presented earlier):

$$\begin{aligned} w_0(r) &= \frac{r^2}{2R_0}; \\ \chi_0(r) &= \frac{YR^4}{R_0^2}\left(2\frac{r^2}{R^2} - \frac{r^4}{R^4}\right); \\ p_0(r) &= -\frac{\Delta\chi_0}{R_0}. \end{aligned} \tag{4.3}$$

Donnan-Mushtari-Vlasov equations are of significant interest to study analytically indentation of viruses. However, no analytical attempts to our knowledge exist in literature to study influence of defects while the elastic shell is under external constraints.

In simpler words, we impose a parabolic deflection using the external vertical pressure p_0 to approximate a spherical one of Gaussian curvature $1/R_0^2$. Then, we compute the resulting Airy function and pressure to get such a deflection. Let us note that these solutions are valid in a domain of reference $r \in [0, R]$ and absolutely not at $r \to \infty$. Then, one can seek perturbed solutions assuming that the final quantities are written $w = w_0 + w_1$, $\chi = \chi_0 + \chi_1$ and $p = p_0 + p_1$. Then, w_1, χ_1 and p_1 are solutions of the system:

$$\begin{aligned} \frac{\nabla^4\chi_1}{Y} &= -\frac{\nabla^2 w_1}{R_0} - \frac{1}{2}L(w_1, w_1); \\ D\nabla^4 w_1 &= \frac{\nabla^2\chi_1}{R_0} + L(w_1, \chi_1) + p_1 + L(w_1, \chi_0). \end{aligned} \tag{4.4}$$

We note here that the last term of the second equation $L(w_1, \chi_0)$ is of order $1/R_0^2$ and can be neglected if the shell is considered shallow (the displacements by modulus are equal or exceed the shell thickness but are considerably less than other linear dimensions of the shell). Consequently, we obtain (provided previous assumptions) governing

differential equations of non-linear theory of shallow shells of constant curvatures:

$$\begin{aligned} \frac{\nabla^4 \chi_1}{Y} &= -\frac{1}{2} L(w_1, w_1) - \frac{\nabla w_1}{R_0}; \\ D\nabla^4 w_1 - \frac{\nabla^2 \chi_1}{R_0} - L(w_1, \chi_1) &= p_1. \end{aligned} \tag{4.5}$$

Obviously, this was a very simple approach to DMV equations, a rigorous derivation of governing equations of non-linear theory of shells has been made taking into account rotations in strain–displacement and equilibrium equations leading to non-linear relations. However, in-plane displacements are still neglected in front of out-of plane ones i. e. the stiffness of the shell in the tangent plane is significantly greater than the flexural one. More rigorous Vlasov and Reissner's approach [82, 83] enables to re-write Eq. (4.5) as follows:

$$\begin{aligned} \frac{\nabla^4 \chi}{Y} &= -\frac{1}{2} L(w_1, w_1) - \nabla_k^2 w; \\ D\nabla^4 w_1 - \nabla_k^2 \chi - L(w_1, \chi_1) &= p_1, \end{aligned} \tag{4.6}$$

where ∇_k is called Vlasov's operator written, in cartesian coordinates, $\kappa_1 \partial_x^2 + \kappa_2 \partial_y^2$, κ_1 and κ_2 being the principal curvatures in the directions of coordinate lines. It is obvious that if $\kappa_{1,2} \to \infty$, one recovers equations that describe large deflections of thin plates presented in Ch. 2.

Additionally, topological defect distributions are not described in this context. We note however that, if we were to describe and study indentation of spherical membranes, only a point force load $p_1 = \delta(r)/2\pi r$ would have to be injected in Eq. (4.6). This point force is the easiest route to get an analytical force-indentation relation, even though such a force is not realistic from the nano-experimental view point. Indeed, due to the smallness of viruses, AFM tips exert a load more compatible to the one obtained with a hard sphere. Nevertheless, previous assumption enables to get an interesting result (See Subsec. 4.5.3).

4.5.3 *Solutions*

Such a study has been significantly advanced by Vella *et al.* [104, 105]. They derived an effective stiffness for a pressurized shell $F \sim k\delta$,

where δ represents the indentation depth, k the effective stiffness and F the point force intensity:

$$k = \frac{4\pi D}{l_b^2} \frac{(\tau^2 - 1)^{1/2}}{[\tan^{-1}(1 - \tau^{-2})]^{1/2}}. \tag{4.7}$$

DMV equations enable to recover analytically scaling results.

$l_b = (DR_0^2/Y)^{1/4}$ is a natural bending length scale and $\tau = \frac{1}{4} p R_0^2/\sqrt{YD}$ a dimensionless pressure, R_0 the radius of the spherical membrane, p the internal pressure. Note that, if τ becomes negligible compared to 1, the unpressurized result of Reissner and Buenemann is recovered $k = 8D/l_b^2 \sim D/R^2 \cdot \sqrt{\gamma}$.

4.5.4 *Cautions*

Nevertheless, for large Föppl–Von-Karman number γ, other scalings permit to deduce that disclinations are stiffer than planar hexamers. For a capsid with large γ, it is a lot easier to bend the viral shell rather than to strecth it. Spherical viruses exhibit a faceted shape that resemble an icosaheder for $\gamma > 200$. Pentamers point out of the capsid.

Continuum mechanics, as a first approximation, has provided very useful information about elastic properties of viruses. Nevertheless, a continuum description cannot capture the discrete nature of subunits forming the capsid. More specifically, it does not capture the previously presented stiffness anisotropy against orientations of MVM. Let us highlight that previous model and scalings do not take into account influence of topological defects in the membrane constituting viral capsids. Additionally, to our knowledge, such a model considering both effects (indentation and defects) is still lacking in literature. As from the structural point of view, those defects are associated with a few numbers of capsomers structured by five proteins (pentamers) instead of six (hexamers), one shall take into account the discreteness effect of the packing. By modeling proteins constituting the capsid by triangles, it is possible, in an approximate way to reproduce the molecular structure. Hexamers become perfect planar hexagons (6 equilateral triangles) while pentamers point outward the viral capsid if proteins are considered particularly stiff, therefore curving locally the region (cf Fig. 3.1 in Ch. 3). Such models have been mostly studied numerically, as we will see in Sec. 4.6.

However, several authors tried to extend previous scaling for stiffness estimates modifying the stretching contribution to the energy. They tried to estimate the stiffness of a disclination located at the summit of the matching icosaheder for spherical viruses. In the limit of large Föppl–Von-Karman numbers, the stiffness response to forces applied on icosahedron edges and summits have been studied by Widom *et al.* [108] and Timoshenko [100, 101] . We recall that, in this limit, spherical viruses resemble icosahedrons and exhibit a faceted shape. We expect

then different scalings against material properties due to the geometry and the new aspect of viruses. Considering the indentation on a flat triangular face, that is an hexamer of the idealized icosaheder, solving Föppl–Von-Karman equations with appropriate conditions leads to:

$$k_{\text{hexamer}} \sim \frac{Y}{\gamma}. \tag{4.8}$$

Let us now suppose the indentation is done on a vertex, that is a pentamer. Assuming that the bending and strain energy persist along the length of the ridges linking the different summits and that the force is transmitted along those ridges, the stiffness scales as:

$$k_{\text{vertex}} \sim \frac{Y}{\log \gamma} \tag{4.9}$$

Consequently, within the large γ limit, we expect vertices to be stiffer than faces. Nevertheless, within the latter limit, it should be then possible to distinguish vertices from faces numerically and experimentally.

4.6 NUMERICAL VIEW POINT

Different types of simulations of nanoindentation experiments, accounting for the discreteness of the capsid at diverse resolution levels, have been presented in literature. To get numerical capsids to indent, elastic networks are predominantly used. The elastic hypothesis is efficient to study buckling and deformations in the linear regime, but they cannot easily account for breaking events. On the contrary, reducing the coarse-graining and introducing more realistic interactions in simulations can make them incredibly costly. In the following, we present typical numerical nanoindentation experiments that appeared relevant in our framework. Obviously, we recall here that the following state of the art is non-exhaustive and numerous pertinent studies non presented though existing can be found in the literature.

In a careful study led in 2008, Gibbons and Klug tested and extracted numerically various effective stiffnesses for the CCMV capsid. They used methods developed to construct volumetric finite element meshes of macromolecules that enabled them to create a coarse-grained three-dimensional model that adhere to geometric details of the capsid structure [11, 39, 115, 116]. They constrained the resulting numerical capsid between a flat hard plate and a rigid hemisphere of radius 20 nm to model the AFM tip. We recall here that CCMV has an average radius

similar to the one given to the tip. Additionally, they included an AFM response, i. e. a tip displacement to model the cantilever stiffness in the simulation. To match the experimental spring constant value $k^{exp}_{CCMV} \sim 0.15\,N/m$, the Young modulus of the model was tuned for the native CCMV capsid, with a value set to 215 MPa giving the best agreement. The relaxation of the system is done using the gradient of the deformation, to make the most appropriate choice of vertex displacements. Very interestingly and fortunately, they investigated, as previously though numerically, the stiffness heterogeneity of CCMV, against the three orientations, 2-3 and 5-fold axes of symmetry. Even though the difference between the orientations is not very strong, previously given inequalities and observed on another virus by Carrasco *et al.* still hold (See Fig.4.6). According to the authors, stiffening may correspond to discrete changes in contact geometry as additional capsomers contact the AFM tip. Modeling the AFM cantilever as a linear spring enabled them to underline its role: a stiffer cantilever would more accurately represent the nonlinearity of the capsid response. However, from an experimental view point, this also decreases the signal/noise ratio of the tip deflection measurement, leading to overall less accurate measurement of the capsid response. We thought that this latter result deserved to be pointed out considering its relative importance for experimental investigations.

Numerically and experimentally, when indented vertically, disclinations are softer than the rest of the shell. However, for large Föppl–Von-Karman numbers (mostly non realistic biophysically for viruses), the latter trend is reversed.

Deciphering the elastic behavior of HBV, Roos *et al.* also verified orientationnal dependence of the elastic stiffness, confronting both Finite Element (FE) Simulations and Molecular Dynamics (MD) Simulations to experiments [86]. For small deformation at least, the three of them coalesce at the nanoscale with a special advantage for MD simulations that do not need to be tuned with experimental data compared to FE analysis to perform scalings.

The previous trend regarding the stiffness and symmetry axes has been found numerically for other viruses possessing other geometries (i. e. T-numbers) and also with simpler coarse-grained models and relaxation processes, where capsomers are simply represented by spheres interacting through a Lennard-jones Potential [3, 29, 45] and relaxed using the well-known Langevin dynamics [55, 76].

Buenemann and Lenz studied mechanical limits of viral capsids with the Föppl–Von-Karman number γ varying on a large interval, from 10 to 2000 [20]. This investigation regards specific geometries for specific viruses such as $\Phi 29$ or the latter CCMV. Nevertheless, the coarse-grained model is very similar to the one proposed by Seung and Nelson,

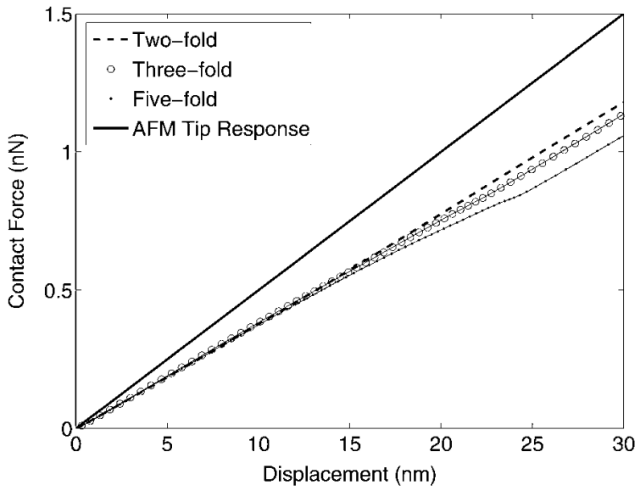

Figure 4.6 – Contact force curves for the native numerical CCMV indented on each of the rotational symmetric orientations, as a function of the total displacement, which includes also AFM tip displacement. The stiffness of the cantilever of the AFM is set to $k \sim 0.05\,N\,nm^{-1}$. Figure is taken from Ref. [39]

giving the study a general character as they could systematically vary elastic moduli and geometries of capsids to probe their mechanical responses against external disturbances. Viruses were indented radially and precisely on a point to consider the precise difference between hexamers and pentamers. Relaxation of the numerical structure is done here using conjugate gradient algorithm [80]. For small indentation, compared to the radius of the studied capsid, it appears that the latter scaling given for k (unpressurized case) in Eq. (4.7) agrees well with numerical simulations, and pentamers are softer as reported before. However, for their model, and because of discreteness effect, for $\gamma > 500$, the numerical capsid gets a faceted shape, and pentamers appear to be slightly stiffer than hexamers.

After a certain depth of indentation, the capsid buckles, and this event only occurs with the indentation of pentamers. For even larger γ, $\gamma > 2000$, the effective stiffness of hexamers grows like $Y\gamma^{-2/3}$, whereas for pentamers a linear dependence to Y is extracted (See Fig. 4.7).

Hence, from those studies, one can assert that viruses possess stiffness heterogeneities due specifically to their geometries but also on the materials they are constituted of.

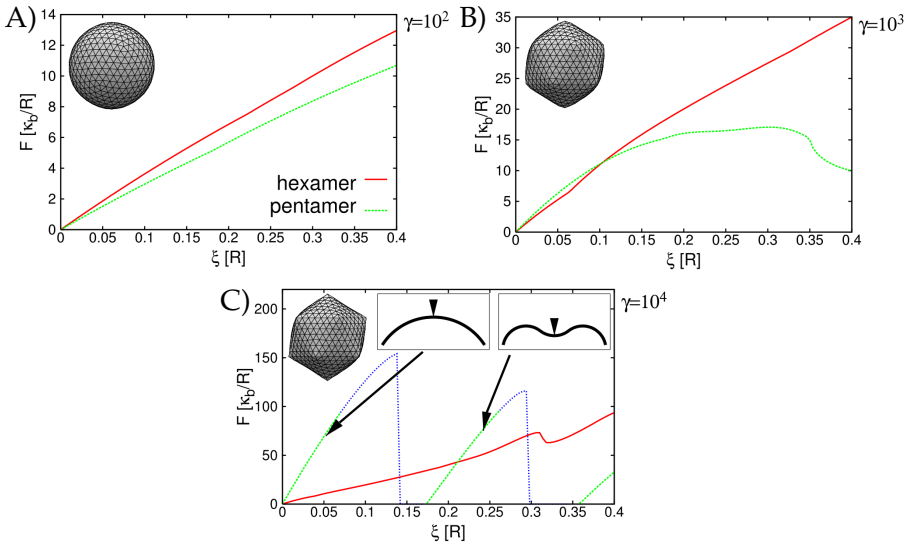

Figure 4.7 – Force-distance relationships of locally deformed viral shells. ξ is the normalized indentation depth with the radius of the numerical shell R, F is scaled by κ_b/R where κ_b is the flexural rigidity here. A) For small γ, regimes are linear with an effective stiffness proportional to $\sqrt{\gamma}$. B)-C) Above the critical threshold γ_c, stiffness heterogeneity appears with the faceted shape. For $\gamma \sim 1000$, pentamers are stiffer than hexamers and for a strong indentation, pentamers buckle in the viral shell, causing softening. For $\gamma > 2000$, pentamers may even snap into a new stable inverted configuration, which creates discontinuities in the force-distance function. Figures and details are adapted from Ref. [20].

4.7 MOTIVATIONS

As said in the introduction of this chapter, AFM is a remarkably useful tool to probe the mechanical properties of viruses at the nanoscale. All experimental observations are relevant since they address the global stability of viruses, as well as their deformability. Nowadays, the constant growth of the computational power enables to develop more and more precise numerical nanoindentation simulations. Those are also of interest to provide insights into viral resistivity at the molecular scale. Most works dealing with nanoindentation of viruses have focused on their linear response. Focusing more specifically on icosahedral viruses, the three main symmetries (2-fold, 3-fold and 5-fold) strongly suggest that elastic properties of capsids are not uniform throughout the molecular structure. Additionally, differences in stiffness for identical experiments were traced back again to the orientation of virus adhesion. Those were consequently interpreted as signatures of the asphericity of the virus.

Scalings and analytical models proposed in literature mostly assume point-indentation to rationalize both numerical and experimental results. Most results were also analyzed assuming top-indentation. Nevertheless, one can think that AFM tip shapes and tip positions have an influence on the induced elastic deformation during an indentation experiment. The response might then be different. Due to the smallness of viruses, it is perhaps preferable to model AFM tips as spheres which radii are comparable to viral sizes. Tip thermal drifts are sometimes inevitable too in experiments. Those can also be non-negligible regarding the typical working scale of a few nanometers. Investigate tip position dependence can also be of significant interest for the interpretation of experimental results. We hope to familiarize ourselves with such dependences in this work.

Part II

MECHANICAL STRESS RELAXATION IN SELF-ASSEMBLY

Depuis la montagne jusqu'au cristal le plus menu , depuis le lichen jusqu'aux chênes de nos forêts, depuis le polype jusqu'à l'homme, tout dans la nature terrestre possède du style, c'est à dire l'harmonie parfaite entre le résultat et les moyens employés pour l'obtenir.

– *Eugène Viollet-le-Duc*

5 GROWTH ON A CURVED SUBSTRATE

5.1 RÉSUMÉ

Dans cette partie autant que dans ce chapitre, un modèle élastique de nucléation de défauts est proposé. En particulier, dans l'hypothèse d'un auto-assemblage irréversible d'une capside virale sphérique, on montre que les pentamères (respectivement les heptamères) sont le plus susceptibles de se former respectivement dans les régions où la tension azimuthale (selon la circonférence) en bordure de calotte protéique est le plus compressif (respectivement le plus extensif).

5.2 INTRODUCTION

To make an analytical model and to propose a defect nucleation mechanism, we write the equations regarding thin plates elasticity in a polar frame. We will study the self-assembly of a crystalline spherical cap forced to adopt a constant curvature.

We have seen earlier that individual molecules such as capsomers for the viral case can acquire a collective behavior to self-assemble. For spherical viruses, icosahedral structure is mostly observed. Capsomers tend to be hexamers, but because of a topological constraint (i. e. to create a closed shell), 12 pentamers (i. e. positively charged defects: disclinations) arise in the final structure. Additionally, no topological restrictions exist against the introduction of heptamers (negatively charged defects) in large capsids provided they are attached to pentamers to create dislocations which have a zero charge. It is thus possible to introduce an infinite number of dislocations in the molecular self-assembled system. However, the progressive arising of such defects in the crystalline order of the biological shell and physical mechanisms that drive them is still far from clear. This work, we hope, will contribute modestly to a deeper understanding of the latter phenomenon.

5.3 EQUATIONS IN A POLAR FRAME

5.3.1 *Back to basics*

Self-assembly of hexamers results into a perfect planar surface, whereas disclinations help to introduce curvature leading to a buckled

structure, even if same building blocks are used. Therefore, the closure of capsids requires those pentamers, but where and how to include them in the structure ? To answer this question, we will consider a curved elastic triangulated surface growing on a spherical scaffold. The important role given here to an inner core is reasonable. Indeed, several large viruses assemble onto scaffolding proteins that play a key role in the physico-chemical process. For instance without them, subunits of the Infectious Bursal Disease Virus (IBDV) assemble into a $T = 1$ capsid. One can also mention the Reoviridae virus family which viruses possess a multishell structure that can also act as inner cores. In this section, to get theoretical insights, we will model the growing surface as an elastic sheet. Consequently, we will briefly recall the classical framework of thin plate elasticity, writing previous equations in a cylindrical frame (See Ch. 2).

Let us consider a flat disk of radius R with negligible thickness, i. e. $h \ll R$. The latter disk is then forced to adopt a curvature equal to $1/R_0$. Using polar coordinates $\mathbf{r} = \{r, \theta\}$, we characterize an in-plane elastic displacement with $\mathbf{u} = (= \{u_r, u_\theta\}$. The out-of-plane displacement is characterized by the deflection $\mathbf{w}$. As we are to consider the large-deflection case for the disk, we recall the two non-linear Föppl–Von-Karman equations. They couple the Airy stress function $\chi(r, \theta)$ and the deflection, or vertical deformation, $w(r, \theta)$ taking into account the elastic cost of defects:

$$\begin{aligned} \frac{\nabla^4 \chi}{Y} &= s(r, \theta) - \frac{1}{2} L(w, w); \\ D\nabla^4 w &= L(w, \chi) + p(r, \theta). \end{aligned} \tag{5.1}$$

In polar coordinates, the L operator is defined as follows:

$$\begin{aligned} L(w, \chi) = \frac{\partial^2 w}{\partial r^2} \left(\frac{1}{r} \frac{\partial \chi}{\partial r} + \frac{1}{r^2} \frac{\partial^2 \chi}{\partial \theta^2} \right) + \frac{\partial^2 \chi}{\partial r^2} \left(\frac{1}{r} \frac{\partial w}{\partial r} + \frac{1}{r^2} \frac{\partial^2 w}{\partial \theta^2} \right) \\ - 2 \frac{\partial}{\partial r} \left(\frac{1}{r} \frac{\partial \chi}{\partial \theta} \right) \frac{\partial}{\partial r} \left(\frac{1}{r} \frac{\partial w}{\partial \theta} \right), \end{aligned} \tag{5.2}$$

and the Laplacian is written:

$$\nabla^2 w = \frac{1}{r} \frac{\partial}{\partial r} \left(r \frac{\partial w}{\partial r} + \frac{1}{r^2} \frac{\partial^2 w}{\partial \theta^2} \right). \tag{5.3}$$

To get the Bilaplacian ∇^4, we simply apply the Laplacian twice $\nabla^4 = \nabla^2\nabla^2$:

$$\begin{aligned}\nabla^4 w = &\frac{1}{r^4}(4\partial_\theta^2 w + \partial_\theta^4 w) + \frac{1}{r^3}(\partial_r w - 2\partial_r\partial_\theta^2 w)\\ &+ \frac{1}{r^2}(2\partial_r^2\partial_\theta^2 w - \partial_r^2 w) + \frac{2\partial_r^3 w}{r} + \partial_r^4 w.\end{aligned} \tag{5.4}$$

Additionally, provided that $R^{-1}|\partial_r w| \ll 1$, $L(w,w)/2$ approximately reduces to the Gaussian curvature of the studied cap $1/R_0^2$. Föppl–Von-Karman equations are valid upon the assumption of mechanical equilibrium, stress tensor and Airy stress function are thus linked by equations:

$$\begin{aligned}\sigma_{rr} &= \frac{1}{r}\frac{\partial\chi}{\partial r} + \frac{1}{r^2}\frac{\partial^2\chi}{\partial\theta^2};\\ \sigma_{r\theta} &= -\frac{\partial}{\partial r}\left(\frac{1}{r}\frac{\partial\chi}{\partial\theta}\right);\\ \sigma_{\theta\theta} &= \frac{\partial^2\chi}{\partial r^2},\end{aligned} \tag{5.5}$$

and planar strain components are computed inverting Hooke's law as:

$$\begin{aligned}u_{rr} &= \frac{1}{Y}(\sigma_{rr} - \nu\sigma_{\theta\theta});\\ u_{\theta\theta} &= \frac{1}{Y}(\sigma_{\theta\theta} - \nu\sigma_{rr});\\ u_{r\theta} &= \frac{1+\nu}{Y}\sigma_{r\theta}.\end{aligned} \tag{5.6}$$

Previous equations are basic tools needed to propose an analytical model for the introduction of our two favourite defects, disclinations and dislocations. In triangular crystalline lattices, such as those formed by viral capsid proteins, positive disclinations are associated with proteins having five neighbors, and negative disclinations with seven neighbors. A dislocation is a bound pair of a positive disclination and of a negative one i. e. an heptamer-pentamer pair.

5.3.2 *Creased membranes and crushed caps*

Before studying directly previous equations with a non-vanishing distribution of defects $s(r,\theta) \neq 0$ on the spherical cap, let us study the initial state of the spherical cap itself. Let us assume an initial sheet is stretched to reach a spherical state of constant Gaussian curvature

$1/R_0^2$. This imposes a deformation $w(r,\theta)$ such that $L(w,w) = 2/R_0^2$. Our sheet is circularly invariant, then w is a pure radial function, hence one can write:

$$\begin{aligned}\frac{1}{2}L(w,w) = \frac{1}{R_0^2} &\Leftrightarrow \frac{d^2w}{dr^2}\frac{1}{r}\frac{dw}{dr} = \frac{1}{R_0^2}\\ &\Leftrightarrow \frac{1}{2r}\frac{d}{dr}\left(\frac{dw}{dr}\right)^2 = \frac{1}{R_0^2} \qquad (5.7)\\ &\Leftrightarrow \frac{dw}{dr} = \sqrt{\frac{r^2}{R_0^2}+\alpha}, \qquad (5.8)\end{aligned}$$

where α is a constant of integration. The slope must vanish at the origin, so $\alpha = 0$, and $d_r w = r/R_0$. It follows subsequently the parabolic profile $w(r) = r^2/2R_0$ that approximates previous constant Gaussian curvature.

Firstly, we compute radial and azimuthal stresses for a spherical cap without any defect. Radial stress-free boundary conditions are imposed, the elastic crystalline sheet is not stretched nor pulled radially. Hoop stress is tensile close to the top and compressive near the rim. This state of stress makes ineluctable the wrinkling of sheets when they are put onto spheres provided their respective sizes are comparable.

With this imposed deformation and with no defects, the compatibility equation is solvable, knowing that χ obeys the same symmetry as the vertical deflection w, and that $\nabla^2 = r^{-1}\,d_r(r\,d_r)$. Hence it is possible to write:

$$\begin{aligned}&\frac{\nabla^4\chi}{Y} = -\frac{1}{R_0^2} \Leftrightarrow \frac{1}{r}\frac{d}{dr}r\frac{d}{dr}\nabla^2\chi = -\frac{Y}{R_0^2}\\ &\frac{1}{r}\,d_r r\,d_r\chi = -\frac{Yr^2}{4R_0^2} + A\log r + B\\ &\chi(r) = -\frac{Yr^4}{64R_0^2} + \frac{Ar^2}{4}(\log r - 1) + \frac{Br^2}{4} + C\log r + D, \qquad (5.9)\end{aligned}$$

where A, B, C and D are, again, constants of integration. As we are only interested in derivatives of χ through Eq. (5.5), D is set equal to zero. It is a dummy constant. Two constants, A and B are directly multiplied by r^2, we choose to re-write χ as:

$$\chi(r) = \frac{-Yr^4}{64R_0^2} + \frac{Ar^2}{4}\log r + \frac{B'r^2}{4} + C\log r, \qquad (5.10)$$

where $B' = B - A$. Now let us reason more physically. We do not want divergent components of the stress tensor at the origin $r \to 0$. Otherwise circular caps mapped onto spheres would not exist, and it should not be possible to wear beanies. Thus, we set $A = C = 0$. Moreover, we want our circular cap to self-asssemble freely, consequently, we impose free-boundary conditions $\sigma_{\theta\theta}(r = R) = \sigma_{r\theta}(r = R) = 0$. The radial

and shear stresses vanish at the boundary. Using Eq. (5.5) again, this enables us to find B:

$$\sigma_{rr}(r = R) = -\frac{YR^4}{16R_0^2} + \frac{B}{2} = 0 \Leftrightarrow B = \frac{YR^2}{8r_0^2}, \tag{5.11}$$

and finally, Airy stress function for a circular cap with constant Gaussian curvature $1/R_0^2$ is written as:

$$\chi(r) = -\frac{Yr^4}{64R_0^2} + \frac{YR^2}{32R_0^2}r^2 = \frac{YR^4}{64R_0^2}\left(2\frac{r^2}{R^2} - \frac{r^4}{R^4}\right). \tag{5.12}$$

The radial and azimuthal stresses become respectively:

$$\begin{aligned} \sigma_{rr} &= \frac{YR^2}{16R_0^2}\left(1 - \frac{r^2}{R^2}\right); \\ \sigma_{\theta\theta} &= \frac{YR^2}{16R_0^2}\left(1 - 3\frac{r^2}{R^2}\right). \end{aligned} \tag{5.13}$$

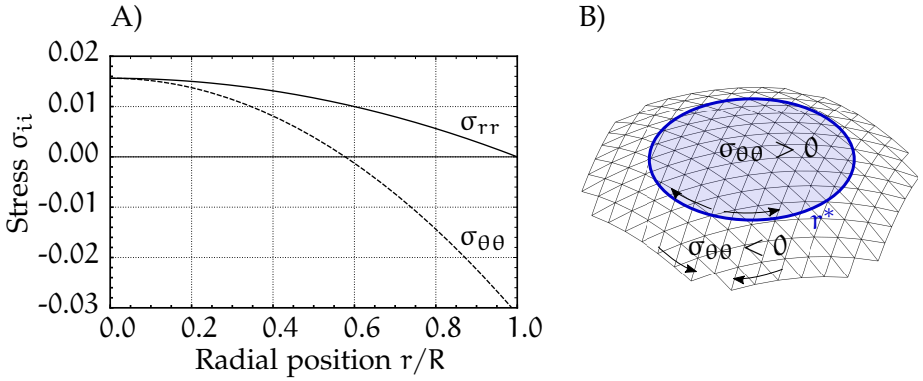

Figure 5.1 – A) Plot of radial and azimuthal stresses (respectively σ_{rr} and $\sigma_{\theta\theta}$) against normalized radial position r/R, where r is the radial position in polar coordinates, R the radius of the cap. For this particular plot, $R/R_0 = 1/2$. R_0 denotes the radius of curvature. Note that above a critical radius $r^* = R/\sqrt{3}$, $\sigma_{\theta\theta}$ becomes negative. B) Sketch of the hoop stress profile where r^* is highlighted in blue.

In Eq. (5.13), one easily finds a critical radius $r^* = R/\sqrt{3}$ above which the hoop stress becomes negative. This signifies that the molecular elastic sheet is tensed close to the center and compressed close to the boundary in the azimuthal direction. This result, in spite of its triviality, permits us to understand why a planar sheet is ineluctably

wrinkled when put onto a sphere. It is the physical consequence of the geometric incompatibility between the plane and the sphere. This state of stress is prone to an out-of plane buckling instability, and it is the origin of the wrinkling observed when a flat disk is forced to adhere on a sphere. A non-negligible amount of papers can be found in literature investigating the latter inevitable wrinkling in spherically confined crystalline sheet [42, 49, 50]. From those papers, we have to underline that wrinkling is possible when the adhesion to the inner core is not too strong compared to the bending cost, allowing an out-of-plane deformation. Also, emergent structures of dislocations presented earlier prevent from the latter crushing (See Ch. 3) [5, 6] and can be used to discuss compression-free model.

5.4 GROWTH ON A SPHERICAL SUBSTRATE

5.4.1 *Introduction of disclinations*

Due to compressive hoop stress at the rim, it is possible to think that pentamers, i.e positive disclinations are nucleated when hoop stress is sufficiently compressive. On the contrary, heptamers, i.e negative disclinations, are nucleated when hoop stress is sufficiently tensile at the rim.

Coming back to our study of self-assembly, and due to previous results, we can anticipate and come up with a spontaneous mechanism for introduction of disclinations. Indeed, one can imagine an open arrangement of five subunits at the perimeter of the crystalline cap. Another unit could perfectly close the latter to get an hexamer. Nevertheless, provided hoop stress is compressive enough, hoop strain can reduce drastically available space for a new subunit addition. Ergo, the nucleation of a pentagon is more likely to happen, resulting into the nucleation of a positively charged 5-fold defect. On the contrary, one can reverse previous argumentation. Provided hoop stress is sufficiently tensile, hoop strain increases available space, rending possible the addition of two supplementary subunits, instead of one, thereby creating a negatively charged 7-fold defect. The mechanism proposed is sketched on Fig. 5.2.

In order to investigate more quantitatively the mechanical influence of defect inclusion in the growing and curved molecular cap, one needs to solve Eq. (5.1) in the presence of an off-centered (positive or negative) disclination. Fortunately for us, the solution has been recently proposed by Grason *et al.* [4, 41], decomposing the effect of defect inclusion into two parts. A direct one, due to the defect itself in an infinite medium, and another one taking into account the interaction between the defect and the boundary. As Eq. (5.1) are linear, the combination of both solutions leads to a global Airy stress

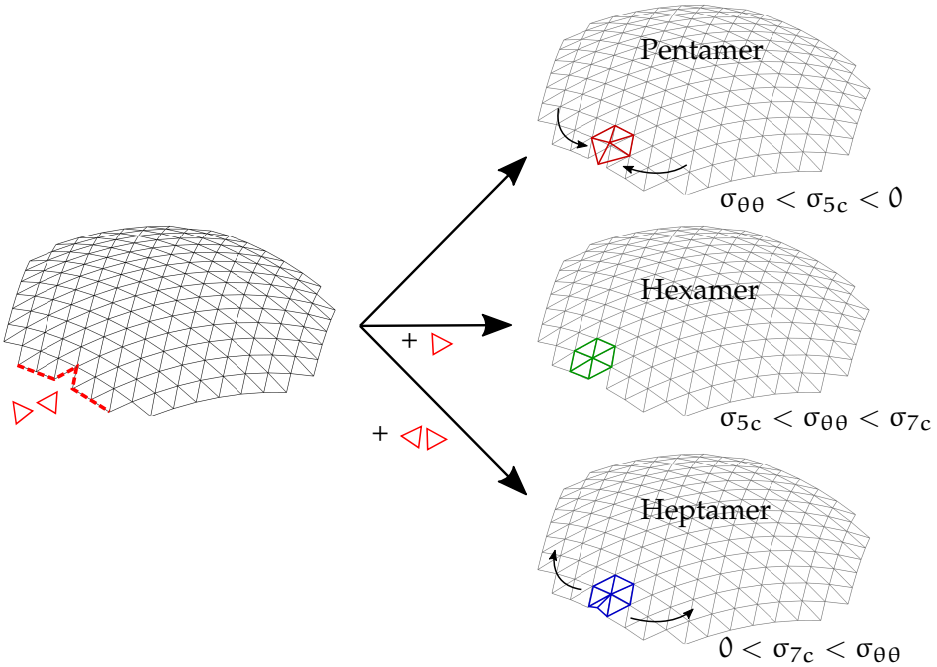

Figure 5.2 – Proposed mechanism for nucleations of defects illustrated on triangulated surfaces, based on values of hoop stress. Threshold values for hoop stress are labeled as σ_{5c} and σ_{7c}. Arrows represent the elastic stress that makes possible the nucleation of the respective (negative or positive) disclination in the azimuthal direction. If hoop stress is compressive enough, a positive disclination is nucleated. On the other hand, if hoop stress is tensile enough, a negative disclination is added. Last mechanism makes possible the introduction of dislocations in the crystalline structure, a supplementing positive 5-fold defect is to be attached to the 7-fold negative one.

function valid for any distribution of defects. This path was originately proposed by Brown in 1941 [19], to study the effect of dislocations on magnetization in a metallic lattice. The interaction between defects and the boundary are computed using an image charge outside the cap, always to satisfy stress-free-boundary conditions. We propose here a simple summary of this work.

It is possible to compute Airy stress function that characterizes states of stress in the crystalline sheet even when an off-centered disclination is included in the studied self-assemble system.

We consider a disclination at polar coordinates $(r = \rho, \theta = 0)$, the direct Airy stress function is given by:

$$\begin{aligned}\chi_d &= \frac{Y_s}{8\pi} r'^2 \log r' \\ &= \frac{Y_s}{16\pi}(r^2 + \rho^2 - 2\rho r\cos\theta)\log[r^2 + \rho^2 - 2\rho r\cos\theta],\end{aligned} \tag{5.14}$$

where $r'^2 = r^2 + \rho^2 - 2\rho r\cos\theta$ represents the squared distance between the point (r, θ) where the function is evaluated and the defect location. In simple words, direct Airy stress function for an off-centered defect is the delocalized direct Airy stress function for a centered defect proposed by Seung *et al.* [94] in a crystalline flexible membrane $\chi_d^S = Y_s/8\pi \cdot r^2 \log r$. χ_d can be expanded:

$$\chi_d = \begin{cases} \dfrac{Y_s r'^2}{8\pi}\left[\log\rho - \displaystyle\sum_{n=1}^{\infty}\frac{1}{n}\left(\frac{r^n}{\rho^n}\right)\cos n\theta\right] & \text{if } r < \rho; \\ \dfrac{Y_s r'^2}{8\pi}\left[\log r - \displaystyle\sum_{n=1}^{\infty}\frac{1}{n}\left(\frac{\rho^n}{r^n}\right)\cos n\theta\right] & \text{otherwise.}\end{cases} \tag{5.15}$$

In order to compute indirect Airy function, we seek solution of $\nabla^4\chi_i = 0$ for $r < R$ using Michell solution of generic form:

$$\chi_i = \sum_{n=0}^{\infty} C_n r^n \cos n\theta + D_n r^{n+2}\cos n\theta, \tag{5.16}$$

where C_n and D_n coefficients are determined in order to satisfy stress-free boundary condition [71].

In order to find latter coefficients, we re-write the multipole expansion given in Eq. (5.15) for the direct stress function corrected from Ref. [41]:

$$\chi_d = \begin{cases} \dfrac{Y_s}{8\pi}\displaystyle\sum_{n=0}^{\infty} A_n^{<}(r)\cos n\theta & \text{if } r < \rho; \\ \dfrac{Y_s}{8\pi}\displaystyle\sum_{n=0}^{\infty} A_n^{>}(r)\cos n\theta & \text{if } r > \rho,\end{cases} \tag{5.17}$$

where we give the coefficients that depend on the position at which the function is evaluated:

$$\begin{cases} A_0^<(r) = (\rho^2 + r^2)\log\rho + r^2 \\ A_1^<(r) = -2\rho r\log\rho - r\rho - \dfrac{r^3}{2\rho} \\ A_{n\geqslant 2}^<(r) = \dfrac{r^n}{\rho^n}\left[\dfrac{\rho^2}{n(n-1)} - \dfrac{r^2}{n(n+1)}\right], \end{cases} \tag{5.18}$$

and:

$$\begin{cases} A_0^>(r) = (\rho^2 + r^2)\log r + \rho^2 \\ A_1^>(r) = -2\rho r\log r - r\rho - \dfrac{\rho^3}{2r} \\ A_{n\geqslant 2}^>(r) = \dfrac{\rho^n}{r^n}\left[\dfrac{r^2}{n(n-1)} - \dfrac{\rho^2}{n(n+1)}\right]. \end{cases} \tag{5.19}$$

Now, it suffices to inject $\chi = \chi_d + \chi_i$ in Eq. (5.5), and to reduce both boundary conditions at $r = R$ to get a system of equations that will enable us to get a final formulation for C_n and D_n respectively. From first condition:

$$\sigma_{r\theta}|_{r=R} = 0 \Leftrightarrow \partial_r\frac{1}{r}\partial_\theta(\chi_i + \chi_d)|_{r=R} = 0, \tag{5.20}$$

one writes the relation $\forall n \in \mathbb{N}$:

$$C_n(n-1)R^{n-2} + D_n(n+1)R^n + \frac{d_r A_n(r)|_{r=R}}{R} - \frac{A_n(R)}{R^2} = 0, \tag{5.21}$$

and from second condition:

$$\sigma_{rr}|_{r=R} = 0 \Leftrightarrow \frac{1}{r^2}\partial_\theta^2(\chi_i + \chi_d) + \frac{1}{r}\partial_r(\chi_i + \chi_d)|_{r=R} = 0, \tag{5.22}$$

we writes $\forall n \in \mathbb{N}$:

$$(-n^2 + n)C_n R^{n-2} + (-n^2 + n + 2)D_n R^n - n^2\frac{A_n(R)}{R^2} + \frac{d_r A_n(r)|_{r=R}}{R} = 0. \tag{5.23}$$

Note that we got rid off the $<,>$ superscripts, as computations are rigorously the same in both cases. Now solving the system of equations composed of Eq. (5.21) and Eq. (5.23), we get the solutions:

$$\forall n \in \mathbb{N}, \begin{cases} C_n = \dfrac{1}{2R^n}[R\, d_r A_n(r)|_{r=R} - (n+2)A_n(R)] \\ D_n = \dfrac{1}{2R^{n+2}}[nA_n(R) - R\, d_r A_n(r)|_{r=R}] \end{cases} \tag{5.24}$$

From now on, we will focus on azimuthal stress at the boundary. Combining Eq. (5.19) and Eq. (5.24), it is possible to compute $\chi_i^{r>\rho}(r)$ that is to add to χ_d to get full Airy stress function in the presence of an off-centered defect at $\{\rho, 0\}$ for a flat surface. To complete Ref. [41]:

Radial and hoop stresses can be computed from previous Airy stress function.

$$\frac{\chi_1^{r>\rho}}{Ys/8\pi} = \frac{r'^2}{2}\log\left(\frac{r'^2R^4}{\bar{r}'^2\rho^2}\right) - \frac{r(2\rho^3\cos\theta + r(R^2-\rho^2+R^2\log R^2))}{2R^2}. \tag{5.25}$$

Here, we call $\bar{r}'^2 = r^2 + R^4/\rho - 2rR^2\cos\theta/\rho$ the distance between the point of observation and the image charge outside the boundary at $(R^2/\rho, 0)$. We recall that the image charge was created to get stress-free boundary conditions in radial directions at the rim of the spherical crystalline cap. To get the angular dependence with the defect location in the latter function, it suffices to replace θ by $\theta - \phi$, where ϕ denotes its angular position. A last single step is necessary to get physical quantities, the computation of stress tensor components using Eq. (5.5) for a disclination (we recall that the assumed position is $\{\rho, \theta = 0\}$ on the sheet). We write:

Positive disclinations (pentamers) relax compressive hoop stress when they nucleate at the rim of the spherical crystalline sheet. This relaxation is short-ranged. If a first disclination is nucleated at the rim, hoop stress is still highly compressive at diametrically opposed points. This favors face to face disclination nucleations.

$$\begin{aligned}\frac{\sigma_{\theta\theta,1}^{r>\rho}}{Ys/8\pi} &= -1 + \frac{\rho^2}{R^2} + \log\left(\frac{r'^2R^2}{\bar{r}'^2\rho^2}\right) \\ &+ \frac{3r^2+\rho^2+2\rho\cos\theta(\rho\cos\theta - 3r)}{r'^2} \\ &- \frac{\bar{r}'^2\rho^3[5r^2\rho+\rho^3-2r\cos\theta(2R^2+3\rho^2)+4R^2\rho\cos^2\theta]}{\bar{r}'^4\rho^4} \\ &- \frac{2\rho^2r'^2(r\rho - R^2\cos\theta)^2}{\bar{r}'^4\rho^4},\end{aligned} \tag{5.26}$$

$$\begin{aligned}\frac{\sigma_{rr,1}^{r>\rho}}{Ys/8\pi} &= \frac{\rho^2}{R^2} + \log\left(\frac{r'^2R^2}{\bar{r}'^2\rho^2}\right) + \frac{2\rho^2\sin^2\theta}{r'^2} \\ &- \frac{2R^6 + r^2\rho^2(r^2+4R^2) + r^2\rho^4}{\bar{r}'^4\rho^2} \\ &+ \frac{r\rho\cos\theta[3R^4+2R^2\rho^2+2r^2(R^2+\rho^2)]}{\bar{r}'^4\rho^2} \\ &- \frac{R^4[\cos 2\theta(r^2-2R^2+\rho^2)+r\rho\cos 3\theta]}{\bar{r}'^4\rho^2}.\end{aligned} \tag{5.27}$$

Using these exact expressions and due to the linearity of Eq. (5.1) and of Eq. (5.5), it is possible to investigate the relaxation of hoop stress at

the rim of the circular curved cap for various defect configurations, provided we specify their positions. Indeed, for a self-assembly assumed irreversible, the modulation of hoop stress by inclusion of defects at the rim of the scaffold is the only degree of freedom and thus the only way to relax its elastic stress. For this reason we evaluate resulting hoop stress at $r = R$ in function of θ. For a single disclination of charge s located at $\{\rho_1, \theta_1\}$, resulting hoop stress is (taking into account the curvature with the first term, the second represents the stress generated by the defect itself):

$$\sigma_{\theta\theta,1}(R,\theta) = \frac{YR^2}{16R_0^2}\left(1 - 3\frac{r^2}{R^2}\right) + \frac{Ys}{8\pi}\frac{2(R^2-\rho_1^2)^2}{R^2[R^2+\rho_1^2-2R\rho_1\cos(\theta-\theta_1)]}. \quad (5.28)$$

However, nucleation of positive disclinations at the rim generates tensile bursts in the azimuthal direction between the boundary and the defects. This promotes nucleation of negative disclinations (heptamers) to create dislocations. On the contrary, bursts are compressive if negative dislocations are nucleated. This enables also to create dislocations, reversing latter reasoning.

On Fig. 5.3, the inclusion of a single positive defect, relieves the hoop stress locally. The effect apears to be quite large close to the defect itself, where hoop stress becomes positive, hence tensile. However, $\sigma_{\theta\theta}$ reduces significally towards the initial compression due to curvature at diametrically opposed points. According to our initial intuition, during the growing process, another positive disclination is more prone to nucleate at the opposite of the initial one on the cap. After the second nucleation, once again, the most compressive regions are located symmetrically *between* the two first disclinations. Increasing the size of the surface, we observe that inclusion of disclinations at highly compressive regions relaxes them significantly. Iterating this mechanism for disclination inclusion and this type of minimal hoop stress analysis, it shall be possible to recover azimuthal locations compatible with icosahedral symmetry for large spherical viruses. However, radial locations for optimal defect inclusion may depend on further details of the model, one can think about the contact energy between capsomers.

If we consider now azimuthal stress in function of r denoting the radial position, at the angular position of a single fivefold defect, we notice that the latter inclusion induces a burst of tensile hoop stress between the defect and the rim itself. According to our earlier analysis (See Fig. 5.2), the burst shall promote the nucleation of a sevenfold negative defect. On the other hand, if hoop stress is plotted against r, but now at the angular position of a sevenfold defect, we notice the negative disclination induces a burst of compressive hoop stress. Therefore, it favors the nucleation of a fivefold positive defect. By this quantitative analysis, we consolidate previously assumed mechanism

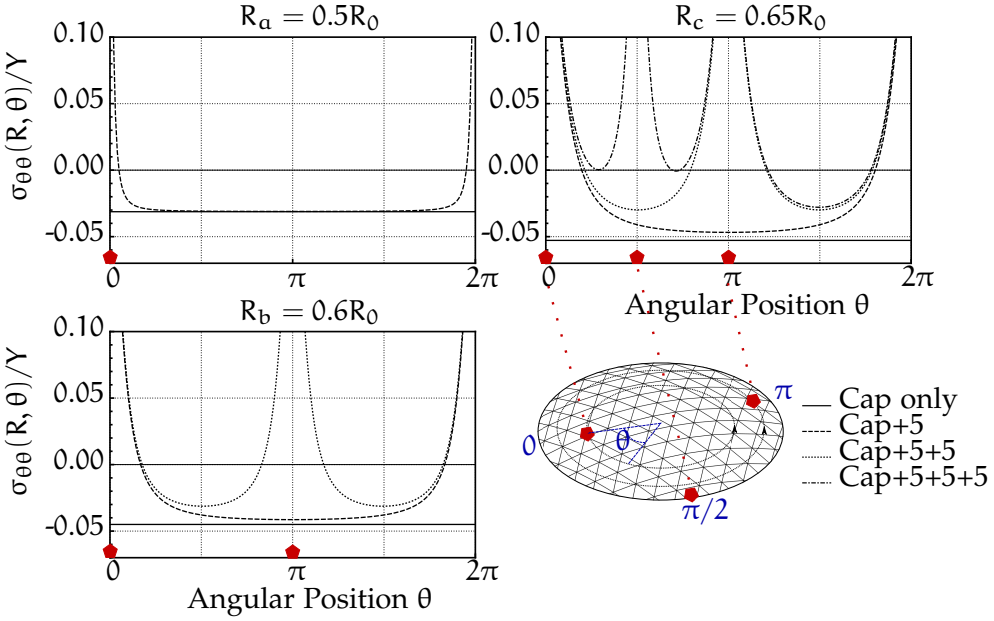

Figure 5.3 – Relaxation of hoop stress by defect nucleation. The hoop stress at the rim of the assembly is computed with and without defects (highlighted in red on the sketched structure, we specify their angular positions on graphs). The size R of the structure is shown at the top of each graph in function of imposed Gaussian curvature radius R_0. The radial position of the first defect $\rho_1 = 0.95R_a$, the second defect $\rho_2 = 0.8R_b$, the third one $\rho_3 = 0.85R_c$. We chose radial positions in order to highlight relaxation of hoop stress described in the main text. At each step, a disclination is added at the most compressive region.

for defect nucleation whatever their types: disclinations or dislocations. Based on this observation, one dislocation or several ones may also be efficient in relieving hoop stress at the boundary (See Fig. 5.4).

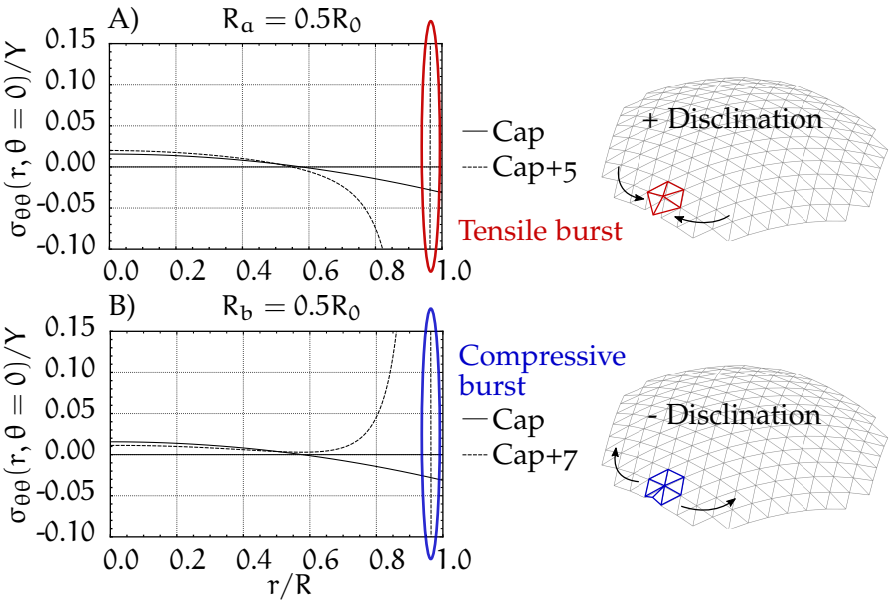

Figure 5.4 – Hoop stress $\sigma_{\theta\theta}$ in function of the adimensionalized radial position r/R, R represents the size of the cap specified at the top of each graph in function of the imposed radius of curvature R_0. A) Only one positive disclination is included in the structure (a 5-fold defect). In the configuration specified in Fig. 5.3. We plot hoop stress for $\theta = 0$ i. e. the angular position of the first defect. Note the tensile burst near the border of the cap, this should favor the inclusion of a negative 7-fold defect. B) On the contrary, the negative disclination case is considered, though with same configuration. Now, a compressive burst near the border of the cap favors the nucleation of a 5-fold defect. Note the subsequent relief of hoop stress each time a disclination is added.

5.4.2 *Introduction of dislocations*

To study the effect of dislocations on azimuthal stress at the rim of the cap, we compute Airy stress function in the presence of a single off-centered dislocation. This can be done by superimposing Airy stress function of a 5-fold and a 7-fold defect in the limit of vanishing separation. Within the continuous limit, we recall that this

pair of defects can be viewed as a dislocation. Assuming the resulting dislocation possesses a Burgers vector $\mathbf{b} = b\mathbf{e}_\theta$, we compute χ_{57} as:

$$\chi_{57}(r,\theta) = b \lim_{e\to 0} \frac{\chi_1^{(\rho,\theta)}(r,\theta) - \chi_1^{(\rho+e,\theta)}(r,\theta)}{e}. \tag{5.29}$$

It is also possible to compute Airy stress function when an off-centered dislocation is included in the studied self-assembled system. It suffices to consider the contribution of a pair of opposed disclinations in the vanishing separation limit.

Hence:

$$\begin{aligned}\frac{\chi_{57}^{r>\rho}(r,\theta)}{Yb/12} &= -\frac{r^2R^2 + R^4 + r^4(\rho^2/R^2 - 1)}{\rho\bar{r}'^2} \\ &- \frac{r\cos\theta[-R^2(R^2+4\rho^2) + r^2(R^2 - \rho^2 - 3\rho^4/R^2) + 6r\rho^3\cos\theta]}{\rho^2\bar{r}'^2} \\ &- (\rho - r\cos\theta)\log\left(\frac{R^4 r'^2}{\rho^2\bar{r}'^2}\right),\end{aligned} \tag{5.30}$$

and it becomes relatively "easy" to compute radial and hoop stresses using Eq. (5.5). The results are presented on Eq. (5.31) and Eq. (5.32). We compute first σ_{rr}:

$$\begin{aligned}\frac{\sigma_{rr}^{57,r>\rho}}{Yb/12} &= -\frac{2\rho}{R^2} - \frac{2(\rho - r\cos\theta)}{r'^2} + \frac{2r(r\rho - R^2\cos\theta)}{\rho^2\bar{r}'^2} \\ &+ \frac{\rho^2(2r^2\rho(r^2+4R^2+2\rho^2) - r(2r^2R^2 + 3R^4 + 6(r^2+R^2)\rho^2)\cos\theta)}{\rho^4\bar{r}'^4} \\ &+ \frac{\rho^2R^4(2\rho\cos 2\theta + r\cos 3\theta)}{\rho^4\bar{r}'^4} - \frac{4r\rho(r - \rho\cos\theta)\sin^2\theta}{r'^4} \\ &- \frac{2\rho(-R^4 + r^2\rho^2)}{\rho^6\bar{r}'^6}\left\{2R^6 + r^2(r^2+4R^2)\rho^2 + r^2\rho^4\right. \\ &-r\rho[3R^4 + 2R^2\rho^2 + 2r^2(R^2+\rho^2)]\cos\theta \\ &\left.+R^4[(r^2 - 2R^2 + \rho^2)\cos 2\theta + r\rho\cos 3\theta]\right\}.\end{aligned} \tag{5.31}$$

We specify here that, for such a dislocation, the 5-fold defect is closer to the center of the disk, whereas, the 7-fold is closer to the border. Consequently, the two defects are aligned radially.

If one wishes the opposite configuration, it suffices to change the sign of both equations. We present $\sigma_{\theta\theta}$:

$$\begin{aligned}\frac{\sigma_{\theta\theta}^{57,r>\rho}}{Yb/12} &= -\frac{2\rho}{R^2} - \frac{2(\rho - r\cos\theta)}{r'^2} - \frac{2r\rho^2(r\rho - R^2\cos\theta)r'^2}{\rho^4\bar{r}'^4} \\ &+ \frac{2r(r\rho - R^2\cos\theta)}{\rho^2\bar{r}'^2} + \frac{2\rho(r^2 + 2\rho^2 - 3r\rho\cos\theta)}{\rho^2\bar{r}'^2} \\ &+ \frac{8r^2R^4\rho + 8R^2\rho(R^4 + 2r^2\rho^2)\cos^2\theta - 4r\cos\theta(R^6 + R^2(r^2 + 4R^2)\rho^2)}{\rho^4\bar{r}'^4} \\ &- \frac{4r\cos\theta(r^2\rho^4 + R^4\rho^2\cos 2\theta)}{\rho^4\bar{r}'^4} + \frac{4r\rho(r - \rho\cos\theta)\sin^2\theta}{r'^4} \\ &- \frac{2\rho}{\rho^6\bar{r}'^6}\left\{-4r\rho(r\rho - R^2\cos\theta)^3(r^2 + \rho^2 - 2r\rho\cos\theta)\right. \\ &+ (R^4 + r^2\rho^2 - 2rR^2\rho\cos\theta)[2\rho(\rho - r\cos\theta)(r\rho - R^2\cos\theta)^2 \\ &\left. + (r^2 + \rho^2 - 2r\rho\cos\theta)(R^4 + 4r^2\rho^2 - 6rR^2\rho\cos\theta + R^4\cos 2\theta)]\right\}. \end{aligned} \tag{5.32}$$

Again, it suffices to superimpose, for an arbitrary distribution of dislocations (radially aligned though), latter Airy stress function to get final global Airy function injecting angular and radial dependence as for distributions of disclinations. Only angular dependence of dislocations themselves is not taken into account in those formulae. Additionally, it is perfectly possible now to create and analyze the effect of distributions of both disclinations *and* dislocations, for example combination of scars and disclinations at the rim of the hexatic sheet. As for a disclination, we give the hoop stress at the rim for a single dislocation located at $\{r = \rho_1, \theta = \theta_1\}$ (again we take into account the curvature, the second term is the defect contribution):

$$\begin{aligned}\sigma_{\theta\theta,1}^{d}(R,\theta) &= \frac{YR^2}{16R_0^2}\left(1 - 3\frac{r^2}{R^2}\right) \\ &+ \frac{Yb}{24}\frac{4(R^2 - \rho_1^2)[\rho_1(3R^2 + \rho_1^2) - R(R^2 + 3\rho_1^2)\cos(\theta - \theta_1)]}{R^2[R^2 + \rho_1^2 - 2R\rho_1\cos(\theta - \theta_1)]^2}. \end{aligned} \tag{5.33}$$

In Fig. 5.5, we show different hoop stress distributions at the rim for several defect arrangements. Obviously, single disclination case and single dislocation case are compared, but we analyze also both effects of a small grain boundary (three dislocations aligned on a row) and of a "charged" grain boundary (three aligned dislocations which row is terminated by a disclination). It is evident to notice that, whatever the type of defect studied, hoop stress close to a defect is relieved, but it

reduces drastically when the position diametrically opposed is reached. In addition, for a given small size of the disc (compared to the radius of curvature), no significant differences can be noticed between patterns of hoop stress distributions with respect to defect types. However, if the latter size is increased, long range stress relaxation varies with respect to defect configurations. Indeed, we observe that charged grain boundaries are best for long range stress relief while the crystalline cap grows. This observation is compatible with the presence of grain boundaries in the ground state energy of closed shells with large radii previously mentioned earlier [6, 12, 16].

Similarly, hoop and radial stresses generated with a dislocation can be computed. Relaxation stress patterns are very similar to those realized with disclinations. However, elastic stress contributions of dislocations and disclinations can be summed up to analyze the effect of chains of dislocations or disclinations, i.e, scars.

It could be of interest to test, using the superimposition property of previous equations, hoop stress relaxation at the rim for various defect distributions. More especially, to test the effect of length for scars and against various directions.

5.5 VARIOUS DISTRIBUTIONS

5.5.1 *Defects along one direction VS multiple directions*

Previous patterns are invariant if other directions are added in defect distributions. They are invariant with respect to angular orientations.

In this section, we compute hoop stress at the rim of the spherical crystalline cap for several defect configurations. More specifically, for each type of defect arrangement (isolated disclination, isolated dislocation, scars) we wish to test the relaxation pattern against its orientation. In other words, is there a benefit to include several similar defects at the same radius but for various angular positions ? As said, previously, it suffices to sum up hoop stresses for all defects switching appropriately angular and radial dependences. On Fig. 5.6, we make the quantitative comparison. As noticed previously, even in the multidirectional case, latter order of curves is conserved, i. e. grain boundaries are best to relax hoop stress at the rim at long distances. However, the stress relaxation pattern is enhanced adding multiple directions to the defect distribution. This is not surprising considering the fact that more defects help to screen the elastic stress, improving then the relaxation. Note that, if one is to understand special features of stress relaxation by defect nucleation, testing hypotheses against one direction is easier and results extracted are also relevant in multiple directions (See Fig. 5.6).

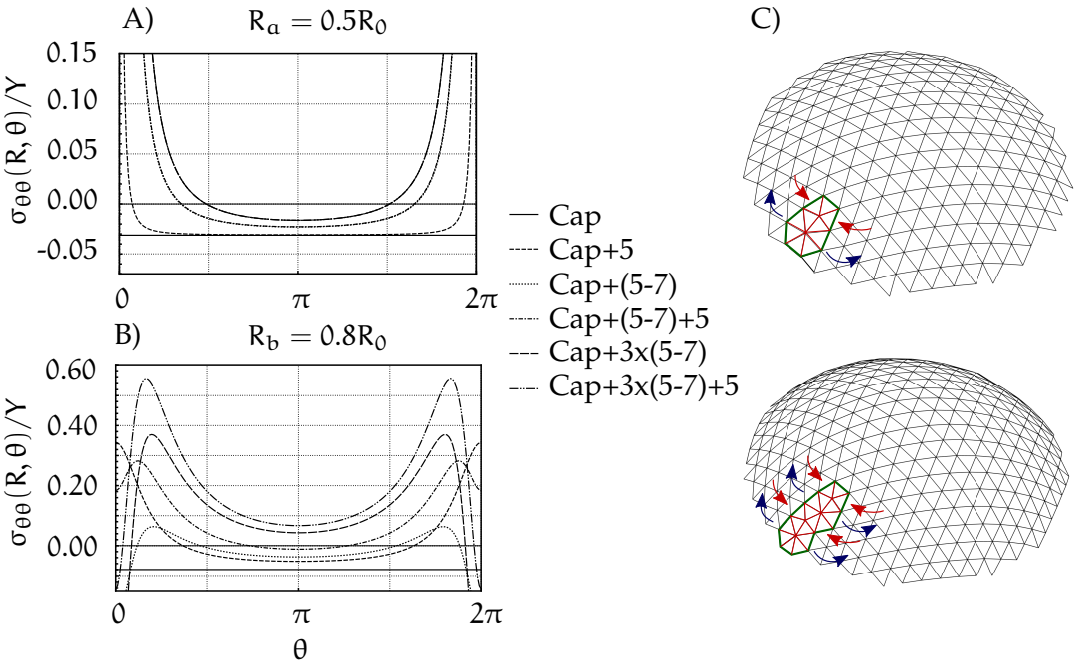

Figure 5.5 – Hoop stress with respect to polar angle for various defect distributions. Those configurations are used to relax locally the mechanical stress due to the geometric curvature, we set Gaussian curvature to $1/R_0^2$. The size of the cap is shown at the top for each graph. A) All defects are arranged along the single angular position $\theta = 0$. Their radial positions are as follows, $\rho_5 = \rho_{57} = .95R_a$, for the charged dislocation $\rho_{57} = .95R_a$; $\rho_5 = .97R_a$. For the scar, $\rho_{57}^{(1)} = .95R_a$, $\rho_{57}^{(2)} = .97R_a$, $\rho_{57}^{(3)} = .99R_a$. For the charged scar, we chose a similar arrangement, and we set $\rho_5 = .996R_a$. For distributions close to the border, no particular effect is observed on stress relaxation patterns at long distance. B) However, for the very same arrangement, and if the size of the cap is increased, a strong modulation of the relaxing effect is possible, where the charged scar appears to be more efficient. C) We sketch here typical configurations at the rim of triangulated surfaces: a single dislocation and a scar made of two dislocations, hoop stress patterns are highlighted with red and blue arrows (respectively red for a compressive stress and blue for a tensile one).

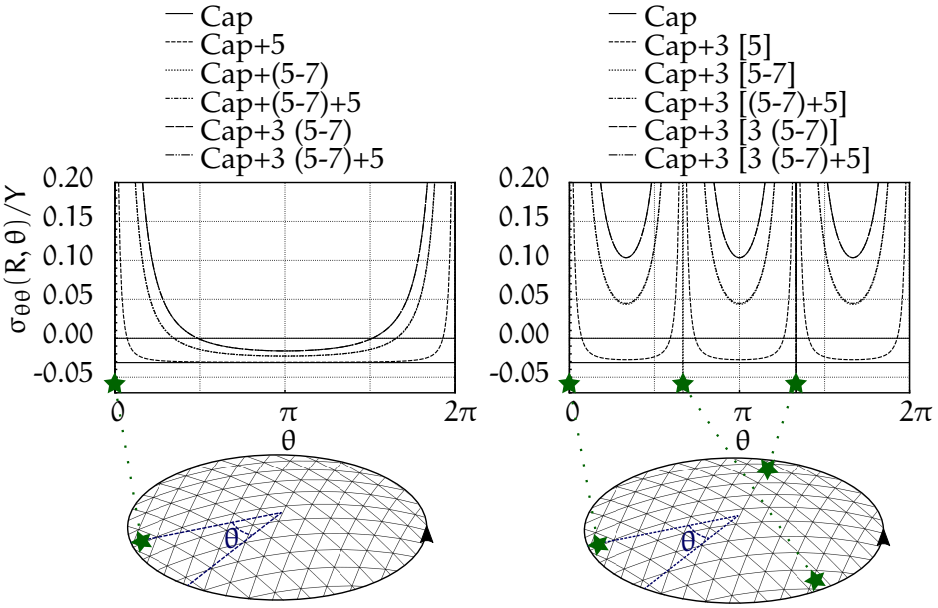

Figure 5.6 – Hoop stress relaxation against the angular position at the rim of the cap for several defect distributions. We highlight here that for similar defect arrangements, the "relaxation order" is conserved, i. e. no change in relaxation efficiency can be observed comparing respectively disclinations, dislocations, charged dislocations, etc., if same types of defect(s) are added at other angles. For instance, on graph A) defects are placed at $\theta = 0$, and then B) disposed at respectively $\theta_i = \{0, 2\pi/3, 4\pi/3\}$. Locations of defects are sketched by green stars on respective spherical caps below each graph. In fact, each defect nearly touches the boundary. The order remains unchanged. Nevertheless, a better mechanical relaxation can be noted due to the higher number of defects in the second case.

5.5.2 *Effect of scar lengths*

Because we know now that testing special configurations in one direction is as relevant as in several ones, we wish to evaluate the effect of scar length on stress relaxation. Does a long scar have a better effect than a smaller one on $\sigma_{\theta\theta}$ at the rim of the molecular assembly ? To adress this question, we build scars made of three, five, ten and fifteen dislocations aligned radially for a unique angular position θ. Results are shown on Fig. 5.7. Increasing the length of scars leads undoubtedly to better relaxations. This can be easily deduced from the vertical shift of hoop stress towards positive values (tensile hoop stress). Additionally, a scar starting in the bulk of the molecular assembly and terminating at the boundary induces a better relaxation (See Fig. 5.7).

Better long-range hoop stress relaxations are obtained with long scars terminated by isolated disclinations in the crystalline spherical cap.

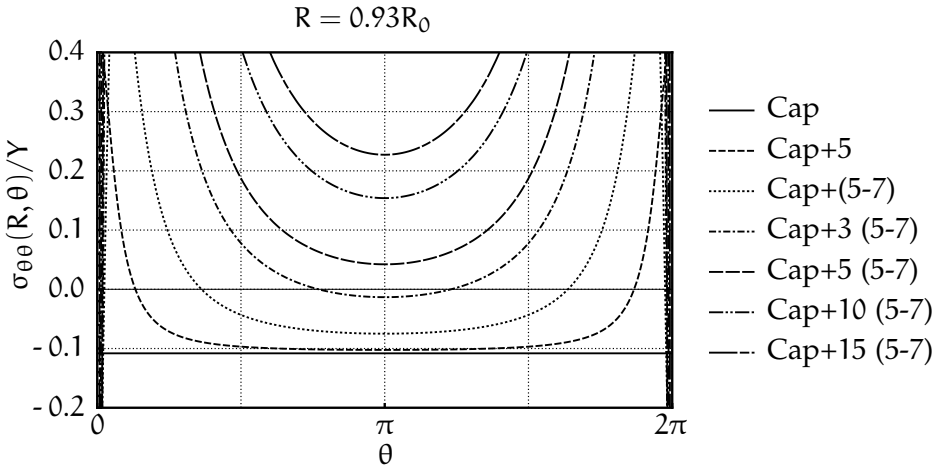

Figure 5.7 – Hoop stress relaxation against the angular position at the rim of the cap for various length of scars. Defects are radially aligned along a single direction. We set $\rho_1 = .758R$, for the single disclination and single dislocation. Then, between each defect, we let a space of .008. Note that the best relaxation is obviously obtained for the longest scar. Hoop stress relaxation pattern remains unchanged though.

All previous results were derived and tested analytically, we should now test them numerically, using the triangular model proposed by Seung and Nelson [94] and presented earlier.

6 NUMERICAL TEST

6.1 RÉSUMÉ

Dans ce chapitre, le précédent modèle de nucléation de défauts topologiques (heptamères et pentamères) est étudié numériquement. Un accord raisonnable qualitatif et quantitatif est obtenu avec les précédents résultats analytiques.

6.2 INTRODUCTION

It is possible to test latter predictions of the elastic analytical model by using numerical triangular surfaces. We will first recall proceedings and then present numerical results compared with the analytical model.

6.3 NUMERICAL PROCEEDINGS AND TEST

A numerical test of the previously proposed mechanism can be realized. A satisfactory agreement between analytical and numerical results is firstly reached.

To check our model numerically, the triangular coarse-grained protein lattice is computed to match the topological properties of the protein surface. Consequently, most vertex are shared among six triangles, five triangles for a positive disclination, 7 for a negative one, dislocations are created by 5-7 dipoles. The elastic energy is composed of two terms: an in-plane stretching energy and an out-of-plane bending energy, both terms are to be minimized to obtain equilibrium configurations. We write the total energy:

$$E = \frac{k_e}{2} \sum_{\alpha,\beta} (d_{\alpha,\beta} - d_0)^2 + k_b \sum_{i,j} [1 - \cos(\theta_{i,j} - \theta_0)], \tag{6.1}$$

where $d_{\alpha,\beta}$ is the length of the edge connecting vertices α and β, the preferred length being d_0. $\theta_{i,j}$ represents the angle between the two normal vectors of adjacent triangles i and j. The remaining set of parameters $\{k_e, k_b, \theta_0\}$ enables us to model intrinsinc elastic properties between building blocks. More precisely, θ_0 models the preferred curvature between adjacent faces to mimic the radius of curvature R_0 such that $\theta_0 \sim d_0/R_0$. Within the continuous limit, the discrete model

reproduces the continuous system with elastic constants $Y = 2k_e/\sqrt{3}$, $D = \sqrt{3}k_b/2$, with equal Lamé coefficients $\lambda = \mu = \sqrt{3}/4 \cdot k_s$ and with the Poisson ratio $\sigma = 1/3$.

In order to compare and test our analytical predictions, the triangular structure with appropriate defect locations is constructed. Then, we map each vertices on the surface of a sphere with radius R_0, the final structure is relaxed using the conjugate gradient method [80]. To prevent the latter structure to recover a particular flat state, we add a radial Morse potential between vertices and the spherical "substrate". For following numerical results, we ensured that the pure elastic energy does not depend on the Morse parameters.

The numerical computation of stress tensor components is rather tedious as it requires to perturb numerical membranes. Hence, if one wishes to compare numerical and analytical hoop stress patterns at the rim, it is easier to evaluate the stretching energy density Γ. Indeed, because of specific radial stress-free boundary conditions, Γ is evaluated as:

$$\Gamma(R,\theta) = \frac{[\sigma_{rr}(R,\theta) + \sigma_{\theta\theta}(R,\theta)]^2}{2} = \frac{\sigma^2_{\theta\theta}(R,\theta)}{2}. \tag{6.2}$$

Consequently, in the numerical case, we evaluate Γ by averaging for each vertex of the rim the stretching energy stored in the related connected edges.

The proposed mechanism is finally tested numerically. Numerical trends are in agreement with what has been written previously. Negative disclinations and dislocations appear if tensile stress threshold is low. If the latter is high, only positive disclinations nucleate.

We test numerically three particular configurations. A first one with a disclination close to the boundary and a second one with the same positive charge far from the boundary. The last configuration possess three disclinations close to the rim, in order to test the stress relief when several defects are included in the coarse-grained molecular structure. Quantitative comparisons are shown in Fig. 6.1. For all cases, comparison between numerical and analytical energy densities shows satisfactory agreement. Remarkably, no adjustment has been required on numerical parameters to get latter agreements. Note that, for the multidisclination case, the reversal of the convexity of $\sigma^2_{\theta\theta}$ due to negative squared values is not present. This implies the stress-relief towards positive values by defect nucleations. Overall, those comparisons validate analytical results obtained in this work. Quantitative comparisons were also realized for isolated dislocations close and far from the rim of the coarse-grained molecular scaffold. Again, satisfactory agreements are obtained without any adjustment validating, once again, our previous results.

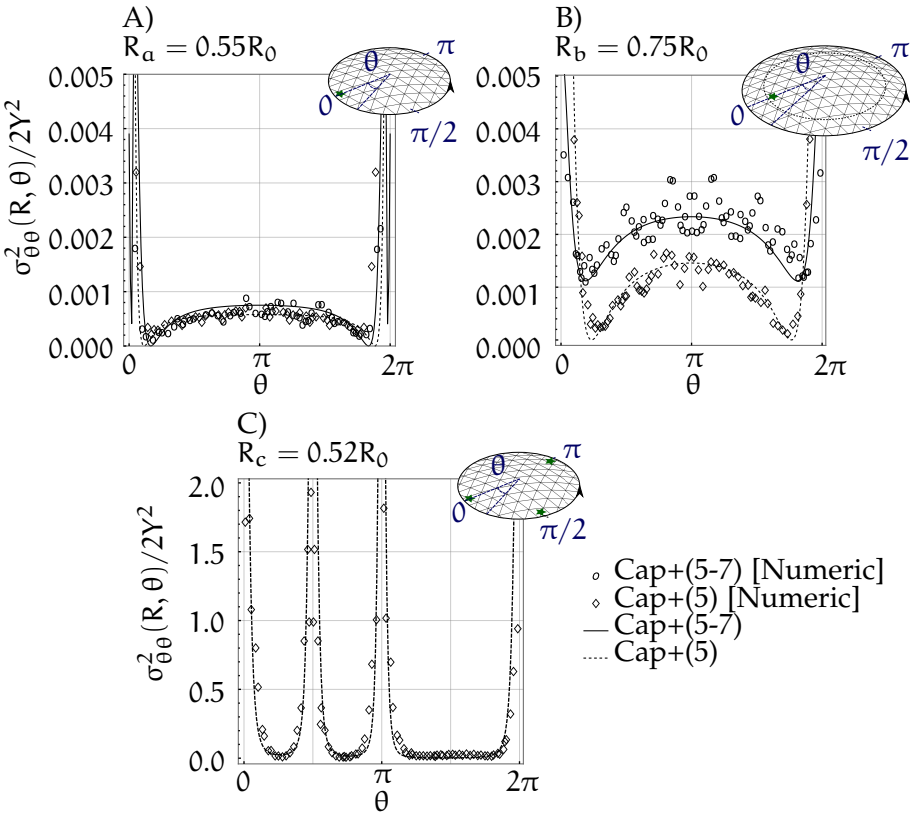

Figure 6.1 – Comparison of analytical (lines) and numerical (points) energy densities at the rim of the coarse-grained crystalline cap for several defect distributions. Numerical structures were built accordingly. We present here the single disclination case and the single dislocation one A) at the rim and B) far from the border. C) The multidisclination case is shown below. The size of the spherical cap for each plot is shown above in function of the radius of curvature R_0. Other parameters, $\rho_5 = \rho_{57} = .88R_a$, and $\rho_5^{(3)} = .88R_c$. $\theta = 0$ for two first cases, $\theta_i = \{0, \pi/2, \pi\}$ for the last one. Locations of defects are sketched with green stars on respective spherical caps at top right corners. Satisfactory agreements are obtained for all cases without any adjustment.

6.4 SWITCHING FROM DISCLINATIONS TO DISLOCATIONS

In this section, we present additionnal results of self-assembly simulations. The algorithm used here is very similar to the one elaborated by Li *et. al* [64, 106, 112]. We recall here its main features, and our modifications. As said previously, the building blocks are deformable triangles that self-assemble by sharing edges. The resulting structure grows on an attractive spherical substrate to model inner core attraction. The Morse potential is once again used. We choose to build triangular structures isotropically, and at each growing step of the simulation, elastic energy is minimized using the conjugate gradient algorithm. We ensure that the adhesive Morse energy to reach specific Gaussian curvature is not taken into account in the minimisation process. Each time five triangles meet at a common vertice, there is a choice to be made: closing the pentagon or adding a new triangle to form an hexagon. The choice can be made on an energetic criterion, selecting the configuration with the lowest energy. Equivalently, it suffices to compare the length between the two free vertices of the unclosed pentagon. If the length is smaller than a given threshold l_{5c}, the local structure is closed. On the contrary, if the length is larger, a new block is added to form an hexagon.

In our algorithm, we slightly modify this last step. Indeed, we suggested previously that depending on hoop stress values, the local structure is to be closed into a pentagon or an heptagon. If $\sigma_{\theta\theta}$ is smaller (respectively larger) than a critical threshold σ_{5c} (respectively σ_{7c}), we proceed to the nucleation of a pentagon (respectively of an heptagon). Now, using classical Hook relation, we can translate two stress thresholds into strain thresholds: $u_{5c} = \sigma_{5c}/Y$, $u_{7c} = \sigma_{7c}/Y$. Finally, those two strain thresholds can be translated numerically into length thresholds, with relations $u_{5c} = (l_{5c} - l_0)/l_0$, $u_{7c} = (l_{7c} - l_0)/l_0$ respectively.

As a consequence, when the length between free boundary vertices is smaller than l_{5c}, we close the pentagon, when it is between l_5c and l_7c, we close an hexagon (i. e. one triangle is added), when it is above l_{7c}, we close an heptagon (i. e. two triangles are added). We show in Fig. 6.2, numerical structures that result from such an algorithm. We start from an initial coarse-grained triangular lattice free from topological charge. Then, varying the parameter l_{7c}, we add exactly 180 triangles without any other restriction regarding their distribution. It is observed that reducing l_{7c} promotes the transition

from disclination mode stress relaxation to dislocation and scar mode stress relaxations. At this point, we can take a step back, and consider our results. Indeed, the resulting scars are not aligned radially (which is the most effective way of relaxing for a frozen structure according to the literature [5, 6]). They are rather aligned with the boundary. Such a distribution of scars may be due to our irreversible assumption. We assumed the structure cannot re-organize at the boundary to prevent from the nucleation of heptamers. Even though such a nucleation is locally favorable, it may be forbidden from a global view point or re-arranged radially. This is how we can rationalize and interpret our typical scar distributions. Then, our nucleation algorithm can be improved including the consideration of the global energy not only for the relaxing process. Nonetheless we illustrated numerically our proposed mechanism for defect nucleation based on hoop stress thresholds at the rim of a crystalline spherical cap.

6.5 CONCLUSION

Our analysis led us to identify the in-plane hoop stress evaluated at the rim of the hemispherical cap as the most relevant quantity in order to explain defect nucleation. In the case of an irreversible self-assembly, the rim of the assembly is the only degree of freedom that enables to reduce the inherent geometric frustration due to the curvature. We showed in previous chapters that defect nucleation is able to relax locally compressive hoop stress at the rim and to ease further assembly. We computed radial and hoop stress profiles for different crystalline spherical structures and gave a way to evaluate them for various defect distributions, including scars. In agreement with the work of Azadi *et. al* [4], radial lines of dislocations are also efficient to relax internal stress during self-assembly. We proposed a mechanism to reach, for the case of large closed crystals, the ground state constituted of twelve disclinations decorated with multiple clouds of scars which lengths enhance the elastic stress relaxation. We observed further that using a single direction for defect nucleation leads to pictures and effects similar to the ones observed in the multidirectional case.

From all previous analyses, we draw here the final conclusion, different defect configurations can lead to similar stress relaxation patterns. However, we did not find a way to rationalize objectively the icosahedral symmetry of defect distributions found in Nature. Latter distributions require a global view point by considering total elastic

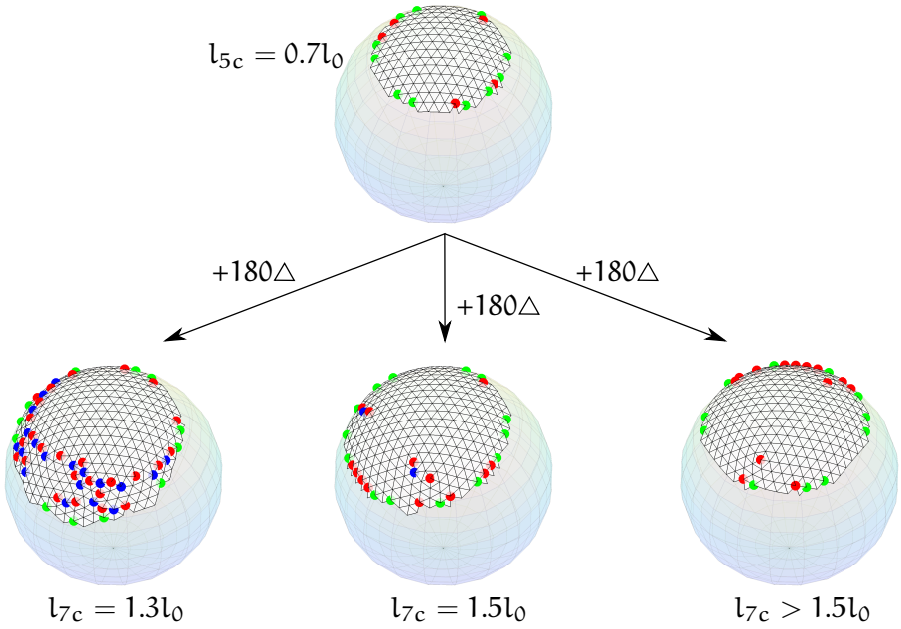

Figure 6.2 – Snapshots of self-assembly simulations showing nucleation of defects depending on hoop stress thresholds. l_0 is the equilibrium length of edges.The first closing threshold is associated to the length $l_{5c} = 0.7l_0$. Then we increase the closing threshold l_{7c}. If $l_{7c} = 1.5l_0$ no dislocation appears in the simulation, only disclinations. We precise that the radius of curvature $R_0 = 12l_0$ and we set the ratio of moduli $k_e/k_b = 100$. Red dots highlights pentamers, blue dots, heptamers and green dots, tetramers. Tetramers are considered as defects on the boundary, we expect trimers instead. Each arrow indicates that 180 triangles (coarse-grained proteins) are added under the specified conditions above and below.

energy for each distribution. We concluded from last section that disclination/dislocation preference is set by local stress profiles and molecular affinity between building blocks, switching single-defect regime to scar-dominated ones. In order to highlight defect nucleation mechanism, we chose a spherical surface as an idealized geometry and for the sake of calculation tractability. However, the mechanism proposed shall be valid for various other geometries and curvatures that are all sources of frustration. A given self-assembled system on a given substrate with given Gaussian curvature should possess particular stress patterns therefore leading to various profiles for defect distributions. For example, assuming self-assembly on a torus which possess inner negative Gaussian curvature, negative sevenfold defect distributions are more relevant as shown in literature [52].

Obviously, local rearrangements in the bulk of molecular self-assemblies are not taken into account in previous analyses. Disclination motions are unlikely to happen in a general way as they require large-scale rearrangement. Dislocation motions require mostly local rearrangement, and are determined and preferred at the biochemical level. If interaction between subunits are strong enough, relaxation in the bulk are not favorable, it is easier to reduce mechanical stress at the rim of the assembly [75]. Let us note also that finding optimal azimuthal positions of defects by searching for most negative hoop stress values is consistent with final symmetries found by minimizing global energies as the surface is growing [64]. Again, we recall that present work is not expected to be applied for closed structures, but only to those with moderate deviations from planar configurations. However, physical features previously presented for self-assembly might remain unchanged.

Part III

STIFFNESS HETEROGENEITY IN VIRUSES

> Ce que nous appelons les lois de la nature est l'ensemble des méthodes que nous avons trouvées pour adapter les choses à notre intelligence et les plier à l'accomplissement de nos volontés.
> – *Émile Boutroux*

7 (VIRTUAL) NANOINDENTATION

7.1 RÉSUMÉ

Cette partie et ce chapitre se focalise sur le second aspect des études virologiques, à savoir la nanoindentation des virus. On détaille ici les ingrédients numériques nécessaires que nous avons utilisé pour étudier "virtuellement" la nanoindentation de capsides virales sphériques. La réponse mécanique élastique du virus est étudiée en fonction de la forme de la pointe indentante du microscope à force atomique. La dépendance par rapport à la position de cette même pointe par rapport au virus est, par ailleurs, évaluée. Dans un deuxième temps, la précédente réponse élastique est également étudiée selon si le virus présente un aspect icosahédrique ou non. Ce précédent aspect découlant principalement des propriétés élastiques du virus lui-même.

7.2 INTRODUCTION

We investigate now mechanical properties of viruses using numerical and analytical models.

The main role of the capsid is to protect the viral genome against external aggressions. Consequently, as said earlier, capsids developed remarkable mechanical properties and strong resistivity to agressions from external environment. Atomic force microscopy has recently provided highly precise methods to probe mechanical properties of various viruses. Nevertheless, molecular details underlying viral mechanics remain unresolved. These remarkable properties can also be unveiled in single-virus nanoindentation experiments. In this chapter, we will present what we will call a Virtual Atomic Force Microscope (VAFM) combined with coarse-grained molecular dynamics simulations. The latter term was firstly introduced by Aznar, Roca-Bonet and Reguera in 2018 [8]. This study, we hope, will permit interpretation of experimental results at the molecular level. The combination of numerical results with analytical models enables us to scrutinize conformational effects on structural stiffness trend. It is also numerically possible to investigate how specific set-up experiments influence measurements of mechanical resistances. This study demonstrates that material proper-

We restrict our study to small deformations. Thus, viral shells shall behave as springs when nanoindented. It is possible to extract numerically their effective stiffness simulating a so-called Atomic Force Microscope.

ties of viral nanoparticles can be correctly described by both numerical and analytical approaches.

7.3 VIRTUAL ATOMIC FORCE MICROSCOPY

7.3.1 *Parametrization of the empty capsid*

Viruses can be seen as elastic curved crystals. In order to create a VAFM, we first coarse-grain the elastic biomembrane regarding it as a discrete thin elastic shell. Thus, constituting proteins become triangles of a spherical triangular lattice (provided $T \geqslant 4$). Although interactions between individual amino-acids are presumably very complex, effective acid-acid interactions and their hydrophobicity give the protein a rigidity. That is why we choose to coarse-grain our capsid at the protein level. Within such a numerical model, in-plane deformations are taken into account with bond deformations, varying their lengths. Out-of-plane deformations are taken into account varying angles between adjacent faces or triangles [94]:

$$F_d = \sum_{\langle i,j \rangle} \frac{1}{2} k_s (\ell_{\langle i,j \rangle} - \ell_0)^2 + \sum_{\alpha,\beta} k_b (1 - \cos\theta_{\alpha,\beta}), \tag{7.1}$$

To analyze and investigate mechanical properties of viral shells, we coarse-grain them at the protein level. Proteins are modeled as elastic triangles. Triangles can be stretched to simulate in-plane deformations and triangle pairs can be bent to simulate out-of-plane deformations.

where $\ell_{\langle i,j \rangle}$ is the length of the edge relating vertices i, j. When the latter length is different from the preferred one ℓ_0, the bond is stretched or compressed by a spring force proportional to the spring stiffness k_s. k_b sets the bending energetic cost for developing a non zero angle $\theta_{\alpha,\beta}$ between the two given adjacent faces α, β. The equilibrium length ℓ_0 is used to normalize distances, and our unit of energy is set to $k_B T$.

Each virus possess a magic T number (See Ch. 1). In order to refine previous coarse-graining, the latter parameter is chose as an input to build the final structure, preserving the particular symmetry and the particular (possibly non)-skew capsid shape. The structures are obtained using the java applet available at Ref. [31].

As previously said, an important parameter arises in our model previously presented, the Föppl Von-Karman ratio $\gamma = 4R_0^2 k_s / 3k_b$ balancing the in-plane/out-of-plane energies [27, 59], with R_0 the size of the spherical coarse-grained structure. We retrict our study to spherical viruses, so that $\gamma \simeq O(1)$, unless specified differently. At ambient temperature $T = 298K$, we set $k_s = 200 k_B T / nm^2 \simeq 120 kcal/mol/nm^2$ and $k_b = 80 k_B T \simeq 50 kcal/mol$ [8, 38, 87].

7.3.2 *Interactions with the substrate and with the tip*

The coarse-grained thin shell interacts both with the infinite flat substrate on which it is lying, and with the approaching spherical or conical tip (we can change the tip shape as it is described hereafter). Both influences are computed using a repulsive Morse potential on vertices:

The Morse potential is used to simulate repulsive interactions of both AFM tips and underlying substrate.

$$V(r) = \sum_i P(1 - e^{-r_i/a})^2. \tag{7.2}$$

P is its depth, r_i the distance between the i^{th} vertice and the tip (respectively the substrate) and a the width of the well. We sum over all vertices. Interactions are naturally repulsive at very short distance, and attractive at larger distance. We add a steric repulsive cost to each face to prevent the tip from entering the numerical virus. Actually, we consider also the repulsion of the barycenter of each face [87]. Points of contact with the substrate are not allowed to slide tangentially and fixed at their initial positions in order to prevent our numerical shell from rolling. In our simulation, we set $P = 2k_BT \simeq 1.2\,kcal/mol$ and $a = 2\,\text{Å}$.

7.3.3 *Simulation and relaxation*

We consider quasi-static indentation. Each time the AFM tip is lowered to indent the numerical shell, vertices of triangles are relaxed to their new equilibrium positions. We take into account thermal fluctuations. AFM tips are modeled either by a smooth cone or a sphere. We shall examine the difference between two cases.

The relaxation is done using a Langevin dynamics [3, 8, 86], *i.e*, for the i^{th} vertex, we compute the following trajectory for the relaxation:

$$\mathbf{r}_i(t + dt) = \mathbf{r}_i(t) - \frac{dt}{\gamma}\nabla(F_d + V) + \left(2\frac{k_BT\,dt}{\xi}\right)^{1/2}\eta, \tag{7.3}$$

where $\mathbf{r}_i$ represents the position of the vertex, $\nabla(F_d + V)$ the gradient of the latter elastic energy and of repulsive interactions to relax the system (from the tip and the substrate). Numerical computation of the gradient is inspired from Ref. [98] [1]. η is a Gaussian white noise vector included to mimic thermal fluctuations and ξ denotes the damping coefficient that enables solely to account for the effective mass of beads and frictional forces. $\xi = 1kcal/mol/nm$ to get good agreement with experimental diffusion time of capsomers. The integration time-step is set to $dt = 400\,fs$. We assume quasi-static nanoindentation, hence the tip is lowered from $9pm$ between each relaxation iteration that lasts

1. The technical report is amusingly from Walt Disney Animation studios.

2 µs. We ensured that equilibrium state is reached between each tip descent. Using numerical simulations allows also to investigate the precise influence of various parameters on viral mechanical properties such as the tip geometry (spherical or conical) and elastic parameters. The size and the shape of the tip can be changed very easily. In an attempt to do realistic nanoindentation simulations, we indent with a tip of radius $R_t = 1/5R_0$ (unless a different value is specified in following results). If the tip is chosen to be conical, half-angle of the cone is set to $\alpha = \pi/4$ (again, unless a different value is specified). Note that, due to the smallness of the majority of viruses, the conical tip is in fact a line-swept sphere where instead of a cylinder, a cone is smoothly joining the two half sphere ends. Only the Morse repulsion of the bottom sphere (of radius R_t) and of the conical part are taken into account during indentation using an algorithm inspired of Ref. [10]. To investigate more precisely VAFM experiments, latter parameters are tunable.

7.3.4 *Data extraction*

To extract effective numerical stiffnesses of numerical shells, elastic energy is plotted against the indentation depth. A quadratic fit suffices to compute the effective stiffness as the shell behaves like a spring.

From simulations, elastic energy-indentation curves are obtained, the position of the center of the VAFM tip is recorded and substracted with its initial position giving the indentation depth. The maximal indentation depth is set to $\delta_{max} = 0.3R_0$, provided the tip has not reach the bottom in the off-centered case. Indeed, when coordinates of the tip in the $x-y$ plane are not zeros, the position of the tip is carefully computed so that indentations begin at the contact of the numerical cap. Note that if the tip is not above the virus, the initial height of the tip is set equal to the radius of the virus. Data is stored between each relaxation step, and each nanoindentation experiments is repeated several times to check the reproducibility of the results (specified in captions of figures). A quadratic numerical fit of elastic energy of the form $F_d = k/2 \cdot \delta^2$ using the `Nonlinearfit` method of `Mathematica` enables us to extract the effective stiffness of the virus for each experiment and at each tip position (See Fig. 7.1, Subfig. C) for examples of fits). δ represents the indentation depth.

7.4 RESULTS

7.4.1 *Spherical tip VS Conical tip*

Unless specified, we chose to indent a skew virus which T-number is set equal to 9 ($h = 3, k = 0$). Because this structure is of intermediate size and it is technically easier to indent a region with no elastic effects due to disclinations. On Fig. 7.1, we plot the variation of effective stiffness of the numerical capsid against the lateral position of the tip of the VAFM. Results from conical and spherical indentations are both shown. Immediately, we see that, even far away from the center of the simulated virus, effective stiffness for the conical case does not vanish. This can be seemingly understood by the fact that the domain of influence of the cone is significantly larger than the pure sphere. Even when the tip is not above the virus, the conical part can still indent the numerical capsid. The latter phenomenon is sketched on Fig. 7.1, Subfig. B). We highlighted the conical tip-virus intersection with the blue dotted ellipse. This results into a mechanical response of the coarse-grained biological scaffold. Consequently, non-vanishing stiffness can be extracted from those particular nanoindentation experiments. This effective stiffness appears nearly constant with the error bars (See Fig. 7.1 for details). Regarding the spherical case, the extracted effective stiffness drops to zero far away from the coarse-grained virus. We note that when the tip is shifted not far away from the center of the capsid ($r < R_0$, where r represents the viral vertical axis-tip distance), for both conical and spherical tips, an important decrease of the stiffness is found (around 20% when the tip is shifted from a quarter of the capsid radius). The agreement between both cases in the "close-regime" suggests that the spherical part of the conical tip plays the major role in this region. Note that we normalize effective stiffnesses by the Laudau stiffness of a thin shell point-indented at the top, $k_L = Y/\sqrt{\gamma}$. Numerical average of top stiffnesses is in agreement with scaling of Landau *et al*. Indeed, $k_{max} \sim 50 k_B T/l_0^2 \sim D/R_0^2 \cdot \sqrt{\gamma} \sim Y\gamma^{-1/2}$.

Effective stiffness varies with lateral position of the AFM tip. However, particular trends are visible when the shape of the tip is changed. More specifically, when the tip is conical, the conical fraction plays a major role when the tip lateral position is changed. Non vanishing stiffness can be extracted even indenting far away from the shell.

7.4.2 *Geometrical dependance*

Previous qualitative agreement in the close regime for conical and spherical cases nurtures the need to specify previous stiffness dependence on tip shapes. As a result, we show on Fig. 7.2 the dependence of stiffness on the radius of the tip and on the conical angle. We vary

When the viral shell is very stiff, it exhibits a faceted shape. Disclinations point out of the shell creating nearly an icosaheder. Strong variations of effective stiffness can then be observed against lateral position of the tip. Pentamers are stiffer than hexamers. Effective stiffnesses thus depends also on intrinsic structures and molecular details of capsids.

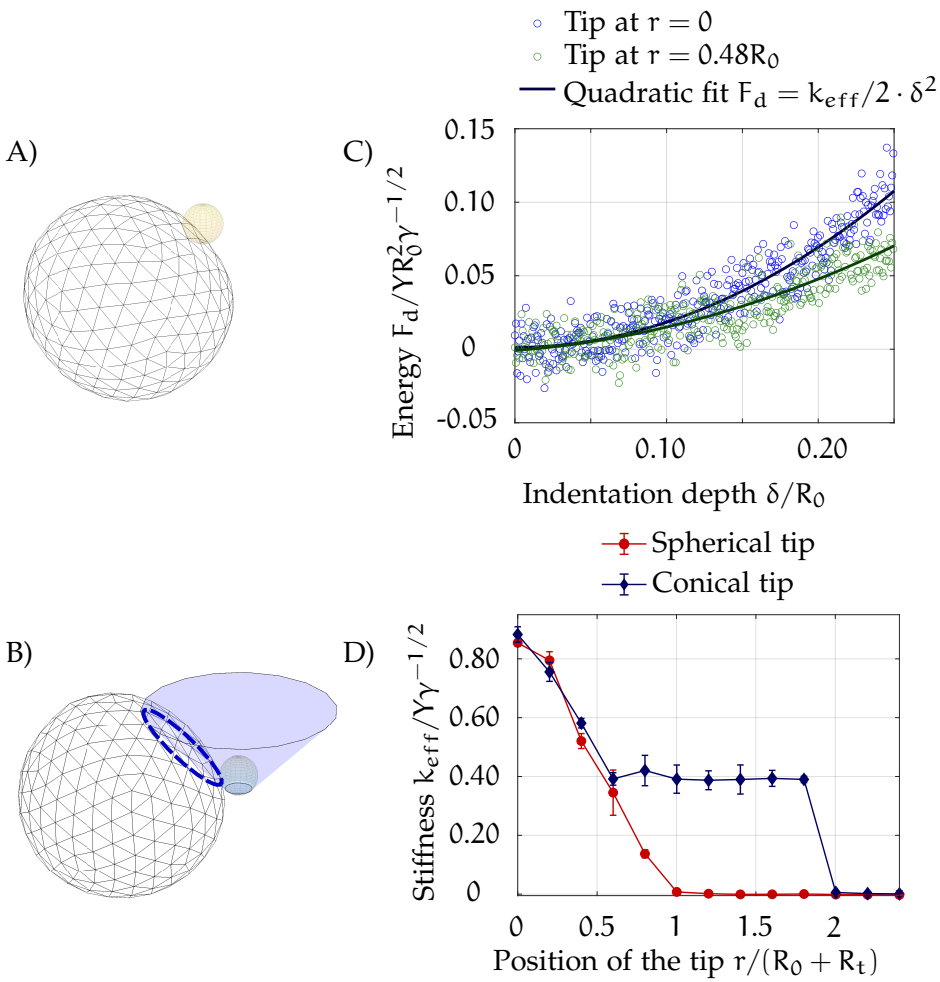

Figure 7.1 – Comparison of virtual nanoindentation experiments using a spherical or a conical tip. A) Snapshot of a virtual nanoindentation using a spherical tip. B) Snapshot of a virtual nanoindentation using a conical tip. Note that the conical part is indenting the numerical capsid. This is highlighted by the blue dotted ellipse. C) Quadratic fits of the discrete elastic energy against the indentation depth. Note the decrease of the effective stiffness when the spherical tip is off-centered. D) Extracted numerical stiffness against the position of the tip for the spherical tip (red circles) and the conical tip (blue diamonds). Each point of the curve is the average of 4 virtual indentations. The error bars are the corresponding root mean-square deviations. The stiffness does not vanish for $r > R_0 + R_t$ with the conical tip. Parameters of simulations: $R_t/R_0 = 1/5$, Semi-aperture of the cone $\alpha = \pi/4$, $\gamma = 57.6533$. Other parameters unchanged.

the aperture angle of the conical tip but also its bottom radius, and we compare the results to the first situation. We find that, if one increases the bottom radius of the conical tip, the plateau (i. e. the region where stiffness is constant with the tip position for indentations with a conical shape) is shifted to the right as function of the lateral position of the tip. This can be explained by the fact that, as the bottom tip is bigger, the transition between what we can call the spherical and the conical regimes appears later. Similarly, the higher the aperture angle is, the higher is the height of the plateau. The aperture angle seems to fix the effective stiffness that is extracted from conical indentation.

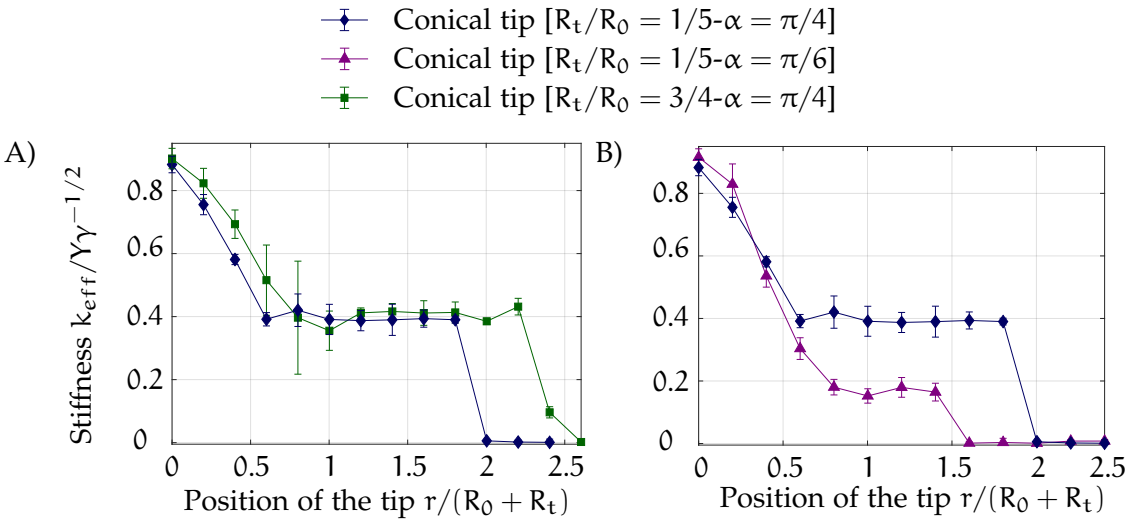

Figure 7.2 – Comparison of virtual nanoindentation experiments using various conical tips. A) Effective stiffness against the tip position, the aperture angle $\alpha = \pi/4$ is the same for both tips. Only the bottom radius was changed, for the blue diamond curve $R_t/R_0 = 1/5$, for the square green curve $R_t/R_0 = 3/4$. Note the shift to the right of the plateau for the bigger radius compared to the initial situation as function of the position of the tip. B) Here, both radii of conical tips are equal, only the aperture angle was changed, $\alpha = \pi/4$ for the blue diamond curve, and $\alpha = \pi/6$ for the magenta down triangle curve. Note the decrease of the heigth of the plateau with aperture angle of the cone. $\gamma \simeq 57.6533$. The experiment for each position was repeated 2 times, error bars correspond to square root type deviations. Other parameters unchanged.

7.4.3 *5-fold, 3-fold symmetries*

In previous studies, we loaded coarse-grained viral shells with small forces to probe their global elastic behavior. The latter seems logically dependent on the position of the tip, *i.e* the region indented. Nevertheless, several experimental and theoretical studies suggest that the elastic response also depends on internal structures of capsids. Specifically, for indentations along the 5-fold symmetry, for most viruses, capsids appear weaker in the studied regime, i. e. for $\gamma \simeq O(1)$ [8, 20, 24, 86]. We checked that our results are coherent with latter studies. We then investigate the robustness of the latter trend against the shape of the tip. On Fig. 7.3, we plot numerical stiffnesses extracted from indentations with a cone for various orientations of the numerical capsid. We also investigate the trend for a Föppl–Von-Karman number γ above the buckling transition, i. e. $\gamma \sim 500$. The various orientations of the shell were taken so that either a pentamer or an hexamer faces up the tip. Then, several trajectories are available. We can choose to off-center the tip to indent passing through a pentamer or an hexamer. We have then 4 cases to investigate. For $\gamma \sim 50 \leqslant 200$, no significant differences appear between cases. On the contrary, strong discrepancies appear after the buckling threshold. This is coherent with numerical results already obtained by Buenemann *et al.* and Widom *et al*. For $\gamma > 500$, the capsid has a strongly faceted shape. The twelve positive disclinations point out of the coarse-grained viral structure. This structural inhomogeneity induces a stiffer elastic response of pentamers compared to hexamers. Interestingly, the stiffer response of pentamers is observed whatever their positions in the structure of the shell. In other words, pentamers on top of the shell are stiffer than hexamers but this is also confirmed by the value of the stiffness plateau. For trajectories starting from a central pentamer, the plateau is higher if the trajectory ends on a peripheric pentamer rather than on a peripheric hexamer. However, the two last trajectories starting from a central hexamer to pass respectively on a peripheric pentamer and on a peripheric hexamer are more complex. We can legitimately think that they reflect a stronger contribution of the intrinsic structure of the shell. Going from one central hexamer towards a distal pentamer, the stiffness first increases, before decreasing in agreement with the first observed trend. This can be due to the "side" indentation of the distal pentamer. The stiffness extracted that way corresponds to 80% the one extracted when the indentation is performed at the top. Surprisingly, the stiffness plateau is the highest

when an indentation is performed on a distal hexamer. This can be due to the indentation of the so-called ridge between the two neighboring disclinations at high Föppl–Von-Karman number. This might ends up to the deformation of the two neighboring disclinations at large scale.

To conclude, for large Föppl–Von-Karman numbers, the dispersion of trajectories shows that the effective stiffness can also be strongly dependent on tip trajectories themselves. Latter results resonate with some previously presented [20] (See Ch. 4) and others presented by Aznar, Luque and Reguera [7]. Indeed, they showed that the bulk modulus $K_0 = -V \cdot \partial p/\partial V = R^2/9V \cdot \partial^2 E/\partial^2 R$ seem to be comparatively stiffer for icosahedral shell than for spherical one. In their notations, V is the volume of the shell, R its radius, E the energy and p the pressure. In words, K_0 measures the compressibility of the capsid. Additionally, polyhedral (*i.e* icosahedral) capsids systematically tolerate higher values of the bursting pressure than their spherical counterparts. Here, for a comparison, we submitted it to an external localized one. Consequently, the choice of an icosahedral instead of spherical shape seems to bring mechanical advantages that can play an important biological role. It can be now of interest to rationalize previously observed trends and more specifically the position-dependent one.

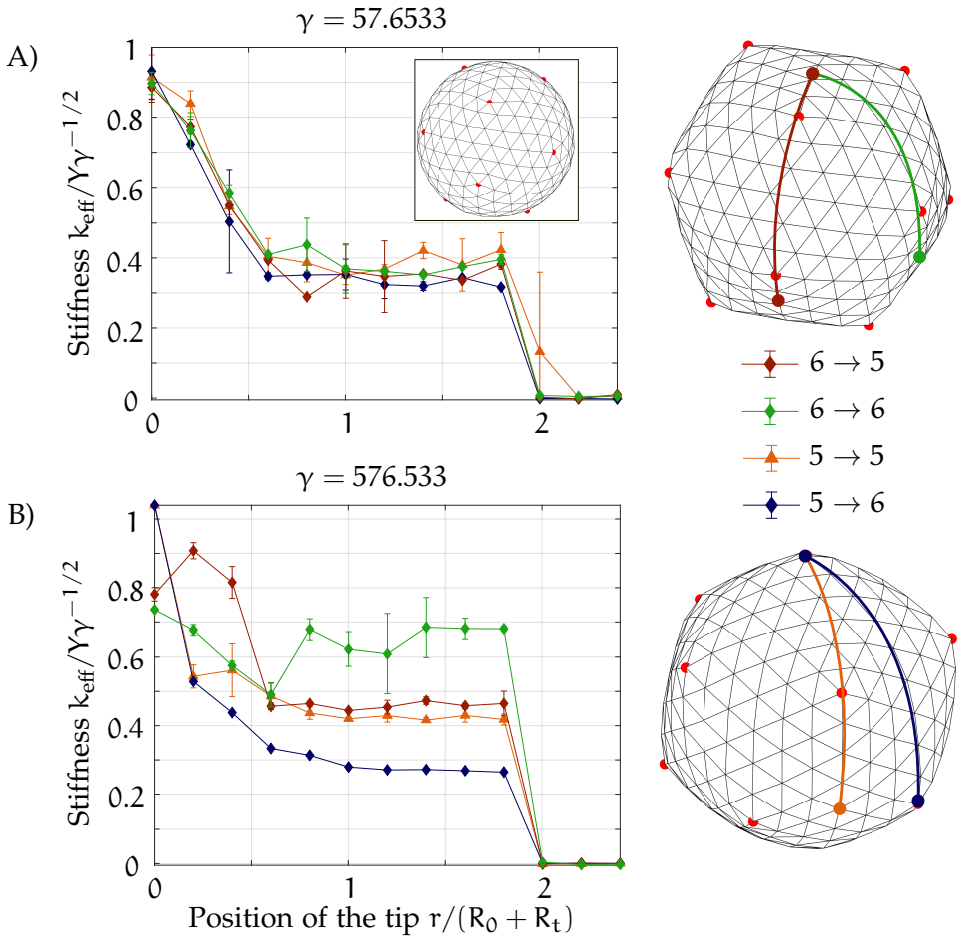

Figure 7.3 – Comparison of virtual nanoindentation experiments for various orientations and two different Föppl–Von-Karman numbers γ. A) Numerical effective stiffness against the position of the tip for various orientations of the numerical capsid, $\gamma = 57.6533$. Inset represents the structure of the capsid for such a γ. The orientations are taken in order to indent either on a disclination at the top or off-centered. Trajectories of the tip on the capsid are represented with the respective colors on sketches at the right. No significant differences can be noticed for this case. B) Numerical effective stiffness against the position of the tip for various orientations of the numerical capsid, $\gamma = 576.533$. Trajectories are represented with the same colors on the numerical capsid which structure is computed for latter γ. Strong discrepancies can be noticed. Parameters of the indentation and of the tip : $R_t/R_0 = 1/5, \alpha = \pi/4$. The experiment for each position was repeated 2 times, error bars correspond to square root type deviations. Other parameters unchanged.

8 GEOMETRICAL MODEL

8.1 RÉSUMÉ

Dans ce chapitre, les précédents résultats numériques obtenus sont analysés et rationalisés analytiquement. Un accord quantitatif est encore une fois obtenu.

8.2 INTRODUCTION

We recall here that scaling results obtained and summed up in Ch. 4 are done assuming that indentations are point-like. However, due to the smallness of some viruses, in particular the AAV or the HBV, the latter hypothesis is not valid. The AFM tip possess a finite curvature radius comparable to the studied particles that can be included in simulations or models. Deciphering the role of this finite curvature in nanoindentation experiments can be of significant interest. We aim in this chapter, using a simple geometrical model, to fill this gap and rationalize results of Ch. 7.

In this chapter, we distinguish two types of indentation:

— Spherical indentation, where the AFM tip is modeled by a sphere of radius comparable to the one of the viral particle.

— Conical indentation where the AFM tip is modeled using a conical tip ended by an hemisphere at the bottom. Its radius is also comparable to the size of the viral particle.

The different geometries considered are sketched in Fig. 8.1.

8.3 SPHERICAL NANOINDENTATION

In the case of a sphere-sphere indentation, Figure 8.1 highlights a strong decrease of the indentation depth. The latter decrease is accessible through the same vertical tip displacement if the tip moves from the top to the edge of the shell horizontally. Indeed, if the tip moves, let us say to the right of the shell, the corresponding shell deformation decreases too. This can be highlighted by the intersection between the viral sphere and the spherical tip (See Fig. 8.1, Subfig. A).

Previously observed trends are due to geometrical effects. When the tip is off-centered, the real indentation depth is smaller than the input vertical displacement. Hence, the elastic response of the viral shell is lower than the top-indentation response.

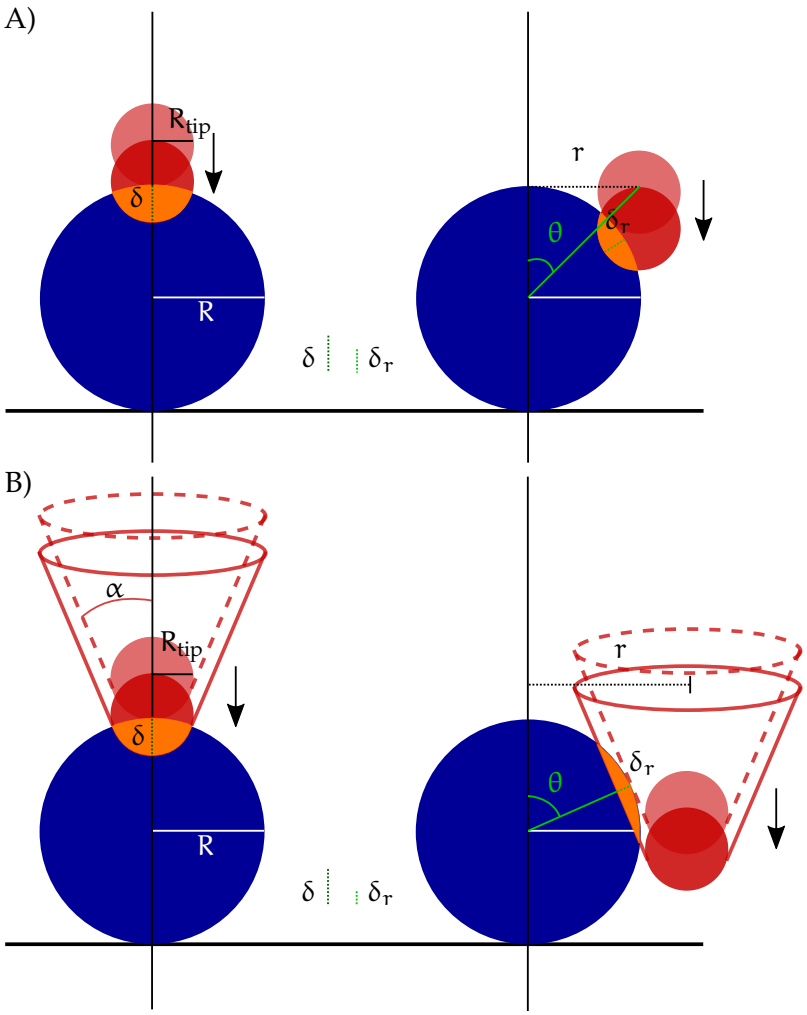

Figure 8.1 – Sketches of indentations. A) Indentation with a sphere, we highlight the fact that when the tip is off-centered, $X_{tip} = r$, the real indentation δ_r is less than the vertical descent or indentation δ. B) Indentation with a cone, the real indentation δ_r is constant after a given radial position of the tip $r = (R_0 + R_t)\cos\alpha$. Idealized deformed regions are highlighted in orange.

According to previous works, the size of the deformed zone scales as $d \sim R_0 \gamma^{-1/4}$, where R_0 is the radius of the shell and γ the Föppl–Von-Karman ratio [21]. However, the estimation of the overlaped regions provides us a simple way to quantify variations of deformations.

Here, we want to compute from vertical tip displacement δ drawn in Fig. 8.1, the real indentation depth δ_r. We assume small indentation (i. e. we restrict our study to non-inverted capsid). It is possible to determine the angle between the initial axis of symmetry of the experiment when the tip and the capsid are aligned with the new lateral position of the former, written r. The angle is denoted θ and it is possible to compute:

$$\cos\theta = \sqrt{1-\sin^2\theta} = \sqrt{1-\left(\frac{r}{R_t+R_0}\right)^2}, \tag{8.1}$$

where R_t denotes the tip radius. A straightforward geometrical computation enables to compute the real indentation depth:

$$\delta_r = \frac{1+\dfrac{\tilde{\delta}}{R_0-\tilde{\delta}} - \sqrt{1+\left(\dfrac{\tilde{\delta}}{R_0-\tilde{\delta}}\right)^2\left(\dfrac{1}{\cos^2\theta}-1\right)}}{1+\dfrac{\tilde{\delta}}{R_0-\tilde{\delta}}}, \tag{8.2}$$

where the variable $\tilde{\delta} = \delta\cos\theta/(1+R_t/R_0)$. In the limit of small indentation, when $\delta \ll R_0$, the real indentation depth reduces to:

$$\delta_r = \delta\cos\theta = \delta\sqrt{1-\left(\frac{r}{R_t+R_0}\right)^2}. \tag{8.3}$$

Consequently, the effective stiffness that shall be extracted either from simulations or experiments depends on the lateral position of the tip as (approximately):

$$k_{\text{eff}}^{\text{sphere}} = k_{\text{top}}\sqrt{1-\left(\frac{r}{R_0+R_t}\right)^2}. \tag{8.4}$$

8.4 CONICAL INDENTATION

In the case of the conical tip, we note α the aperture angle of the cone. The latter is terminated by an hemisphere of radius R_t. As for spherical indentation, extracted effective stiffness depends also on the lateral

position of the tip for conical indentation. Moreover, the previous proof is valid as soon as $r \leqslant R_0$. However, when the tip is moved far from the viral shell $r > (R_0 + R_t)\cos\alpha$, or simply when $\theta = \pi/2 - \alpha$, only the conical part of it is indenting. Additionally, real indentation δ_r associated to a vertical displacement δ is identical whatever the lateral position r. This is easily explained by the fact that the curvature that plays the major role in the indentation is zero and the overlap with the shell remains constant with r.

By geometrical analysis, one in fact writes:

$$\delta_r = \delta \sin\alpha. \tag{8.5}$$

When the cone indents, we deduce:

$$k_{\text{eff}}^{\text{cone}} = \begin{cases} k_{\text{top}} \sqrt{1 - \left(\dfrac{r}{R_t + R_0}\right)^2} & \text{if } r < (R_0 + R_t)\cos\alpha, \\ k_{top} \sin\alpha \text{ otherwise.} \end{cases} \tag{8.6}$$

Similarly, using a geometrical model, it is possible to recover and analyze the role of the conical fraction of the conical tip. However, no quantitative agreements are reached with pure geometry.

We compare our analytic predictions to numerical results on Fig. 8.2. The resulting stiffness variations, shown in Fig. 8.2, is similar to the observed numerical stiffness changes. The geometrical model predicts a decrease of the effective stiffness by off-centering the spherical tip towards vanishing values in qualitative agreement with simulations. For the case of the conical tip, a similar trend is observed as soon as the *spherical part* of the tip indents. Then, when the conical part indents, the effective stiffness reaches a non-zero constant value. This is also observed in the numerical experiments. However, we are driven to admit that numerical latter curves show a stronger decrease of stiffness compared to the simple geometrical model, suggesting the presence of other effects at play in the real system.

8.5 DISCUSSION

Comparing numerical results with models, trends appear correct but not the values. The two estimations in Eq. 8.4 and Eq. 8.6 assume that the shell does not move laterally under off-centered vertical indentation. Nevertheless, if the adhesion with the substrate is not strong enough, one shall reasonably expect the shell to move horizontally. Even, in the limit of weak adhesion, the shell can be expected to escape from the imposed indentation constraint by rolling or sliding sideways. This additionnal shift could lower the resulting stiffness as it reduces

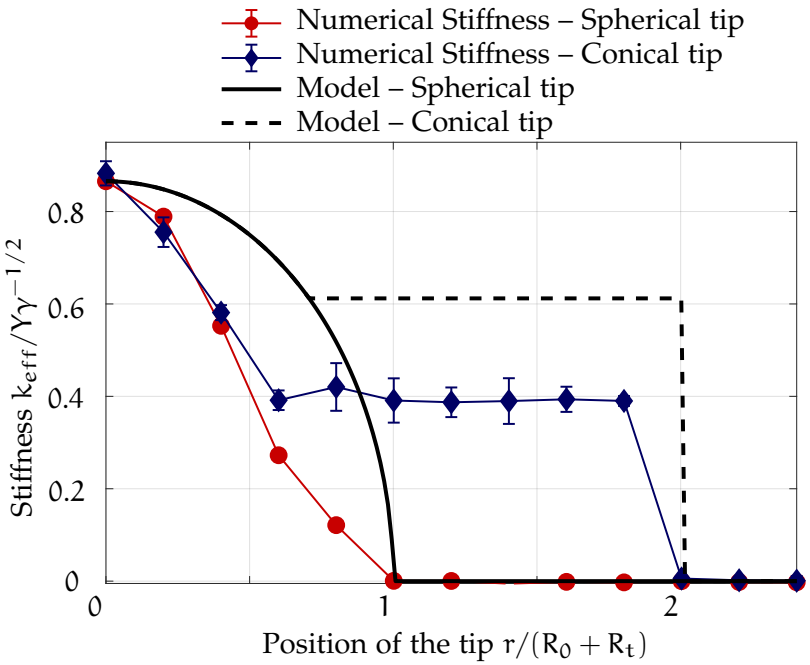

Figure 8.2 – Effective stiffness against the position of the tip. The red curve represents the numerical stiffness obtained by indentation with a spherical tip, the blue curve represents the numerical stiffness obtained by indentation with a conical tip. Plain and dotted lines correspond to the respective analytical model. The trends appear to be correct for both cases but no quantitative agreement is observed. This can be due to the strong "no lateral movement" assumption. Parameters of the simulations: $\gamma = 57.6533$, $R_t/R_0 = 1/5$, $\alpha = \pi/4$ (for the cone). Each dot is the mean of 4 numerical experiments, error bars correspond to square root type deviations. Other parameters unchanged.

the accessible deformation. Consequently, the first major correction that can be brought to the geometrical model is to take into account horizontal displacements which may be concomittant with vertical indentations (See Fig. 8.3).

For the spherical case, it is possible to estimate the horizontal shift written δ_h by assuming that the vertical indentation produces it. Consequently, we should correct Eq. 8.3:

$$\delta_r = \delta \cos\theta = \delta \sqrt{1 - \left(\frac{r + \delta_h}{R_t + R_0}\right)^2}. \tag{8.7}$$

Consequently, the viral shell remains at its position if the horizontal restoring force computed as $F_h \sim k_{adhesion}\delta_h$, where $k_{adhesion}$ is an estimation of the response, balances the horizontal component of the indentating force $F^h_{indentation}$ estimated as:

$$F^h_{indentation} = k_{top}\delta_r \frac{r + \delta_h}{R_0 + R_t}. \tag{8.8}$$

We shall take into account horizontal response when the tip is off-centered. And this, for both shapes. Including and taking into account horizontal contribution enables to recover quantitative agreements. Effective stiffness dependence against lateral position of AFM tip is now rationalized for both conical and spherical shapes.

Hence, one can estimate the horizontal shift as:

$$\delta_h \sim \delta \frac{k_{top}}{k_{adhesion}} \frac{r}{R_0 + R_t}. \tag{8.9}$$

This simple scaling, enables us to deduce that the horizontal displacement increases with lateral position of the tip r and decreases with adhesion efficiency $k_{adhesion}$. To test the latter scaling, we choose to compute resulting horizontal displacement of the barycenter of all vertices for each numerical indentation experiment. This is done for different tip positions. Within simulations, we can indeed compute, for each lateral position, the net horizontal shift of the shell center of mass compared to the original position prior to indentation. This is shown in Fig. 8.4 respectively for spherical and conical tips. It is observed within these plots that horizontal shift increases first linearly with lateral position, in qualitative agreement with scaling prediction reported in Eq. (8.9). The latter shift can be associated to a more global deformation rather than a pure vertical one.

Let us note that Eq. (8.9) can be rewritten as $\delta_h = Ar$, where A introduces a rescaling that depends on specific adhesion parameters and geometrical ones. Then, this enables us to rescale Eq. (8.4) and to write:

$$k^{sphere}_{eff} = k_{top}\sqrt{1 - \left(\frac{r}{R_t + R_0}\right)^2 (1 + A)^2} \tag{8.10}$$

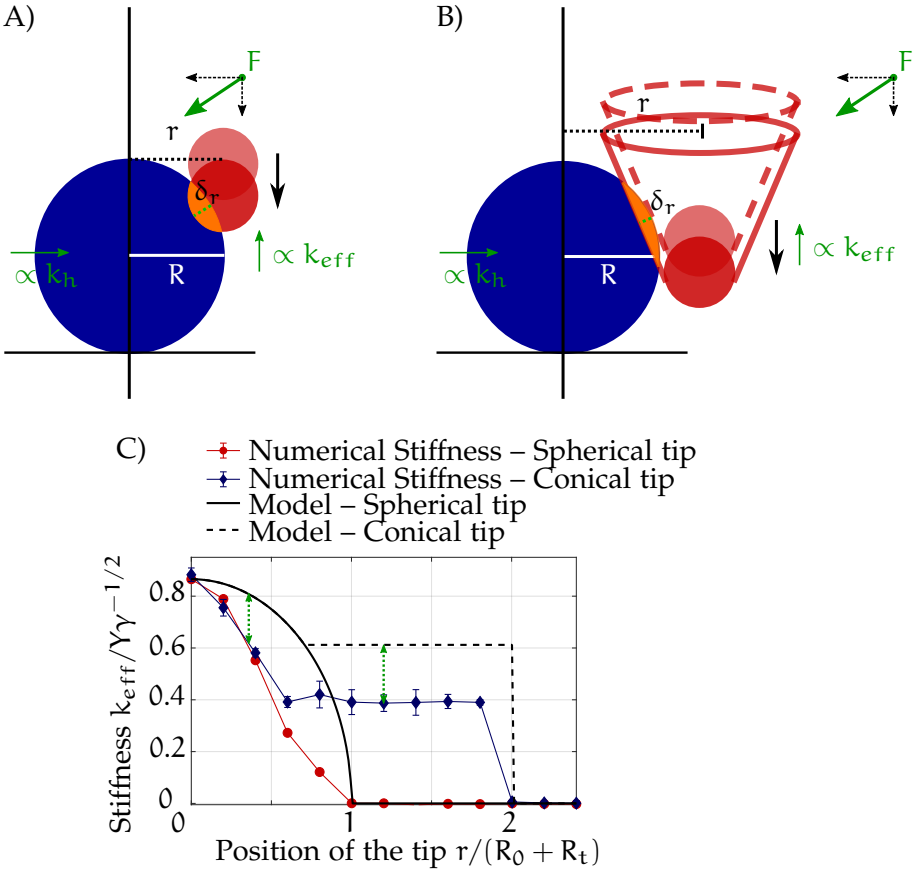

Figure 8.3 – The need to take into account the horizontal response of the capsid. When the tip is off-centered, the capsid response possesses an horizontal component F_h. The latter component is highlighted for both spherical A) and conical B) cases. C) The quantitative disagreement between the geometrical model and the numerical results for quantitative stiffness as function of the lateral position of the tip may be due to this horizontal response. Parameters of the simulations: $\gamma = 57.6533, R_t/R_0 = 1/5, \alpha = \pi/4$ (for the cone). Each dot is the mean of 4 numerical experiments, error bars correspond to square root type deviations. Other parameters unchanged.

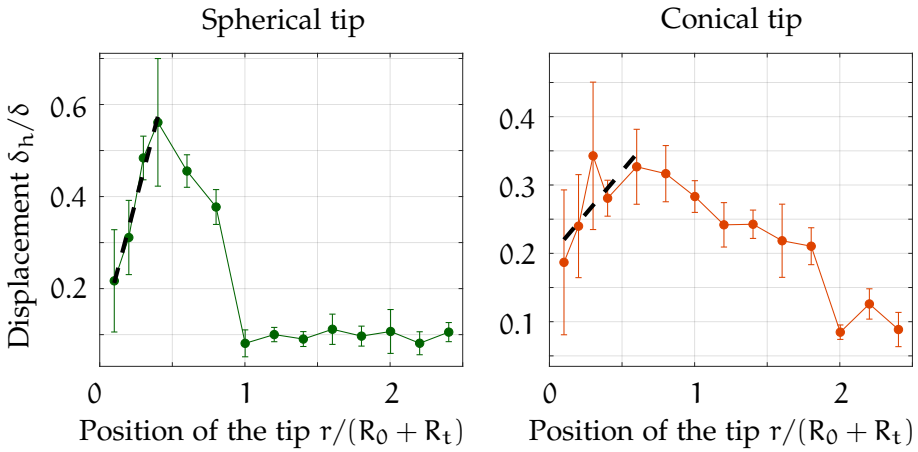

Figure 8.4 – Horizontal displacement of the barycenter of all vertices against lateral position of the tip. A linear trend appears for both shapes of tip (spherical or conical) in agreement with Eq. (8.9) presented in main text. Parameters of the simulations: $\gamma = 57.6533, R_t/R_0 = 1/5, \alpha = \pi/4$ (for the cone). Dots represents the mean of 4 simulations and error bars correspond to respective square root deviations.

As a consequence, a stronger decrease of stiffness is predicted compared to the original geometrical model. This argument can also be applied to the conical model. A becomes an adjustable parameter, and the corrected geometrical model shows a much better agreement with numerical data (See Fig. 8.5).

We check that an agreement is reached for various parameters (See Fig. 8.5). The plateau stiffness seems to depend only on the opening angle of the conical part of the tip but not on the radius of the swept sphere terminating the cone itself in agreement with Eq. (8.6). On the contrary, the transition between what we can call the spherical regime and the conical regime depends on both the opening angle of the cone and of the radius of the spherical part of the tip. Again, a quantitative agreement between the numerical model and the analytical one is obtained. We thus demonstrated and discussed that stiffness heterogeneity depends strongly on lateral positions of the tip. The latter effect should then be considered in experimental investigations on an equal foot with pH condition, substrate interaction (partly taken into account in our model) and viral capsid shape effects.

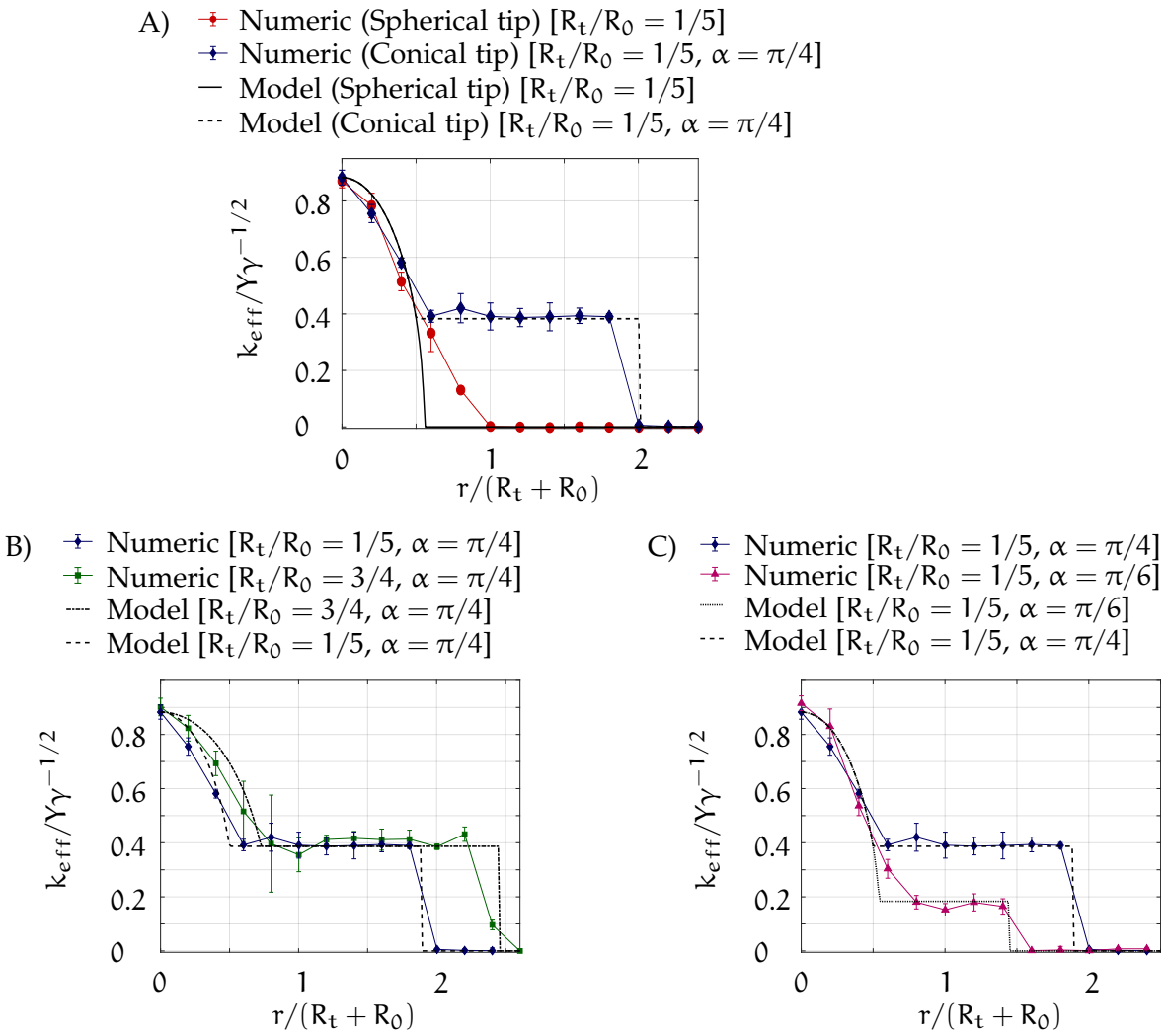

Figure 8.5 – Effective stiffness against lateral position of the tip for various conical shapes. Colored curves represent numerical results. Plain and dotted lines correspond to respective corrected analytical models. Trends appear to be correct and a quantitative agreement is reached for all cases. The lateral movement is included in the model. Parameters of the simulations: $\gamma = 57.6533$. Respective parameters are specified above each figure. Other parameters unchanged.

8.6 CONCLUSION

We showed that the shape of the AFM tip and its lateral position play a major role in stiffness extraction during an indentation experiment. Indeed, for the spherical case, as soon as the lateral position of the tip is greater than the capsid radius, the effective stiffness vanishes. Though, it is still possible to extract a stiffness that represents nearly 50% of the value that can be extracted for a top-indentation when the tip possess a conical shape. The important decrease of effective stiffness when the tip is off-centered (around 20% when the tip is moved by 20% of the radial size of the capsid) seems partly due to a pure geometrical effect for both cases. Indeed, the deformation of the capsid is lowered when the tip is off-centered. Consequently, the necessary mechanical response to balance the deformation can also be less important. Hence the decrease for the extracted stiffness. However, there exists a supplementary horizontal response. Due to the off-centering of external constraints, the reaction of viral capsids is not purely vertical but also horizontal. It is mandatory to take into account those two reacting components in the viral response to reach an agreement between analytical and numerical results.

In addition, we recall that when building blocks of viral capsids are resistant to in-plane compression, spherical capsids exhibit a faceted shape that resembles an icosaheder. In this particular regime, disclinations (i. e. pentamers), located at the summit of the matching icosaheder, are stiffer than hexamer lattices located on faces. More surprisingly, the regions linking neighboring disclinations (i. e. the edges of the icosaheder) have an average effective stiffness greater than all other areas on the viral surface. In the latter regime, strong discrepancies in extracted effective stiffnesses can arise depending on regions indented in the *intrinsic* viral structure.

Latter results were derived using numerical simulations. They were then rationalized analytically. An experimental evidence misses in our study, but investigations are currently performed in the laboratory. The results were not completely analyzed by the time the manuscript was written. We hope to present global results in the near future. Local protein deformations are not taken into account in our study, due to the coarse-grained nature of our simulations. We chose to model proteins, building blocks of capsids, as simple triangles to be stretched. Nevertheless, their hydrophobic character grants them a certain rigidity to build a stable scaffold (chemical reactions and allostery set aside) [56,

57, 78, 84] making our assumption reasonable. Instead of computing the 3D deformation of the capsid, we chose to focus on the main indentation variable, the indentation depth. The reduction of latter variable as function of lateral position of the tip provided us reasonable agreement with numerical data. In agreement with Lenz and Buenemann [20, 21], whose numerical model is similar to ours, no difference can be noticed between hexamers and pentamers for spherical and relatively stretchable viruses. From an experimental view point, no bimodality was detected for λ-phage for instance [70]. However, in the MVM, no sensible difference between pentamer and hexamer is seen for empty capsid, while there is a difference in the presence of internal genome [24]. Internal pressure brought by the viral genome, not taken into account in our model, could rend the capsid faceted, thus creating the observed bimodality. Previous observed trends can recall similar results regarding plant tissue mechanics where it has been shown that the consideration of local differences in mechanical properties are essential for proper data interpretation [88]. In a plant tissue, local stiffness measurements can vary with the level of turgor pressure (caused by osmotic flow of water through the cell walls) in an unexpected way. The previous turgor pressure can play, by analogy, the same role as our DNA internal pressure. Thus enhancing the previously observed trends. In the buckled regime, our model is incorrect at least quantitatively. However, we can still expect the qualitative geometrical trend. Latter geometrical effect is thus to be combined with intrinsic capsid structural effects. Indentation depths remain small in our model, it can be of significant interest to pursue indentations to deeper depths to observe non-linear reactions, especially for buckled shells. It has been observed that graphene cones have two degenerate configurations: their original shape and its inverse. However, if the local reflection symmetry of the graphene sheet is broken by the chemisorption of just five hydrogen atoms to the apex, then the maximal yield strength of the cone increases significantly [58]. Those results also resonate with ours, where pentamers exhibit locally a conical shape, pointing outwards the viral shell. We hope the previous study to motivate further ones focusing on effects of other tip shapes and non-spherical viruses. We also modestly aimed at easing interpretation of nanoindentation experimental results to unveil various aspects of viral nanomechanics. We hope this study to be profitable and experimentally checked in the future.

CONCLUSION

Viruses are constituted of several layers that contain the viral genome. They are possibly made of a lipid enveloppe and always of a matrix protein and the capsid. The capsid is the most important part of the virus as it encloses and protects the viral genome. The viral genome encodes both the genome and conveys the infection generally. Capsids are self-assembled systems made of proteins arranged in multimers. Some are arranged into hexamers (the most efficient packing of proteins), others into pentamers (fivefold defects). From the topological view point, pentamers are called *disclinations*. Due to a topological constraint, a capsid (an assembly topologically equivalent to a sphere) must contain exactly 12 isolated positive disclinations. Those disclinations are remarkably useful to relax the elastic stress created by the curvature to complete the biological shell. They seem to nucleate at the most compressive regions of the unclosed self-assembled systems. The Gaussian curvature of the growing surface is a source of in-plane stress. A given distribution of Gaussian curvature will therefore generate a particular stress pattern at the rim where the assembly is effectively proceeding. Nucleating a *fivefold defect* in the hexagonal packing will reduce locally along the rim the mechanical stress. Interestingly, the introduction of a disclination leads to a tensile elastic burst. This tensile burst can be relaxed by the inclusion of a sevenfold defect (heptamers) in a similar manner. The latter nucleation of a pentamer-heptamer pair is topologically called a *dislocation*. Dislocations tends to align themselves into *scars*. They were not observed yet in viral capsids though they are present in other biological self-assembled systems such as clathrin or microtubules. We chose then, to include them in the present study. It is observed that all the defect arrangements produce similar patterns of hoop stress reliefs at the rim of the surface: close to the defect, the hoop stress is relieved and becomes positive, while this stress relief decreases when positions diametrically opposed to the defect(s) are reached. However, when the size of the structure is increased, a so-called charged scar (a scar terminated by a disclination) provides more efficient long range stress relaxation at the rim than an isolated disclination. This observation is compatible with the presence of radial scars in the ground state energy of closed shells with large

radii previously mentioned in several studies. Our work is therefore able to provide an assembly pathway leading to the observed ground state for a closed shell. We shall underline that the latter results were found assuming the irreversibility of the growing structure. In other words, this neglects any further rearrangement away from the rim, in the bulk of the structure that has been assembled. These rearrangements represent another degree of freedom that could be used in order to relax the mechanical stress. However, their contribution might not be as important for two reasons. First, single disclination motion requires large scale rearrangements and is therefore unlikely to happen. On the other hand, dislocation motion is known to require mostly local structural changes, and it is the cost of these changes that will determine if the structure can relax using dislocation motion. We expect the interaction between subunits to be strong enough (around $20k_BT$) that bulk defect mobility becomes again unlikely. Let us notice that our model is resolved using polar coordinates on spherical scaffolds for the sake of tractibility and it is therefore expected to only apply for structures with moderate deviations from a planar configuration. The physical ingredients, though, seem essentially described.

Focusing on the high resisitivity of closed capsids against external applied load, we proved again the usefulness of disclinations. Provided the stretching energy to be high enough, disclinations exhibit a significant higher effective stiffness compared to sixfold faces. Using a coarse-grained numerical model for capsids, we proved them to resist significant loads if a disclination is indented. However, the most useful result is enlightened when the stretching and the bending components of the elastic energy are comparable. Using, once again, a numerical model for vitual indentation experiments, we showed that the shape of the tip plays a significant role in effective stiffness measurements. Because of the smallness of viruses, even the tip of an atomic force microscope resembles to a cone terminated by a swept sphere. We demonstrated that such a shape can lower the experimental measurement if the viral particle and the tip are not aligned vertically. This is due to a lower deformation compared to top indentation. This lower deformation is the consequence of the particular geometry of the system. These results should have been expected, but our work provides for the first time a refined quantitative model to take into account the latter geometrical effect. Remarkably, numerical and analytical results coalesce. If the tip is moved from the top by 20% the radius of the viral particle, a drift that is thermically accessible, the same reduction

is observed onto the extracted numerical stiffness. We expect the same reduction in experiences. Again, due to the contribution from the conical side of the AFM tip, it is possible to extract a non-vanishing stiffness even if the virus is not indented. Knowing this value enables to recover the top effective stiffness. All the latter results were derived using a coarse-grained numerical model. However interactions between individual amino-acids are presumably very complex, the effective acid-acid interactions and their hydrophobicity give the protein a certain rigidity that enables us to model it as a rigid building block.

We hope that the present work will motivate future investigations, extending the presented models in order to describe defect nucleation until full completion of the spherical surface, or to describe the interplay between tip geometries and viral capsid shapes.

CONCLUSION

Les virus sont donc constitués de plusieurs couches contenant le génome viral. Ils sont possiblement constitués pour partie d'une enveloppe lipidique et toujours d'une matrice protéique et de la capside. La capside est la partie la plus importante du virus contenant le génome. Ce génome encode à la fois l'infection et la structure du virus. La capside est un système auto-assemblé fait de protéines arrangées en multimères. Certains d'entre eux sont des pentamères, d'autres des hexamères (l'hexamère étant le paquetage optimal pour les protéines constituant la capside). D'un point de vue topologique, les pentamères sont appelés *disclinaisons*. En raison de la contrainte topologique, toutes les capsides sont topologiquement équivalentes à des sphères, il doit donc y avoir exactement 12 disclinaisons positives et isolées dans l'assemblage protéiques. Ces disclinaisons sont particulièrement utiles pour relâcher la tension élastique créée par la courbure à la bordure de l'assemblage. Il semble que ces dernières nucléent au point de compression maximale de l'assemblage biologique incomplet. En effet, la courbure gaussienne de la surface croissante est une source de stress élastique dans le plan. Une distribution donnée de courbure Gaussienne engendrera donc une certaine distribution de stress à la bordure où l'auto-assemblage procède effectivement. La nucléation d'une disclinaison dans l'organisation hexagonale réduira ainsi le stress élastique le long de la bordure de l'échafaudage biologique. De manière intéressante, l'introduction d'une telle disclinaison génère dans l'environnement immédiat une contrainte extensive. Cette dernière peut alors être relâché de manière très similaire par l'introduction d'un heptamère. Cette dernière nucléation d'une paire pentamère-heptamère est topologiquement appelée *dislocation*. Ces dislocations ont tendance à s'aligner en cicatrices dans des structures biologiques variées. Elle n'ont pas encore été observées dans des capsides, mais existent dans d'autres systèmes biologiques, tel que la clathrine ou les microtubules. Nous avons donc choisi d'inclure ce nouveau type de défauts dans la présente étude. Nous avons par la suite observé que ces divers arrangements de défauts produisent des effets de relaxation très similaires sur le stress élastique en bordure : proche du défaut, la tension azimuthale est relâchée pour redevenir extensive. Cependant, ce relâchement se

réduit peu à peu alors que l'on s'éloigne du défaut et la tension azimuthale redevient alors compressive en région diamétralement opposée. Mais, au cours de la croissance de la structure, on s'aperçoit que les cicatrices chargées (c'est à dire les cicatrices terminées par une disclinaison isolée) permettent une meilleure relaxation à longue distance comparée à celle induite par une disclinaison seule. Ce résultat est compatible avec les larges structures sphériques closes exhibant des cicatrices radialement alignées dans leurs états fondamentaux, dernières structures mentionnées dans la littérature. Nous nous devons de tout de même souligner que les résultats précédents furent déduits en supposant l'irréversibilité de l'assemblage. En d'autres mots, on néglige des arrangements supplémentaires dans le corps de l'échafaudage biologique. Mais on peut légitimement supposer que ce degré de liberté supplémentaire pour la relaxation est d'une contribution négligeable pour deux raisons. Premièrement, le mouvement d'une disclinaison isolée requiert des réarrangements sur des dimensions comparables à la taille de la structure incomplète. Ces mouvements sont donc energétiquement défavorables. Les dislocations sont en revanche plus mobiles, leurs mouvements nécessitant un réarrangement plus local. Mais l'interaction protéique d'une énergie d'environ $20k_BT$ à température ambiante est supposée suffisamment élevée pour prévenir de tels mouvements. Nous devons aussi ajouter que les résultats présentés au cours de ces travaux furent déduits et calculés dans une géométrie polaire sur un assemblage sphérique à courbure modérée, et ce, pour des raisons de tractabilité. Les mécanismes physiques et les ingrédients essentiels semblent, en revanche, décrits.

En se focalisant ensuite sur la resistivité des capsides aux contraintes extérieures, nous avons également démontré l'utilité des disclinaisons. Si l'énergie élastique de tension (dans le plan) est suffisamment élevée, les disclinaisons possèdent une raideur effective significativement plus élevée que les faces paquetées hexagonalement. En utilisant un simple modèle gros-grain pour modéliser une capside virale, nous avons démontré qu'elles sont capables de résister à des chargements plus élevés si une disclinaison est effectivement indentée. En revanche, nous estimons que ce travail met en lumière un résulat plus utile quand le coût energétique de déformation hors du plan est comparable à celui de la déformation dans le plan. En utilisant, à nouveau, un modèle gros-grain numérique pour la capside, nous avons pu démontrer que la forme de l'objet biologique et la forme de la pointe utilisée pour l'indentation jouent un rôle non négligeable sur la raideur effective

pouvant être extraite au cours d'une telle expérience. En effet, en raison de la très petite taille des virus, une pointe de microscope atomique peut être vue comme un cône en terminaison sphérique. Cette forme particulière diminue effectivement la raideur effective extraite au cours d'une expérience d'indentation. Ceci est en fait une conséquence purement géométrique, la zone déformée si la pointe et le virus ne sont pas verticalement alignés étant plus petite, ce dernier résultat était parfaitement prévisible. Néanmoins, notre travail propose pour la première fois un modèle quantitatif pour prendre en compte cette moindre déformation géométrique. Si la pointe d'un microscope à force atomique est excentré de 20% du rayon du virus étudié, ce qui est thermiquement possible aux échelles étudiées, une réduction comparable est observée sur la mesure de raideur effective. On s'attend aux mêmes conséquences expérimentalement. De plus, en raison de la partie conique de la pointe d'AFM, il est possible d'extraire une raideur, et ce même si la pointe n'indente pas effectivement le virus. La pointe tombe, en fait, en dehors du virus. Avec le modèle proposé, il est tout de même possible de remonter à la raideur effective si la pointe indentait effectivement au sommet. Ces derniers résultats, furent déduits en utilisant un modèle gros-grain numérique pour la capside et un modèle géométrique. Ces résulats coalescent toutefois remarquablement. Nous n'avons pas réalisé d'études "tout atomes" en raison des interactions présumées complexes entre les acides aminés constituant les diverses protéines, blocs primaires d'une capside virale. Mais l'interaction acide-acide et leurs hydrophobicités respectives confèrent à la protéine une relative rigidité, ce qui rend nos hypothèses de travail acceptables.

Nous espérons finalement que ce travail permettra de futures recherches qui étendront possiblement les modèles précédemment proposés dans le but de décrire la nucléation des défauts jusqu'à achèvement complet d'une capside virale ou d'une coque biologique et/ou de décrire encore mieux l'interaction pointe d'AFM-morphologie virale.

BIBLIOGRAPHY

BOOKS

[2] Peter M Anderson, John P Hirth, and Jens Lothe. *Theory of dislocations*. Cambridge University Press, 2017.

[9] JB Bancroft. *The self-assembly of spherical plant viruses*. Vol. 16. Elsevier, 1970, pp. 99–134.

[28] Donald LD Caspar and Aaron Klug. *Physical principles in the construction of regular viruses*. Vol. 27. 1962, pp. 1–24.

[37] Boris A Dubrovin, Anatolij Timofeevi Fomenko, and Serge Petrovich Novikov. *Modern geometry—methods and applications: Part II: The geometry and topology of manifolds*. Vol. 104. Springer Science, Business Media, 2012.

[61] Lifshitz E.M. Landau L.D. *Vol.07. Theory of elasticity*. 3ed. Butterworth-Heinemann, 1986.

[80] William H Press, Saul A Teukolsky, Brian P Flannery, and William T Vetterling. *Numerical recipes in Fortran 77: volume 1, volume 1 of Fortran numerical recipes: the art of scientific computing*. Cambridge university press, 1992.

[90] Jean-François Sadoc and Rémy Mosseri. *Geometrical frustration*. Cambridge University Press, 2006.

[96] Peter G Stockley and Reidun Twarock. *Emerging topics in physical virology*. World Scientific, 2010.

[99] Eduard Ventsel Theodor Krauthammer. *Thin plates and shells: theory, analysis, and applications*. 1st. CRC Press, 2001.

[100] Stephen P Timoshenko and James M Gere. *Theory of elastic stability*. Courier Corporation, 2009.

[101] Stephen Timoshenko. *History of strength of materials: with a brief account of the history of theory of elasticity and theory of structures*. Courier Corporation, 1983.

[110] Gordon Ethelbert Ward Wolstenholme and Maeve O'Connor. *Principles of biomolecular organization*. Vol. 969. John Wiley & Sons, 2009.

ARTICLES

[1] Mavis Agbandje-McKenna, Antonio L Llamas-Saiz, Feng Wang, Peter Tattersall, and Michael G Rossmann. « Functional implications of the structure of the murine parvovirus, minute virus of mice. » In: *Structure* 6.11 (1998), pp. 1369–1381.

[3] Anton Arkhipov, Wouter H Roos, Gijs JL Wuite, and Klaus Schulten. « Elucidating the mechanism behind irreversible deformation of viral capsids. » In: *Biophysical journal* 97.7 (2009), pp. 2061–2069.

[4] Amir Azadi and Gregory M Grason. « Defects in crystalline packings of twisted filament bundles. II. Dislocations and grain boundaries. » In: *Physical Review E* 85.3 (2012), p. 031604.

[5] Amir Azadi and Gregory M Grason. « Emergent structure of multidislocation ground states in curved crystals. » In: *Physical review letters* 112.22 (2014), p. 225502.

[6] Amir Azadi and Gregory M Grason. « Neutral versus charged defect patterns in curved crystals. » In: *Physical Review E* 94.1 (2016), p. 013003.

[7] Maria Aznar, Antoni Luque, and David Reguera. « Relevance of capsid structure in the buckling and maturation of spherical viruses. » In: *Physical biology* 9.3 (2012), p. 036003.

[8] María Aznar, Sergi Roca-Bonet, and David Reguera. « Viral nanomechanics with a virtual atomic force microscope. » In: *Journal of Physics: Condensed Matter* 30.26 (2018), p. 264001.

[10] Aurelien Barbier and Eric Galin. « Fast distance computation between a point and cylinders, cones, line-swept spheres and cone-spheres. » In: *Journal of Graphics tools* 9.2 (2004), pp. 11–19.

[11] Mark Bathe. « A finite element framework for computation of protein normal modes and mechanical response. » In: *Proteins: Structure, Function, and Bioinformatics* 70.4 (2008), pp. 1595–1609.

[12] AR Bausch, Mark John Bowick, A Cacciuto, AD Dinsmore, MF Hsu, DR Nelson, MG Nikolaides, A Travesset, and DA Weitz. « Grain boundary scars and spherical crystallography. » In: *Science* 299.5613 (2003), pp. 1716–1718.

[13] Jordan Benjamin, Barbie K Ganser-Pornillos, William F Tivol, Wesley I Sundquist, and Grant J Jensen. « Three-dimensional structure of HIV-1 virus-like particles by electron cryotomography. » In: *Journal of molecular biology* 346.2 (2005), pp. 577–588.

[14] Mark J Bowick, Angelo Cacciuto, David R Nelson, and Alex Travesset. « Crystalline particle packings on a sphere with long-range power-law potentials. » In: *Physical Review B* 73.2 (2006), p. 024115.

[15] Mark J Bowick, David R Nelson, and Alex Travesset. « Interacting topological defects on frozen topographies. » In: *Physical Review B* 62.13 (2000), p. 8738.

[16] Mark Bowick, Angelo Cacciuto, David R Nelson, and Alex Travesset. « Crystalline order on a sphere and the generalized Thomson problem. » In: *Physical Review Letters* 89.18 (2002), p. 185502.

[17] Anže Lošdorfer Božič, Antonio Šiber, and Rudolf Podgornik. « Statistical analysis of sizes and shapes of virus capsids and their resulting elastic properties. » In: *Journal of biological physics* 39.2 (2013), pp. 215–228.

[18] MW Brightman and TS Reese. « Junctions between intimately apposed cell membranes in the vertebrate brain. » In: *The Journal of cell biology* 40.3 (1969), pp. 648–677.

[19] William Fuller Brown Jr. « The effect of dislocations on magnetization near saturation. » In: *Physical Review* 60.2 (1941), p. 139.

[20] Mathias Buenemann and Peter Lenz. « Mechanical limits of viral capsids. » In: *Proceedings of the National Academy of Sciences* 104.24 (2007), pp. 9925–9930.

[21] Mathias Buenemann and Peter Lenz. « Elastic properties and mechanical stability of chiral and filled viral capsids. » In: *Physical Review E* 78.5 (2008), p. 051924.

[22] Nicholas J Butterfield. « Bangiomorpha pubescens n. gen., n. sp.: implications for the evolution of sex, multicellularity, and the Mesoproterozoic/Neoproterozoic radiation of eukaryotes. » In: *Paleobiology* 26.3 (2000), pp. 386–404.

[23] Shuiyan Cao, Eric Le Moal, Florian Bigourdan, Jean-Paul Hugonin, Jean-Jacques Greffet, Aurélien Drezet, Serge Huant, Gérald Dujardin, and Elizabeth Boer-Duchemin. « Revealing the spectral response of a plasmonic lens using low-energy electrons. » In: *Physical Review B* 96.11 (2017), p. 115419.

[24] C Carrasco, A Carreira, IAT Schaap, PA Serena, J Gomez-Herrero, MG Mateu, and PJ De Pablo. « DNA-mediated anisotropic mechanical reinforcement of a virus. » In: *Proceedings of the National Academy of Sciences* 103.37 (2006), pp. 13706–13711.

[25] Carolina Carrasco, Milagros Castellanos, Pedro J de Pablo, and Mauricio G Mateu. « Manipulation of the mechanical properties of a virus by protein engineering. » In: *Proceedings of the National Academy of Sciences* 105.11 (2008), pp. 4150–4155.

[26] Carolina Carrasco, A Luque, M Hernando-Pérez, Roberto Miranda, Jose L Carrascosa, PA Serena, M De Ridder, Arvind Raman, J Gómez-Herrero, IAT Schaap, et al. « Built-in mechanical stress in viral shells. » In: *Biophysical journal* 100.4 (2011), pp. 1100–1108.

[29] Milagros Castellanos, Rebeca Pérez, Carolina Carrasco, Mercedes Hernando-Pérez, Julio Gómez-Herrero, Pedro J de Pablo, and Mauricio G Mateu. « Mechanical elasticity as a physical signature of conformational dynamics in a virus particle. » In: *Proceedings of the National Academy of Sciences* 109.30 (2012), pp. 12028–12033.

[30] Martin Castelnovo. « Viral self-assembly pathway and mechanical stress relaxation. » In: *Physical Review E* 95.5 (2017), p. 052405.

[32] Changlun Chen, Xiangke Wang, Hui Jiang, and Wenping Hu. « Direct observation of macromolecular structures of humic acid by AFM and SEM. » In: *Colloids and Surfaces A: Physicochemical and Engineering Aspects* 302.1-3 (2007), pp. 121–125.

[33] JL Cuellar, F Meinhoevel, M Hoehne, and E Donath. « Size and mechanical stability of norovirus capsids depend on pH: a nanoindentation study. » In: *Journal of general virology* 91.10 (2010), pp. 2449–2456.

[34] Markus Deserno. « Fluid lipid membranes: From differential geometry to curvature stresses. » In: *Chemistry and physics of lipids* 185 (2015), pp. 11–45.

[35] Suraj K Dixit, Nancy L Goicochea, Marie-Christine Daniel, Ayaluru Murali, Lyudmila Bronstein, Mrinmoy De, Barry Stein, Vincent M Rotello, C Cheng Kao, and Bogdan Dragnea. « Quantum dot encapsulation in viral capsids. » In: *Nano Letters* 6.9 (2006), pp. 1993–1999.

[36] Jens Dorfmuller, Daniel Dregely, Moritz Esslinger, Worawut Khunsin, Ralf Vogelgesang, Klaus Kern, and Harald Giessen. « Near-field dynamics of optical Yagi-Uda nanoantennas. » In: *Nano letters* 11.7 (2011), pp. 2819–2824.

[38] AR Evans, MS Turner, and P Sens. « Interactions between proteins bound to biomembranes. » In: *Physical Review E* 67.4 (2003), p. 041907.

[39] Melissa M Gibbons and William S Klug. « Influence of nonuniform geometry on nanoindentation of viral capsids. » In: *Biophysical journal* 95.8 (2008), pp. 3640–3649.

[41] Gregory M Grason. « Defects in crystalline packings of twisted filament bundles. I. Continuum theory of disclinations. » In: *Physical Review E* 85.3 (2012), p. 031603.

[42] Gregory M Grason and Benny Davidovitch. « Universal collapse of stress and wrinkle-to-scar transition in spherically confined crystalline sheets. » In: *Proceedings of the National Academy of Sciences* 110.32 (2013), pp. 12893–12898.

[43] Franz X Heinz and Karin Stiasny. « The antigenic structure of Zika virus and its relation to other flaviviruses: implications for infection and immunoprophylaxis. » In: *Microbiol. Mol. Biol. Rev.* 81.1 (2017), e00055–16.

[44] Wolfgang Helfrich. « Elastic properties of lipid bilayers: theory and possible experiments. » In: *Zeitschrift für Naturforschung C* 28.11-12 (1973), pp. 693–703.

[45] Mercedes Hernando-Pérez, Elena Pascual, María Aznar, Alina Ionel, José R Castón, Antoni Luque, José L Carrascosa, David Reguera, and Pedro J de Pablo. « The interplay between mechanics and stability of viral cages. » In: *Nanoscale* 6.5 (2014), pp. 2702–2709.

[46] Stephen D. Hicks and C. L. Henley. « Irreversible growth model for virus capsid assembly. » In: *Phys. Rev. E* 74 (3 2006), p. 031912.

[47] Eric D Horowitz, K Shefaet Rahman, Brian D Bower, David J Dismuke, Michael R Falvo, Jack D Griffith, Stephen C Harvey, and Aravind Asokan. « Biophysical and ultrastructural characterization of adeno-associated virus capsid uncoating and genome release. » In: *Journal of virology* 87.6 (2013), pp. 2994–3002.

[48] Xinlei Huang, Lyudmila M Bronstein, John Retrum, Chris Dufort, Irina Tsvetkova, Stella Aniagyei, Barry Stein, Galen Stucky, Brandon McKenna, Nicholas Remmes, et al. « Self-assembled virus-like particles with magnetic cores. » In: *Nano letters* 7.8 (2007), pp. 2407–2416.

[49] Jérémy Hure, Benoît Roman, and José Bico. « Wrapping an adhesive sphere with an elastic sheet. » In: *Physical review letters* 106.17 (2011), p. 174301.

[50] Jérémy Hure, Benoît Roman, and José Bico. « Stamping and wrinkling of elastic plates. » In: *Physical review letters* 109.5 (2012), p. 054302.

[51] Borja Ibarra, Jose R Caston, Oscar Llorca, Mikel Valle, Jose M Valpuesta, and Jose L Carrascosa. « Topology of the components of the DNA packaging machinery in the phage φ29 prohead. » In: *Journal of molecular biology* 298.5 (2000), pp. 807–815.

[52] William TM Irvine, Vincenzo Vitelli, and Paul M Chaikin. « Pleats in crystals on curved surfaces. » In: *Nature* 468.7326 (2010), pp. 947–951.

[53] IL Ivanovska, PJ De Pablo, B Ibarra, G Sgalari, FC MacKintosh, JL Carrascosa, CF Schmidt, and GJL Wuite. « Bacteriophage capsids: tough nanoshells with complex elastic properties. » In: *Proceedings of the National Academy of Sciences* 101.20 (2004), pp. 7600–7605.

[54] Irena Ivanovska, Gijs Wuite, Bengt Jönsson, and Alex Evilevitch. « Internal DNA pressure modifies stability of WT phage. » In: *Proceedings of the National Academy of Sciences* 104.23 (2007), pp. 9603–9608.

[55] Jesus A Izaguirre, Daniel P Catarello, Justin M Wozniak, and Robert D Skeel. « Langevin stabilization of molecular dynamics. » In: *The Journal of chemical physics* 114.5 (2001), pp. 2090–2098.

[56] Rainer Jaenicke. « Do ultrastable proteins from hyperthermophiles have high or low conformational rigidity? » In: *Proceedings of the National Academy of Sciences* 97.7 (2000), pp. 2962–2964.

[57] Filip Jagodzinski, Jeanne Hardy, and Ileana Streinu. « Using rigidity analysis to probe mutation-induced structural changes in proteins. » In: *Journal of bioinformatics and computational biology* 10.03 (2012), p. 1242010.

[58] Stephen P Jordan and Vincent H Crespi. « Theory of carbon nanocones: Mechanical chiral inversion of a micron-scale three-dimensional object. » In: *Physical review letters* 93.25 (2004), p. 255504.

[60] William S Klug, Robijn F Bruinsma, Jean-Philippe Michel, Charles M Knobler, Irena L Ivanovska, Christoph F Schmidt, and Gijs JL Wuite. « Failure of viral shells. » In: *Physical Review Letters* 97.22 (2006), p. 228101.

[62] Artem Levandovsky and Roya Zandi. « Nonequilibirum Assembly, Retroviruses, and Conical Structures. » In: *Phys. Rev. Lett.* 102 (19 2009), p. 198102.

[63] Lin Li, Chi-Ming Chan, King Lun Yeung, Jian-Xiong Li, Kai-Mo Ng, and Yuguo Lei. « Direct observation of growth of lamellae and spherulites of a semicrystalline polymer by AFM. » In: *Macromolecules* 34.2 (2001), pp. 316–325.

[64] Siyu Li, Polly Roy, Alex Travesset, and Roya Zandi. « Why large icosahedral viruses need scaffolding proteins. » In: *Proceedings of the National Academy of Sciences* 115.43 (2018), pp. 10971–10976.

[65] Siyu Li, Roya Zandi, and Alex Travesset. « Elasticity in curved topographies: Exact theories and linear approximations. » In: *Physical Review E* 99.6 (2019). ISSN: 2470-0053.

[66] Jack Lidmar, Leonid Mirny, and David R Nelson. « Virus shapes and buckling transitions in spherical shells. » In: *Physical Review E* 68.5 (2003), p. 051910.

[67] Aida Llauró, Emilia Coppari, Francesca Imperatori, Anna R Bizzarri, José R Castón, Luca Santi, Salvatore Cannistraro, and Pedro J de Pablo. « Calcium ions modulate the mechanics of tomato bushy stunt virus. » In: *Biophysical journal* 109.2 (2015), pp. 390–397.

[68] Ranjan V Mannige and Charles L Brooks III. « Periodic table of virus capsids: implications for natural selection and design. » In: *PloS one* 5.3 (2010), e9423.

[69] Mauricio G Mateu. « Mechanical properties of viruses analyzed by atomic force microscopy: a virological perspective. » In: *Virus research* 168.1-2 (2012), pp. 1–22.

[70] JP Michel, IL Ivanovska, MM Gibbons, WS Klug, CM Knobler, GJL Wuite, and CF Schmidt. « Nanoindentation studies of full and empty viral capsids and the effects of capsid protein mutations on elasticity and strength. » In: *Proceedings of the National Academy of Sciences* 103.16 (2006), pp. 6184–6189.

[71] JH Michell. « On the direct determination of stress in an elastic solid, with application to the theory of plates. » In: *Proceedings of the London Mathematical Society* 1.1 (1899), pp. 100–124.

[72] Carlotta Negri, Alessandro L Sellerio, Stefano Zapperi, and M Carmen Miguel. « Deformation and failure of curved colloidal crystal shells. » In: *Proceedings of the National Academy of Sciences* 112.47 (2015), pp. 14545–14550.

[73] David R Nelson and BI Halperin. « Dislocation-mediated melting in two dimensions. » In: *Physical Review B* 19.5 (1979), p. 2457.

[74] T. T. Nguyen, Robijn F. Bruinsma, and William M. Gelbart. « Elasticity theory and shape transitions of viral shells. » In: *Phys. Rev. E* 72 (5 2005), p. 051923.

[75] Sanaz Panahandeh, Siyu Li, and Roya Zandi. « The equilibrium structure of self-assembled protein nano-cages. » In: *Nanoscale* 10.48 (2018), pp. 22802–22809.

[76] Richard W Pastor, Bernard R Brooks, and Attila Szabo. « An analysis of the accuracy of Langevin and molecular dynamics algorithms. » In: *Molecular Physics* 65.6 (1988), pp. 1409–1419.

[77] Antonio Pérez-Garrido, MJW Dodgson, and MA Moore. « Influence of dislocations in thomson's problem. » In: *Physical Review B* 56.7 (1997), p. 3640.

[78] Stefania Perticaroli, Jonathan D Nickels, Georg Ehlers, Hugh O'Neill, Qui Zhang, and Alexei P Sokolov. « Secondary structure and rigidity in model proteins. » In: *Soft Matter* 9.40 (2013), pp. 9548–9556.

[79] Henry C Powell, Abraham I Braude, and Peter W Lampert. « Meningoencephalitis with toroidal virus-like particles. » In: *Acta neuropathologica* 31.4 (1975), pp. 273–279.

[81] Pierre-Henri Puech, Kate Poole, Detlef Knebel, and Daniel J Muller. « A new technical approach to quantify cell–cell adhesion forces by AFM. » In: *Ultramicroscopy* 106.8-9 (2006), pp. 637–644.

[82] Eric Reissner. « Stresses and small displacements of shallow spherical shells. I. » In: *Journal of Mathematics and Physics* 25.1-4 (1946), pp. 80–85.

[83] Eric Reissner. « Stresses and small displacements of shallow spherical shells. II. » In: *Journal of Mathematics and Physics* 25.1-4 (1946), pp. 279–300.

[84] Olivier Rivoire. « Geometry and Flexibility of Optimal Catalysts in a Minimal Elastic Model. » In: *The Journal of Physical Chemistry B* 124.5 (2020), pp. 807–813.

[85] WH Roos, R Bruinsma, and GJL Wuite. « Physical virology. » In: *Nature physics* 6.10 (2010), pp. 733–743.

[86] WH Roos, MM Gibbons, A Arkhipov, C Uetrecht, NR Watts, PT Wingfield, AC Steven, AJR Heck, K Schulten, WS Klug, et al. « Squeezing protein shells: how continuum elastic models, molecular dynamics simulations, and experiments coalesce at the nanoscale. » In: *Biophysical journal* 99.4 (2010), pp. 1175–1181.

[87] Grant M Rotskoff and Phillip L Geissler. « Robust nonequilibrium pathways to microcompartment assembly. » In: *Proceedings of the National Academy of Sciences* 115.25 (2018), pp. 6341–6346.

[88] Anne-Lise Routier-Kierzkowska, Alain Weber, Petra Kochova, Dimitris Felekis, Bradley J Nelson, Cris Kuhlemeier, and Richard S Smith. « Cellular force microscopy for in vivo measurements of plant tissue mechanics. » In: *Plant physiology* 158.4 (2012), pp. 1514–1522.

[89] Subir Sachdev and David R Nelson. « Crystalline and fluid order on a random topography. » In: *Journal of Physics C: Solid State Physics* 17.30 (1984), p. 5473.

[91] DM Salunke, DL Caspar, and RL Garcea. « Polymorphism in the assembly of polyomavirus capsid protein VP1. » In: *Biophysical journal* 56.5 (1989), pp. 887–900.

[92] Roger A Sayle and E James Milner-White. « RASMOL: biomolecular graphics for all. » In: *Trends in biochemical sciences* 20.9 (1995), pp. 374–376.

[93] Shamik Sen, Shyamsundar Subramanian, and Dennis E Discher. « Indentation and adhesive probing of a cell membrane with AFM: theoretical model and experiments. » In: *Biophysical journal* 89.5 (2005), pp. 3203–3213.

[94] Hyunjune Sebastian Seung and David R Nelson. « Defects in flexible membranes with crystalline order. » In: *Physical Review A* 38.2 (1988), p. 1005.

[95] Pratik Singh, Maria J Gonzalez, and Marianne Manchester. « Viruses and their uses in nanotechnology. » In: *Drug development research* 67.1 (2006), pp. 23–41.

[97] Nicholas P Stone, Gabriel Demo, Emily Agnello, and Brian A Kelch. « Principles for enhancing virus capsid capacity and stability from a thermophilic virus capsid structure. » In: *Nature communications* 10.1 (2019), pp. 1–13.

[102] Alex Travesset. « Ground state of a large number of particles on a frozen topography. » In: *Physical Review E* 72.3 (2005), p. 036110.

[104] Dominic Vella, Amin Ajdari, Ashkan Vaziri, and Arezki Boudaoud. « Indentation of ellipsoidal and cylindrical elastic shells. » In: *Physical review letters* 109.14 (2012), p. 144302.

[105] Dominic Vella, Amin Ajdari, Ashkan Vaziri, and Arezki Boudaoud. « The indentation of pressurized elastic shells: from polymeric capsules to yeast cells. » In: *Journal of the Royal Society Interface* 9.68 (2012), pp. 448–455.

[106] Jef Wagner and Roya Zandi. « The robust assembly of small symmetric nanoshells. » In: *Biophysical journal* 109.5 (2015), pp. 956–965.

[107] SW Watson and CC Remsen. « Macromolecular subunits in the walls of marine nitrifying bacteria. » In: *Science* 163.3868 (1969), pp. 685–686.

[108] Michael Widom, Jack Lidmar, and David R Nelson. « Soft modes near the buckling transition of icosahedral shells. » In: *Physical Review E* 76.3 (2007), p. 031911.

[109] William R Wikoff and John E Johnson. « Virus assembly: Imaging a molecular machine. » In: *Current Biology* 9.8 (1999), R296–R300.

[111] Roya Zandi, Bogdan Dragnea, Alex Travesset, and Rudolf Podgornik. « On virus growth and form. » In: *Physics Reports* (2020). ISSN: 0370-1573.

[112] Roya Zandi, David Reguera, Robijn F Bruinsma, William M Gelbart, and Joseph Rudnick. « Origin of icosahedral symmetry in viruses. » In: *Proceedings of the National Academy of Sciences* 101.44 (2004), pp. 15556–15560.

[113] Cheng Zeng, Mercedes Hernando-Pérez, Bogdan Dragnea, Xiang Ma, Paul Van Der Schoot, and Roya Zandi. « Contact mechanics of a small icosahedral virus. » In: *Physical review letters* 119.3 (2017), p. 038102.

[114] Cheng Zeng, Sven Moller-Tank, Aravind Asokan, and Bogdan Dragnea. « Probing the link among genomic cargo, contact mechanics, and nanoindentation in recombinant adeno-associated virus 2. » In: *The Journal of Physical Chemistry B* 121.8 (2017), pp. 1843–1853.

[115] Yongjie Zhang and Chandrajit Bajaj. « Adaptive and quality quadrilateral/hexahedral meshing from volumetric data. » In: *Computer methods in applied mechanics and engineering* 195.9-12 (2006), pp. 942–960.

[116] Yongjie Zhang, Chandrajit Bajaj, and Bong-Soo Sohn. « 3D finite element meshing from imaging data. » In: *Computer methods in applied mechanics and engineering* 194.48-49 (2005), pp. 5083–5106.

[117] CI Zoldesi, IL Ivanovska, C Quilliet, GJL Wuite, and A Imhof. « Elastic properties of hollow colloidal particles. » In: *Physical Review E* 78.5 (2008), p. 051401.

COLLECTIONS

[27] DLD Caspar. « Assembly and stability of the tobacco mosaic virus particle. » In: *Advances in protein chemistry*. Vol. 18. Elsevier, 1964, pp. 37–121.

[59] A Klug and DLD Caspar. « The structure of small viruses. » In: *Advances in virus research*. Vol. 7. Elsevier, 1961, pp. 225–325.

TECHNICAL REPORT

[98] Rasmus Tamstorf. *Derivation of discrete bending forces and their gradients*. Tech. rep. Walt Disney Animation Studios, 2013.

ONLINE

[31] C. Cecka. *Thomson Applet*. http://thomson.phy.syr.edu/thomsonapplet.php. [Online]. 2007.

[40] D. S. Goodsell. *Artistic view of Omega Virus*. https://ccsb.scripps.edu/goodsell/. [Online].

[103] Unknown. *Explanation of the Caspar-Klug Theory*. https://viralzone.expasy.org/8577. [Online].

DECLARATION

Ce monde en lui-même n'est pas raisonnable, c'est tout ce qu'on en peut dire. Mais ce qui est absurde, c'est la confrontation de cet irrationnel et de ce désir éperdu de clarté dont l'appel résonne au plus profond de l'homme.
– *Albert Camus*

Lyon, December 18, 2020

Lucas Menou

S'il n'y a pas de solutions, il n'y a pas de problèmes.
Proverbe shadock – Jacques Rouxel

Elasticity of viral capsids and topological defects, Ph.D. thesis.
Lucas Menou
December 18, 2020